TECHNISCHE UNIVERSITÄT MÜNCHEN

Lehrstuhl für Technische Chemie II

CATALYSIS WITH IONIC LIQUID MEDIATED METAL NANOPARTICLES

Richard Knapp

Vollständiger Abdruck der von der Fakultät für Chemie der Technischen Universität München zur Erlangung des akademischen Grades eines

Doktors der Naturwissenschaften (Dr. rer. nat.)

genehmigten Dissertation.

Vorsitzender: Univ.-Prof. Dr. U. K. Heiz

Prüfer der Dissertation: 1. Univ.-Prof. Dr. J. A. Lercher

2. Univ.-Prof. Dr. K. Köhler

Die Dissertation wurde am 13.04.2010 bei der technischen Universität München eingereicht und durch die Fakultät für Chemie am 15.06.2010 angenommen.

**The more precisely you plan,
the harder destiny hits you.**

Chapter 1.

General Introduction

1.1. The water-gas shift reaction

Efficient environmental technologies such as fuel cells are in the focus of the current request for the reduction of CO_2 emission. This generates an increasing demand for CO free hydrogen, which can be directly used in proton exchange membrane or polymer electrolyte membrane (PEM) fuel cells. On an industrial scale hydrogen is currently produced on by reforming of fossil fuels, which leads in the first step to a mixture of H_2 and CO (the so called synthesis gas), followed by a the water gas shift reaction to produce CO free hydrogen (below 10 ppm CO).

A large amount of hydrogen is produced from natural gas. After cleaning and converting processes, the product mixture after the water gas shift reaction usually contains 80 % H_2, 20 % CO_2, 0.1 % CO, residual methane and water. Since the presence of more than 10 ppm CO in the hydrogen leads to catalyst poisoning when used in PEM fuel cells, further cleaning steps or more efficient processes are required to minimize the amount of CO.[1]

Different processes are used to generate synthesis-gas. The endothermic reforming reactions (equation (1) and (2)) are reversible and therefore, have to be carried out at high temperatures and low pressures.[2]

$$CH_4 \quad + \quad H_2O \quad \rightleftharpoons \quad CO \quad + \quad 3\ H_2 \quad \Delta H^o = 206\ kJ/mol \quad \textbf{(1)}$$

$$CH_4 \quad + \quad CO_2 \quad \rightleftharpoons \quad 2\ CO \quad + \quad 2\ H_2 \quad \Delta H^o = 247\ kJ/mol \quad \textbf{(2)}$$
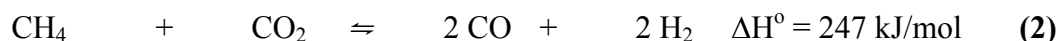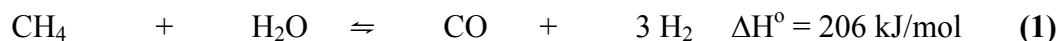
Furthermore hydrogen can be formed by partial oxidation of methane (equation (3)), which together with the total oxidation (equation (4)) as a side reaction are exothermic and lead to an increase of the system temperature.[2]

$$CH_4 \quad + \quad 0.5\ O_2 \quad \rightleftharpoons \quad CO \quad + \quad 2\ H_2 \quad \Delta H^o = -36\ kJ/mol \quad \textbf{(3)}$$

$$CH_4 \quad + \quad 2\ O_2 \quad \rightleftharpoons \quad CO_2 \quad + \quad 2\ H_2O \quad \Delta H^o = -80\ kJ/mol \quad \textbf{(4)}$$
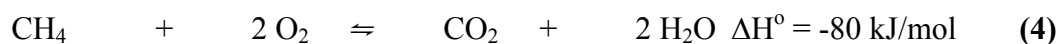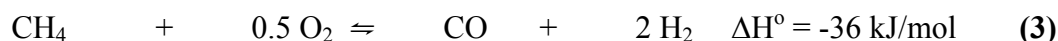
As mentioned above, the water-gas shift reaction (scheme (5)) is one possibility to remove CO from synthesis-gas and to adjust the CO to H_2 ratio.

$$CO + \quad H_2O \quad \rightleftharpoons \quad CO_2 \quad + \quad H_2 \qquad \Delta H^o = \text{-41 kJ/mol} \qquad \textbf{(5)}$$
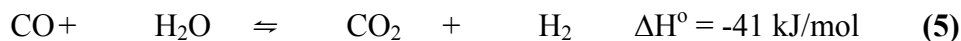
Since the reaction is exothermic, the equilibrium constant of the reaction increases with decreasing temperatures (the CO concentration decreases with temperature). The equilibrium gas mixture calculated for a gas composition close to industrial conditions is shown in Figure 1-1. The exit stream after the water-gas shift step at 200 °C contains less than 0.5 % CO. For further purification (CO concentrations below 50 ppm) selective oxidation is applied.[3]
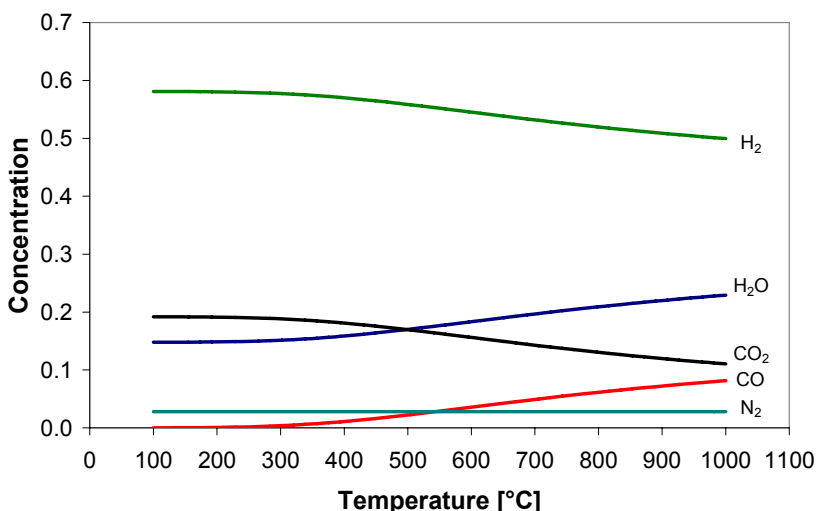
Figure 1-1: Calculated equilibrium concentrations of H_2, H_2O, CO_2, CO and N_2 at different temperatures (feed gas: 75 % hydrogen, 8 % carbon monoxide, 13 % carbon dioxide and 4 % nitrogen, steam to gas ratio of 3 to 10).

The first time the water-gas shift reaction was used on an industrial scale was the Haber-Bosch-ammonia-synthesis in the beginning of the 20th century. The water-gas shift reaction was used to increase the H_2 yield and to minimize the CO concentration, thus avoiding catalyst poisoning.[4] Table 1-1 lists different low-temperature shift catalysts developed in the last years. Mainly Cu, Au and Pt catalysts were used on different

supports like CeO_2 and Al_2O_3. A detailed description of the reaction mechanism of the water-gas shift reaction over copper catalysts is given in the next section and in chapter 5 of this thesis.

Table 1-1: Shift catalysts developed in the last few years[5-12]

Catalyst	Activation	CO conversion at 200 °C [%]	Reaction conditions
2 wt.% Pt/0.5 wt.% Na/CeO$_2$[5] 2 wt.% Pt/0.9 wt.% K/CeO$_2$[5] 2 wt.% Pt/CeO$_2$[5]	H$_2$/300 °C	24 27 15	3 % CO, 47 % H$_2$O$_{(g)}$, 50 % H$_2$, atmospheric pressure
8 wt.% Au/TiO$_2$[6] 8 wt.% Au/CeO$_2$[6]	air/300 °C	75 55	5 % CO in He saturated with 10 % H$_2$O$_{(g)}$, atmospheric pressure
5.3 wt.% Pt/CeO$_x$[7] 1.2 wt.% Pt/CeO$_x$[7] 0.7 wt.% Pt/CeLa(10 wt.%)O$_x$[7]	no activation	40 20 10	2 % CO, 10.7 % H$_2$O in He, atmspheric pressure
4.73 wt.% Au/MTiO$_2$[a] [8] 3.15 wt.% Au/CeMTiO$_2$[a] [8] 1.36 wt.% Au/CeMTiO$_2$[a] [8]	no activation	70 55 80	4.5 % CO in Ar, H$_2$O$_{(g)}$ with partial pressure 31.1 kPa, atmospheric pressure
30 wt.% CuO/1 wt.% Al$_2$O$_3$/CeO$_2$[9] 30 wt.% CuO/5 wt.% Al$_2$O$_3$/CeO$_2$[9] 30 wt.% CuO/CeO$_2$[9]	no activation	84 64 75	25 % CO, 50 % H$_2$, 8 % CO$_2$, balance N$_2$, vapor to feed = 1:1, atmospheric pressure
0.5 wt.% Pt/CeO$_2$[10] 0.5 wt.% Pt/TiO$_2$[10] 0.5 wt.% Pt/ZrO$_2$[10] 0.5 wt.% Pt/Ti$_{0.5}$Ce$_{0.5}$O$_2$[10]	H$_2$/300 °C	60[b] 55[b] 95[b] 60[b]	3 % CO, 7.5 % H$_2$O$_{(g)}$, balance N$_2$, atomspheric pressure
4 wt.% Cu/5 wt.% ZnO/Al$_2$O$_3$[11] (surface area 100 m^2·g^{-1}) 4 wt.% Cu/5 wt.% ZnO/Al$_2$O$_3$[11] (surface area 125 m^2·g^{-1}) 4 wt.% Cu/5 wt.% ZnO/MgO[11] 4 wt.% Cu/5 wt.% ZnO/ SiO$_2$-MgO[11] 4 wt.% Cu/5 wt.% ZnO/CeO$_2$[11]	H$_2$/250 °C	67 92 20 5 55	2.5 % CO, 50 % H$_2$O$_{(g)}$, 47.5 % N$_2$, atmospheric pressure
38 wt.% Cu/6 wt.% Mn/Al$_2$O$_3$[12] 36 wt.% Cu/9 wt.% Mn/Al$_2$O$_3$[12] 36 wt.% Cu/11 wt.% Mn/Al$_2$O$_3$[12]	H$_2$/300 °C	60 70 65	2 % CO, 15 % CO$_2$, 45 % H$_2$, 38 % N$_2$, H$_2$O$_{(g)}$, atmospheric pressure

[a] MTiO$_2$ = mesoporous titania, [b] CO conversion at 300°C.

In industrial plants the water-gas shift reaction is performed in two processes, the high-temperature and the low-temperature water-gas shift reaction. The high-temperature water-gas shift reaction (HTWGS), which reduces the CO concentration to 3-4 %, is operated at temperatures between 350-450 °C using iron-chromium oxide catalysts. At these temperatures the concentration of hydrogen is limited by the equilibrium between $CO + H_2O$ and $CO_2 + H_2$.[3] The low-temperature water-gas shift reaction (LTWGS) is

performed at temperatures between 210-250 °C over copper zinc based catalysts. These catalysts are pyrophoric if exposed to air and deactivate in the presence of liquid water. Furthermore a clean feedstock is needed in order to avoid thermal sintering of the metal particles and deactivation by sulphur and halides. Since the reaction is reversible the rate of the CO conversion is reduced by the presence of the products CO_2 and H_2 [13].

1.2. Ionic liquids

Ionic liquids are a highly solvating, non-coordinating media, in which many organic and inorganic compounds can be dissolved. Their lack of a measurable vapor pressure makes them attractive substitutes for volatile organic solvents. Furthermore ionic liquids are usually non-flammable, have a high thermal stability and are relatively inexpensive to produce. Typically they are in the liquid state between temperatures well below room temperature.[14] Moreover, ionic liquids are molten salts and not salts dissolved in a liquid. Usually one or both of the ions are particularly large and the cation has a low degree of symmetry. These factors lower the lattice energy and hence the melting points.[14]

The first substance acting as an ionic liquid at room temperature $[EtNH_3]^+[NO_3]^-$, was discovered in 1914[15]. However, only the development of binary ionic liquids from mixtures of aluminium (III) chloride and N-alkylpyridinium or 1,3-dialkylimidazolium chloride in 1948 triggered the scientific interest in this class of substances. Ionic liquids have been used as non-aqueous polar solvents for transition metal complexes since the 1990′s. Nowadays new ionic liquids applied as solvents and catalysts are developed, with 10^{18} different cation-anion combinations being possible.[14]

1.2.1. Synthesis of ionic liquids

In the synthesis of ionic liquids amins or phosphates are converted into cations by quaternization (see Step 1 in Figure 1-3).[14] The most important cations are shown in Figure 1-2.
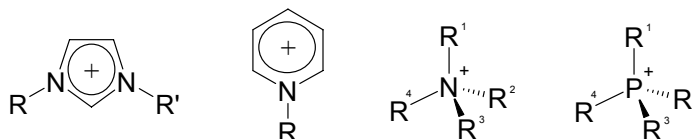
Figure 1-2: Important cations for ionic liquids from left to right: imidazolium-, pyridinium-, ammonium- and phosphonium-ion.

The anions (that can be formed by the quaternization reaction in the most simple case) can have simple structures like halides (Cl⁻, Br⁻, I⁻) or complex structures like the anorganic ions tetraflouroborate (BF_4^-), hexaflourophosphate (PF_6^-), tetrachloroaluminate ($AlCl_4^-$) and large organic ions triflouromethansulfonate (OTf⁻) or bis(triflouromethylsulfonyl)imide (NTf_2^-). If the desired anion can not be directly supplied by the quaternization reaction further synthesis steps have to be applied (see Step 2a and 2b in Figure 1-3). One possibility is (synthesis route 2a) to react the ammonium halide with a Lewis-acid. The other possibility (synthesis route 2b) is to exchange the halide with a favoured anion. The exchange can be realized by addition of a metal salt (leads to precipitation of the undesired anion or a strong Brønsted-acid or by ion exchange.[14]
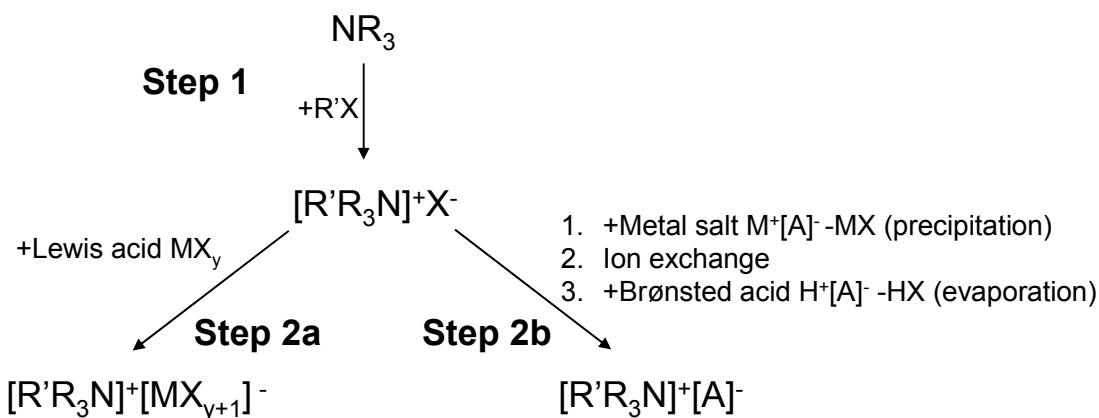
Figure 1-3: Routes for ionic liquid synthesis, e.g. for an ammonium salt.[14]

The synthesis of highly pure ionic liquids, which is essential for applications as solvents or for determination of physical and chemical properties, requires special attention. Residues of halides and of the acid used can lead to undesirable reactivity. Usually the highest purity can be achieved by an ion exchange over an ion exchanger.[14]

Throughout this work 1-Butyl-2,3-dimethyl-imidazolium trifluoromethane sulphonate denoted as BDiMIm was used as ionic liquid (see Figure 1-4), because of the high thermal stability of this imidazolium salt. Furthermore the C-2 position (denoted as 1 in Figure 1-4) was blocked by a methyl group to avoid reactivity of the ionic liquid at this position due to deprotonization.
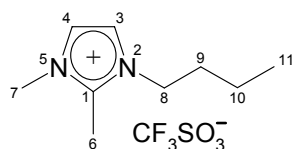
Figure 1-4: 1-Butyl-2,3-dimethyl-imidazolium trifluoromethane sulphonate (BDiMIm)

1.2.2.   General physical properties of ionic liquids

Ionic liquids consist only of ions and are low-melting and low-viscous salts at low temperatures (< 100 °C). The structure and chemical composition influence the melting point of ionic liquids. The cations and anions play an essential role in the melting point of the ionic liquid. To synthesise materials with a low melting point, the cation used should have a low symmetry, a high charge distribution and low intermolecular interactions avoiding hydrogen bonds. Increasing the size of the anion but keeping the charge constant leads to a further lowering of the melting point. A high amount of anion species in the ionic liquids also lead to a low melting point.[14, 16]

Ionic liquids have no measurable vapour pressure, which facilitates the separation by distillation and avoids problems with azeotrope formation between solvent and reaction products. However, the thermal stability is limited by the reactivity of the heteroatom-carbon and the heteroatom-hydrogen bonding. Ionic liquids formed by the direct protonation of amines or phosphanes have in general low thermal stability (decomposition at temperatures below 80 °C in high vacuum). The thermal stability of ionic liquids prepared by alkylation of amines or phosphanes mainly depends on the nature of the anion. Ionic liquids with chloride as anion are decomposed at 150 °C

whereas ionic liquids with bis(trifluoromethylsulfonyl)imide as anion are stable up to 400 °C. This is an example for ionic liquids with a liquid range of 400 °C.[14, 16, 17]

The density of ionic liquids is generally low for bulky cations, but mainly the choice of the anion ultimately defines the density. By proper choice of the cation the density can be fine tuned.[14]

The viscosity of ionic liquids is determined mostly by the concentration of hydrogen bonds and to a minor part by the strength of van der Waals interactions between the anion and the cation. Ionic liquids with high viscosity can be synthesized by using e.g. small basic anions (e.g. chloride), whereas the use of large anions usually leads to low viscosities.[14, 17]

The properties of ionic liquids as solvents can be tuned by varying the alkyl side chain length of an unpolar cation. Many ionic liquids are totally mixable with organic solvents by increase of the dielectric constant to a characteristic limit that is specific for each cation-anion combination.[17]

1.3. Supported ionic liquid catalysts

1.3.1. Overview of different supported ionic liquid catalysts

In order to design a new catalyst generation with high activity, selectivity, stability and efficiency supported ionic liquid phase (SILP)-catalysts were developed. These catalysts combine the advantages of homogeneous and heterogeneous catalysis, therefore expensive separation processes are not necessary, decreasing the costs of production.[18]

Supported ionic liquid catalysts are prepared by impregnation of a porous material with high specific surface area with an ionic liquid. Catalytic active components like metal nanoparticles or metal organic complexes are immobilized in the ionic liquid phase.[19] Due to the formation of an ionic liquid film on the surface undesirable side reactions can be inhibited, lowering the amounts of by-products and thus increasing the efficiency of the catalysis.

Supported ionic liquid catalysts can be used in fixed-bed reactors without the need for organic solvents. Due to the non-volatile ionic liquid film the catalysts can be applied in

gas phase reactions.[18] They were successfully used in test reactions like hydroformylation of olefines[19], achiral hydrogenation[20], Heck-reaction[21] and hydroamination[22, 23]. These applications can usually not be realized with supported organic phase[24] and aqueous phase[25, 26] catalysts that were developed since 1990. The liquid film of these catalysts is volatile, so that high temperatures can not be applied and also the stability of the catalytic active component the organic or aqueous phase is sometimes problematic.[14] The schematic drawing of a supported ionic liquid catalyst with metal nanoparticles as the active component immobilized on an alumina support on is depicted in Figure 1-5.
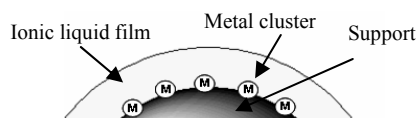
Figure 1-5: Catalyst concept with metal clusters immobilized in thin films of ionic liquid

1.3.2. *Preparation methods of catalysts with ionic liquid mediated nanoparticles*

Supported ionic liquid catalysts, with metal nanoparticles as active component, can be prepared by different methods. In all cases the ionic liquid phase acts as surface agent and reaction medium.

Incipient wetness method. First the support is dried to remove water from the surface and the pores. A metal precursor dissolved in water is impregnated on the dried support by incipient wetness. After calcination metal oxides are formed and then reduced under hydrogen forming the metal nanoparticles. Afterwards the catalysts are coated with ionic liquid. The scheme for this preparation method is shown in Figure 1-6.
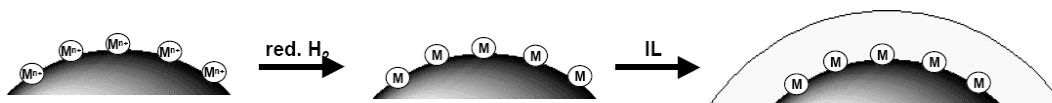
Figure 1-6: Scheme of preparation method A. Impregnation, reduction and coating.

The thickness of the ionic liquid film can vary from 3-5 nm. With this method metal nanoparticles with a particle size of 1 to 2 nm are synthesized. This preparation method was used for the synthesis of the Pt catalysts in chapter 2 of this thesis as well as for the synthesis of the Cu catalysts used in chapter 5. Also different publications dealt with catalysts prepared according to this preparation method.[27, 28]

Reduction of the metal precursors via alcohol. The metal precursor is dissolved in a solution containing an alcohol and a polymer, e.g. polyvinyl-2-pyrrolidon (PVP). The alcohol is used to reduce the metal precursors. The polymer stabilizes the metal nanoparticles, leading to high dispersion avoiding agglomeration. After removal of the solvent the residue is dissolved in an ionic liquid solution that is afterwards impregnated on the dried support. The polymer stabilized metal particles are distributed in the ionic liquid phase. The scheme of this preparation method is shown in Figure 1-7.
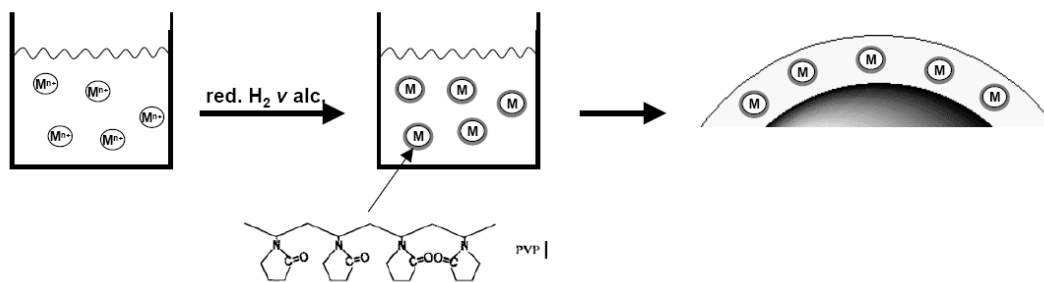
Figure 1-7: Scheme of preparation method B. Reduction, stabilization, coating and impregnation.

The thickness of the ionic liquid film can also vary from 3-5 nm and the particle size can reach 1-5 nm. This method was used for the preparation of the Pt catalysts described in chapter 3 of this thesis. It should be noted that there are various preparation methods for the synthesis of the polymer protected nanoparticles. In this work the Pt particles were synthesize according to Busser *et. al*[29] and to Teranishi *et. al*[30]. The advantage of the Busser method is that no atomically dispersed Pt is found within the protecting polymer layer (for further details see chapter 3).

In-situ reduction in the ionic liquid. The metal precursor is dissolved in a solution containing a solvent and the ionic liquid. This solution is impregnated on the dried support. The metal ions are reduced in the ionic liquid phase with hydrogen under mild conditions (see Figure 1-8).
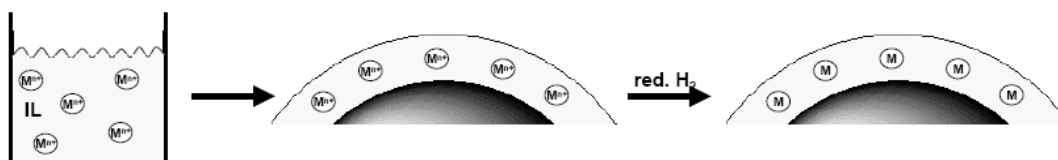
Figure 1-8: Scheme of preparation method C. Coating, impregnation and reduction.

The drawback of this synthesis method is that the metal nanoparticles can agglomerate if no stabilizing agent or a strongly coordinating ionic liquid is added.

1.4. Scope of the thesis

This work is focused on understanding the interactions of immobilized ionic liquids with active components (e.g. metal nanoparticles) as well as with the support. The knowledge of nature of these interactions is of essential value when using these materials as catalysts, since the properties of the ionic liquid are dramatically influenced by the support and the active components.

On the one hand physicochemical methods are utilized to study the surface chemistry and the behavior of the highly polar ionic liquid in the presence of nanoparticles. On the other hand the detailed analysis of reactions where materials with supported ionic liquids are used as catalysts (e.g. ethylene hydrogenation and low temperature water-gas shift) gives further insight to the interactions between the ionic liquid and the support as well as the active component and the reactants.

The impact of supported ionic liquids on supported Pt catalysts is studied in chapter 2. Silica supported platinum catalysts coated with a thin film of 1-butyl-2,3-dimethyl-imidazolium trifluoromethane sulphonate (BDiMIm) were investigated with respect to the interactions of the ionic liquid with the oxide support and the metal clusters. IR,

inelastic neutron scattering and NMR spectroscopy indicate that the vibrations of the imidazolium ring of ionic liquid are less restricted when supported on SiO_2, while the viscosity of the supported ionic liquid increased. The presence of Pt particles enhances the electron density of the ionic liquid at the nitrogen atom inducing higher basicity. The coverage of the catalyst surface and the metal particles by the ionic liquid protects the metal against oxidation. The catalysts are active and stable for hydrogenation of ethene.

Chapter 3 deals with the corrugated structure of ionic liquid surfaces with polymer stabilized platinum nanoparticles. Ionic liquids such as 1-butyl-2,3-dimethyl-imidazolium trifluoromethane sulphonate stabilize complex structures of polyvinylpyrrolidone protected nanoparticles on their surface. The polyvinylpyrrolidone shell around the Pt nanoparticles remains intact, but the ionic liquid partly penetrates the protective layer and interacts with the metal. This leads to a pronounced increase of the viscosity of the ionic liquid, as observed also with metal complexes. The protected particles form small islands of aggregated moieties that are connected by interacting polymer strands, a process enhanced by diluting the sample in methanol during preparation. These ensembles segregate at the surface protruding significantly out from the bulk ionic liquid. The outermost layer of the surface, however, consists of the ionic liquid with the cation being on top and the SO_3-group of the anion underneath being oriented towards the bulk.

An inelastic neutron scattering (INS) and MAS NMR analysis of ionic liquid coated catalysts is presented in chapter 4. In this chapter supported ionic liquids were used to investigate on the influences of different support materials on ionic liquids. Also the immobilization of metal nanoparticles, in thin films of supported ionic liquid, was studied as a novel concept to combine the high selectivity of homogeneous catalysts with the easy separation of a heterogeneous system. Focus was put on the interaction of the highly polar ionic liquid with the metal particles in order to understand the activity and selectivity of these catalysts.

The work presented in chapter 5 is focused on the synthesis and characterization of catalysts based on ionic liquid mediated metal nanoparticles, which can be used for the low temperature water-gas shift reaction. The reactivity of alumina supported copper catalysts coated with a thin film of 1-butyl-2,3-dimethyl-imidazolium trifluoromethane sulphonate was compared to uncoated and commercial catalysts. XAFS experiments

showed that a balanced concentration of oxygen neighboring atoms is necessary to achieve high conversions of CO. These oxygen atoms are removed during the reaction leading to differently structured copper nanoparticles. The reduction degree increased with the loading of the ionic liquid, because the water formed during reduction was dissolved in the ionic liquid. CO is adsorbed weaker on coated catalysts, while the concentration of CO_2 and H_2O was higher in the presence of the ionic liquid. The higher concentration of water in the proximity of the active sites and the interaction of the ionic liquid with the intermediate carboxyl species led to higher activities at low temperatures of catalysts coated with ionic liquid compared to uncoated and commercial systems.

Finally chapter 6 summarizes the most important results and conclusions of the presented thesis.

1.5. References

[1]   S. Giddey, F. T. Ciacchi, S. P. S. Badwal, *J. Power Sources* **2004**, *125*, 155.

[2]   A. S. Bodke, S. S. Bharadwaj, L. D. Schmidt, *J. Catal.* **1998**, *179*, 138.

[3]   D. L. Trimm, *Appl. Catal., A* **2005**, *296*, 1.

[4]   K. Holdermann, *Carl Bosch. Im Banne der Chemie*, 1 ed., Econ-Verlag, Düsseldorf, **1953**.

[5]   H. N. Evin, G. Jacobs, J. Ruiz-Martinez, G. A. Thomas, B. H. Davis, *Catal. Lett.* **2008**, *120*, 166.

[6]   A. Sandoval, A. Gomez-Cortes, R. Zanella, G. Diaz, J. M. Saniger, *J. Mol. Catal. A: Chem.* **2007**, *278*, 200.

[7]   D. Pierre, W. L. Deng, M. Flytzani-Stephanopoulos, *Top. Catal.* **2007**, *46*, 363.

[8]   V. Idakiev, T. Tabakova, K. Tenchev, Z. Y. Yuan, T. Z. Ren, B. L. Su, *Catal. Today* **2007**, *128*, 223.

[9]   L. Li, Y. Y. Zhan, Q. Zheng, Y. H. Zheng, X. Y. Lin, D. L. Li, J. J. Zhu, *Catal. Lett.* **2007**, *118*, 91.

[10]   K. G. Azzam, I. V. Babich, K. Seshan, L. Lefferts, *J. Catal.* **2007**, *251*, 163.

[11]   H. Yahiro, K. Murawaki, K. Saiki, T. Yamamoto, H. Yamaura, *Catal. Today* **2007**, *126*, 436.

[12]   D. C. Yeragi, N. C. Pradhan, A. K. Dalai, *Catal. Lett.* **2006**, *112*, 139.

[13]   Y. Amenomiya, G. Pleizier, *J. Catal.* **1982**, *76*, 345.

[14]   P. Wasserscheid, W. Keim, *Angew. Chem., Int. Ed.* **2000**, *39*, 3773.

[15]   P. Walden, *Bull. Acad. Sci. St. Petersburg* **1914**, 405.

[16]   J. S. Wilkes, J. A. Levisky, R. A. Wilson, C. L. Hussey, *Inorg. Chem.* **1982**, *21*, 1263.

[17]   P. Bonhote, A. P. Dias, N. Papageorgiou, K. Kalyanasundaram, M. Gratzel, *Inorg. Chem.* **1996**, *35*, 1168.

[18]   T. Welton, *Coord. Chem. Rev.* **2004**, *248*, 2459.

[19]   A. Riisager, R. Fehrmann, S. Flicker, R. van Hal, M. Haumann, P. Wasserscheid, *Angew. Chem., Int. Ed.* **2005**, *44*, 815.

[20]   A. Wolfson, I. F. J. Vankelecom, P. A. Jacobs, *Tetrahedron Lett.* **2003**, *44*, 1195.

[21]   H. Hagiwara, Y. Sugawara, K. Isobe, T. Hoshi, T. Suzuki, *Org. Lett.* **2004**, *6*, 2325.

[22]   C. Sievers, O. Jimenez, R. Knapp, X. Lin, T. E. Muller, A. Turler, B. Wierczinski, J. A. Lercher, *J. Mol. Catal. A: Chem.* **2008**, *279*, 187.

[23]   S. Breitenlechner, M. Fleck, T. E. Muller, A. Suppan, *J. Mol. Catal. A: Chem.* **2004**, *214*, 175.

[24]   H. L. Pelt, J. J. J. J. Brockhus, R. P. J. Verburg, J. J. F. Scholten, *Journal of Molecular Catalysis* **1985**, *31*, 107.

[25]   J. P. Arhancet, M. E. Davis, J. S. Merola, B. E. Hanson, *Nature* **1989**, *339*, 454.

[26]   J. P. Arhancet, M. E. Davis, J. S. Merola, B. E. Hanson, *Journal of Catalysis* **1990**, *121*, 327.

[27]   J. P. Mikkola, P. Virtanen, H. Karhu, T. Salmi, D. Y. Murzin, *Green Chemistry* **2006**, *8*, 197.

[28]   R. Knapp, A. Jentys, J. A. Lercher, *Green Chemistry* **2009**, *11*, 656.

[29]   G. W. Busser, J. G. van Ommen, J. A. Lercher, *J. Phys. Chem. B* **1999**, *103*, 1651.

[30]   T. Teranishi, M. Hosoe, M. Miyake, *Advanced Materials* **1997**, *9*, 65.

Chapter 2.

Impact of supported ionic liquids on supported Pt catalysts

Abstract

Silica supported platinum catalysts coated with a thin film of 1-butyl-2,3-dimethyl-imidazolium trifluoromethane sulphonate (BDiMIm) were investigated with respect to the interactions of the ionic liquid with the oxide support and the metal clusters. IR, inelastic neutron scattering and NMR spectroscopy indicate that the vibrations of the imidazolium ring of ionic liquid are less restricted when supported on SiO_2, while the viscosity of the supported ionic liquid increased. The presence of Pt particles enhances the electron density of the ionic liquid at the nitrogen atom inducing higher basicity. The coverage of the catalyst surface and the metal particles by the ionic liquid protects the metal against oxidation. The catalysts are active and stable for hydrogenation of ethene.

2.1. Introduction

To combine the high diversity and homogeneity of molecular catalysts with the facile separation of solid catalysts the immobilization of organometallic complexes in thin films of supported ionic liquid has been proposed as new concept.[1-3] As such, immobilizing an organic[4] or aqueous phase[5] on a support surface has already been described in 1990. The major drawback of these catalysts, however, has been that the liquid film is volatile, which limits the application at high temperatures. In addition, the stability of the catalytically active component in the aqueous phase is often insufficient.

An alternative are the recently introduced supported ionic liquid catalysts, prepared by impregnation of a porous material with an ionic liquid.[6] The catalytically active components are immobilized in the ionic liquid and due to the low vapor pressure these catalysts can be applied in gas phase reactions.[7] The properties of the supported catalysts can be fine-tuned by optimizing the type of ionic liquid and of the metal component. In particular, the solubility and, thus, the selectivity for different reactants can be improved by selecting the polarity of the ionic liquid. The interaction between the ionic liquid and the active component is complex showing ordering phenomena and domain formation of the ionic liquid.[8, 9] Catalysts with immobilized ionic liquids were successfully used in reactions like hydroformylation of olefins[1], achiral hydrogenation[10], Heck-reaction[11] and hydroamination.[2, 3]

This chapter is focused on the synthesis and characterization of catalysts based on ionic liquid mediated metal nanoparticles, which allows combining different functionalities in a single material as co-catalysts and/or stabilizing agents can be easily added into the ionic liquid phase. As active component Pt metal clusters were immobilized in supported thin films of 1-butyl-2,3-dimethyl-imidazolium trifluoromethane sulphonate. Key properties for the application as catalysts such as accessibility, mobility and local environment of the metal clusters were studied with a particular focus on the interaction between metal clusters and ionic liquids.

2.2. Experimental

2.2.1.   Materials

The ionic liquid 1-butyl-2,3-dimethyl-imidazolium trifluoromethane sulphonate (BDiMIm) (99 %) with a maximum water and halide content of 47.8 and 103.1 ppm, respectively, was kindly provided by Solvent Innovation GmbH. Chloroplatinic acid hexahydrate (Pt content $\geq$ 37.5 %) and methanol (99.8 %) were obtained from Aldrich. Octane (>99 %) was purchased from Fluka. All chemicals were used as received. The silica support Aerosil 355 was provided by Degussa AG. For INS measurements SiO_2-60 from Chemie AG was used.

2.2.2.   Preparation of the supported catalysts

The silica support was ground, sieved to 100 μm particle size and dried at 200 °C. Catalysts with immobilized metal clusters (1 wt% metal) were prepared by incipient wetness impregnation. Chloroplatinic acid hexahydrate was dissolved in the appropriate amount of bi-distilled water; the solution was trickled onto the support and stirred until the water was completely absorbed. The water was removed by freeze drying. The precursors were calcined at 400 °C for three hours in synthetic air and subsequently reduced at 250 °C for three hours in a flow of hydrogen.

For preparing the supported ionic liquid catalysts Pt/SiO_2 was added to a solution of BDiMIm dissolved in methanol. The suspension was stirred at room temperature for 10 min and the volatile components were slowly removed by freeze drying to give a free flowing grey powder ($Pt/BDiMIm/SiO_2$).

A silica supported ionic liquid was prepared by adding SiO_2 into a solution of BDiMIm dissolved in methanol. After stirring for 10 min, the suspension was freeze dried to give a free flowing white powder ($BDiMIm/SiO_2$).

2.2.3.   Characterization

The platinum content of the supported catalysts was determined by AAS using a UNICAM 939 spectrometer. The amount of ionic liquid adsorbed on the surface was determined by elemental analysis.

The IR spectra were measured on a Bruker IFS 88 spectrometer in transmission mode. The samples were pressed into self-supporting wafers and activated in vacuum for 1 h at 150 °C. Pt containing samples were reduced *in-situ* at 250 °C and 0.8 bar hydrogen for 30 minutes. The spectra were recorded at a resolution of 4 cm^{-1} in the region from 4000 to 400 cm^{-1}. To compare the different samples, the spectra of the activated samples were normalized using the overtone and combination vibrations of silica between 2105 and 1740 cm^{-1}. For IR measurements of the pure ionic liquid, a KBr wafer was pressed and analyzed using a Jasco FT/IR-460 Plus spectrometer.

INS-Experiments were carried out at 15 K at the Be-filter detector spectrometer IN1BeF at ILL in Grenoble using a Cu (220) monochromator. The instrument resolution was between 4 cm^{-1}, at low energy transfers and 25 cm^{-1} at high energy transfers. The vibrational modes of the ionic liquid were calculated with *GAUSSIAN03*[12] and the INS spectra were calculated using *a-CLIMAX*.[13]

For solid state NMR, the samples were packed in 4 mm ZrO_2 rotors. ^{1}H MAS NMR measurements were performed on a Bruker AV500 spectrometer (B_0 = 14.1 T) with a spinning rate of 15 kHz. For temperature adjustment the bearing and drive gas stream were passed through a heat exchanger. The spectra were recorded as the sum of 100 scans using single pulse excitation with a pulse length of 2.6 μs and recycle time of 3 s.

For transmission electron microscope images, the samples were grinded, suspended in octane and ultrasonically dispersed. Drops of the dispersions were applied on a copper-grid supported carbon film. Micrographs were recorded on a JEM-2010 Jeol transmission electron microscope operating at 120 kV.

The EXAFS spectra were collected at the beamline X1 at HASYLAB, DESY, Hamburg, Germany. The storage ring was operated at 4.5 GeV with an average current of 100 mA. The Si (311) double-crystal monochromator was detuned to 60% of the maximum intensity to minimize the intensity of higher harmonics in the X-ray beam. The catalysts were pressed into self supporting wafers (ca. 150 mg) and the X-ray absorption

spectra were collected at the Pt L_{III} edge (11.564 eV) in a helium flow at liquid N_2 temperature. The EXAFS data was analysed using the *Viper* software.[14] For EXAFS analysis, the scattering contributions of the background were removed from the X-ray absorption by a third-order polynomial function. The oscillations were weighted with k^2 and Fourier-transformed within the limit k = 3.5–16 Å^{-1}. The local environment of the Pt atoms was determined from the EXAFS using the phase-shift and amplitude function for Pt–Pt and Pt–O calculated assuming multiple scattering processes (FEFF version 8.40).[15, 16]

The XANES data were collected in a helium flow at room temperature and analysed using the *XANES dactyloscope* software.[17] All recorded XANES spectra were normalized to unity. The position of the edge was calibrated using the spectra of a Pt reference-foil measured simultaneously.

2.2.4. Catalytic activity

The hydrogenation of ethylene was studied at temperatures between 30 and 50 °C with a hydrogen to ethylene ratio of 2.5 : 1 in a fixed bed reactor filled with 0.1 mg catalyst (diluted with SiO_2 and SiC). The products were analyzed using a Shimadzu GC-2014 gas chromatograph.

2.3. Results

2.3.1. Infrared spectroscopy

The IR spectra of the catalysts and of the pure ionic liquid (prepared in KBr) are shown in Figure 2-1. With pure SiO_2 support a sharp band at 3745 cm^{-1} and a broad band at 3600 cm^{-1} were observed, which are assigned to free and hydrogen bonded silanol groups. After depositing Pt on this silica support (Pt/SiO_2) the intensity of the band for silanol groups decreased by 20 %. Upon adsorption of BDiMIm on SiO_2 (BDiMIm/SiO_2) and on Pt/SiO_2 (Pt/BDiMIm/SiO_2) the band corresponding to terminal SiOH groups disappeared and new bands at 3390 cm^{-1} (BDiMIm/SiO_2) and 3372 cm^{-1}

(Pt/BDiMIm/SiO$_2$) were observed. All other bands observed in these spectra are attributed to the ionic liquid.

Symmetric and asymmetric stretching vibrations of =CH groups appear at 3184 and 3142 cm^{-1}, C-H stretching vibrations of methylen and methyl groups give absorption bands at 2967 and 2941 cm^{-1} and the methyl amino group was observed at 2878 cm^{-1}. At 1589 and 1538 cm^{-1} C=C stretching vibrations and at 1434, 1423 and 1388 cm^{-1} C-H bending vibrations were observed. For the ionic liquid prepared in KBr bands at 2000, 1890 and 1645 cm^{-1} were observed assigned to ring deformation vibrations and stretching vibrations of C=N.

After immobilization of the ionic liquid on SiO$_2$ or Pt/SiO$_2$ the bands at 2975 cm^{-1} (C-H stretching) and 1473 cm^{-1} (C-H bending) were shifted to lower wavenumbers (2968 and 1466 cm^{-1}) compared with the ionic liquid prepared in KBr.
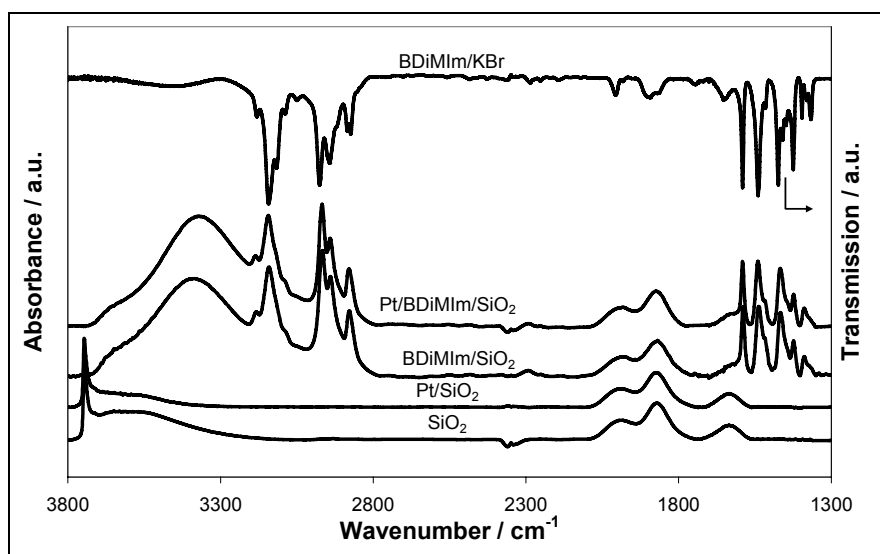
Figure 2-1   IR absorption spectra of the silica support, platinum supported on silica, ionic liquid supported on silica and ionic liquid supported on Pt/SiO$_2$ and IR transmission spectrum of the ionic liquid in KBr

2.3.2.   Inelastic neutron scattering

The INS spectra of pure BDiMIm, BDiMIm supported on SiO$_2$ and BDiMIm supported on Pt/SiO$_2$ are shown in Figure 2-2. The bands at 580 cm^{-1}, 725 cm^{-1} and 1050 cm^{-1} increased when BDiMIm is supported on SiO$_2$ or on Pt/SiO$_2$. The bands at

580 cm^{-1} and 1050 cm^{-1} were assigned to ring deformation vibrations of the imidazolium ring, the band at 725 cm^{-1} to out of plane vibrations -CH groups of the C$_5$-ring. For the supported ionic liquids the band at 580 cm^{-1} was shifted to 610 cm^{-1}. Furthermore, the intensities of the bands attributed to ring deformation vibrations were slightly higher when the ionic liquid was supported on SiO$_2$ compared to the immobilization on Pt/SiO$_2$.

For pure BDiMIm the intensities of the bands at 490 and 880 cm^{-1}, which were assigned to the in plane vibrations of the alkyl rests and stretching vibrations of the methylene groups of the butyl chain were higher compared to the supported ionic liquid. This indicates that the ring deformation led to a slightly higher relative movement of the hydrogen atoms, while the in plane movements of the alkyl rest is more constrained (less moving) than in the free ionic liquid.
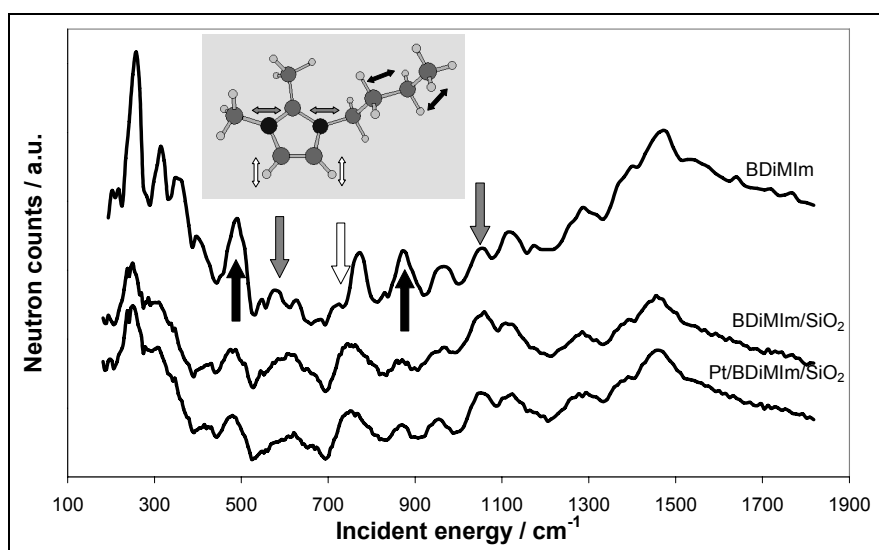
Figure 2-2   INS spectra of ionic liquid, ionic liquid supported on silica and supported ionic liquid on Pt/SiO$_2$

2.3.3. ^{1}H MAS NMR Spectroscopy

In the ^{1}H MAS NMR spectra of the ionic liquid immobilized on silica (Figure 2-3) a noticeable line broadening was observed relative to the pure ionic liquid (for assignments see Table 2-1). The highest increase in line width was observed for the peaks assigned to the methylene group at the nitrogen atoms, while the smallest line broadening was

observed for the terminal methyl and methylene groups of the alkyl chain. After temperature increase to 50 °C and 70 °C, the line-width was further reduced and a high-field shift of the peak assigned to the protons of imidazolium ring was observed. This peak was also shifted by the same value (0.1 ppm) when the ionic liquid was supported on Pt/SiO_2. However, differences in line-width were not observed when BDiMIm was supported on Pt/SiO_2 compared to $BDiMIm/SiO_2$.
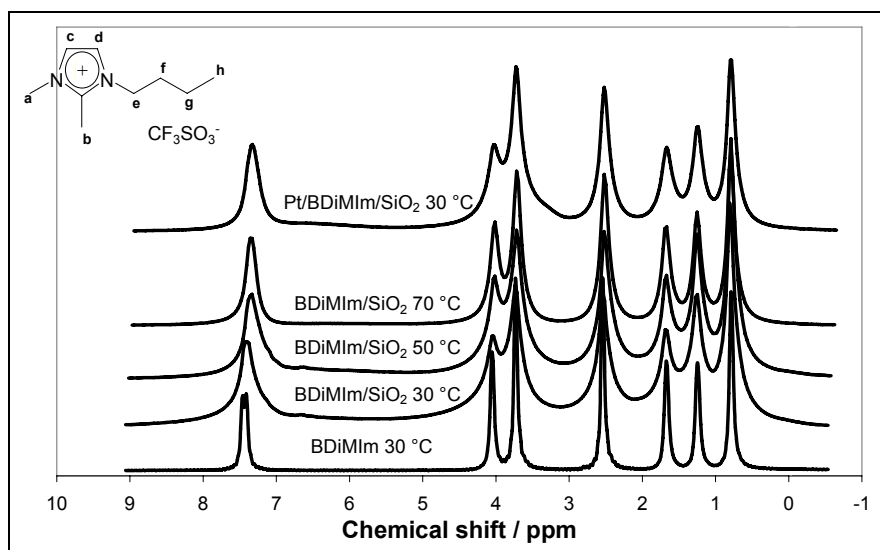
Figure 2-3   Solid state ^1H NMR spectra of pure BDiMIm, $BDiMIm/SiO_2$ at different temperatures and $Pt/BDiMIm/SiO_2$

Table 2-1   NMR peak assignment and full width at half maximum for pure BDiMIm, $BDiMIm/SiO_2$ at different temperatures and $Pt/BDiMIm/SiO_2$ (CS chemical shift / ppm; LW line-width / Hz)

| Assignment | BDiMIm | BDiMIm/SiO_2 | | | Pt/BDiMIm/SiO_2 |
| | 30 °C | 30 °C | 50 °C | 70 °C | 30 °C |
	CS (LW)	CS (LW)	CS (LW)	CS (LW)	CS (LW)
c	7.46 (25)	7.40 (152)	7.34 (119)	7.35 (86)	7.32 (145)
d	7.41 (27)				
e	4.05 (30)	4.05 (125)	4.02 (102)	4.02 (82)	4.02 (124)
a	3.73 (27)	3.73 (101)	3.72 (85)	3.71 (73)	3.72 (95)
b	2.54 (27)	2.53 (101)	2.52 (82)	2.51 (76)	2.52 (90)
f	1.67 (33)	1.67 (108)	1.67 (106)	1.68 (77)	1.66 (104)
g	1.24 (35)	1.25 (104)	1.25 (80)	1.25 (70)	1.24 (101)
h	0.78 (30)	0.80 (81)	0.78 (71)	0.79 (65)	0.79 (79)

2.3.4. *Transmission electron microscopy*

The TEM pictures of Pt clusters supported on silica and coated with 17 wt% ionic liquid at a magnification of 200.000 are shown in Figure 2-4a and the particle size distribution, which indicates a mean metal particle size of 2.1 nm is shown in Figure 2-4b.
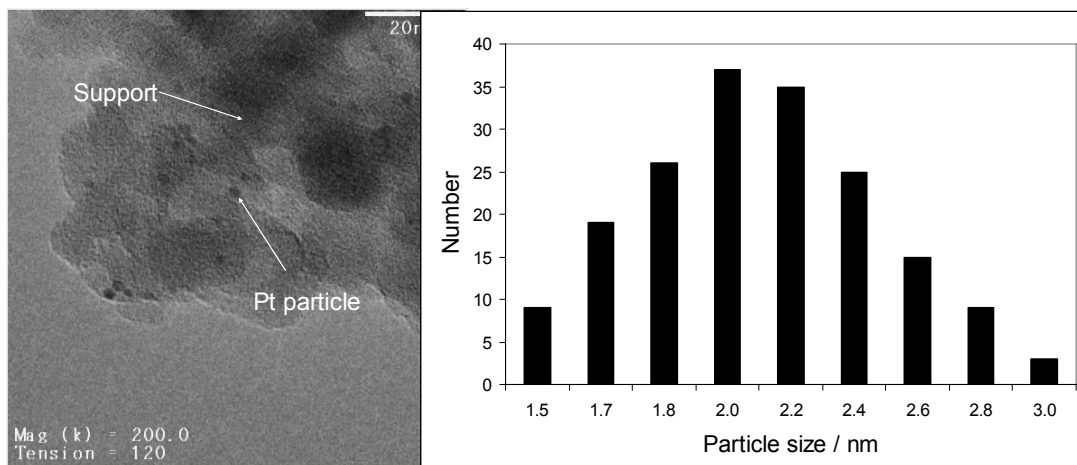
Figure 2-4   TEM picture (a) and particle size distribution (b) of an ionic liquid coated supported platinum catalyst

2.3.5. *X-ray absorption near edge structure and extended X-ray absorption fine structure*

To determine the influence of the ionic liquid on electronical structure of the metal clusters Pt/SiO_2 and $Pt/BDiMIm/SiO_2$, coated with 17 wt% of BDiMIm, were investigated by XANES and EXAFS.

The X-ray absorption spectra at the L_{III} edge (shown in Figure 2-5) show that the intensity of the peak above the edge is higher for the Pt/SiO_2 catalyst compared to $Pt/BDiMIm/SiO_2$ and the Pt-reference foil.
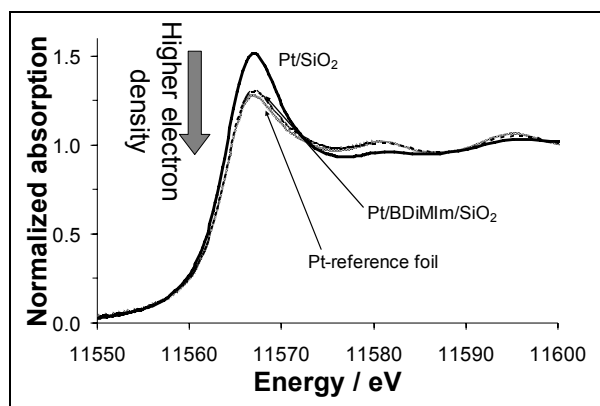
Figure 2-5   XANES of an uncoated catalyst (Pt/SiO$_2$), a coated catalyst (Pt/BDiMIm/SiO$_2$) and a Pt foil

Figure 2-6 compiles the Fourier-transformed EXAFS of the uncoated (Figure 2-6a) and the coated catalyst (Figure 2-6b). The number of neighbours (coordination number CN), their distance (r), the Debye-Waller factor (σ^2) and the zero energy correction (E$_0$) were calculated from the EXAFS and are shown in Table 2-2. The results indicate that oxygen neighbouring atoms can only be found for the uncoated catalyst. Also the coordination number for Pt neighbouring atoms was half compared with the coated catalyst.
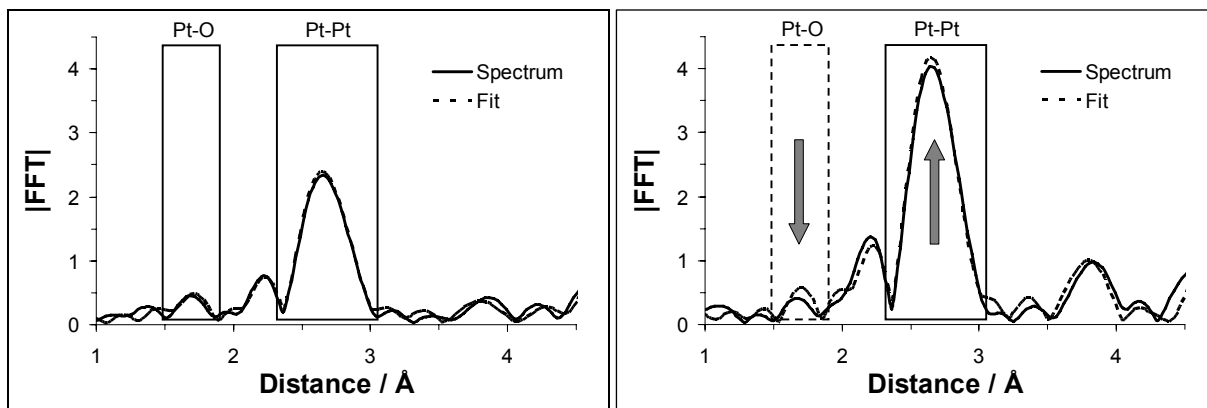
Figure 2-6   Measured and calculated Fourier-transformed EXAFS of Pt/SiO$_2$ (a) and Pt/BDiMIm/SiO$_2$ (b)

Table 2-2   EXAFS curve fitting results for Pt/SiO$_2$ and Pt/BDiMIm/SiO$_2$

	Pt/SiO$_2$	Pt/BDiMIm/SiO$_2$
r_{PtO} [Å]	2.05	2.15
CN_{Pt-O}	0.81	0.0
σ^2	0.0021	0.01619
E_0 [eV]	16.18	18.47
r_{PtPt} [Å]	2.77	2.76
CN_{Pt-Pt}	4.4	8.9
σ^2	0.0033	0.0033
E_0 [eV]	13.23	10.98

The particle size was determined from the average coordination number of the nearest metallic neighboring atoms assuming cuboctahedral geometry.[18] For Pt/SiO$_2$ the particle size was 0.9 nm, corresponding to a dispersion of 0.9 and for Pt/BDiMIm/SiO$_2$ a particle size of 1.95 nm was determined indicating a dispersion of 0.6.

2.3.6.   *Catalytic hydrogenation of ethene*

The activity of the uncoated and coated catalysts as function of the temperature is shown in Figure 2-7. The reaction was zero order with respect to ethylene. The activation energy 42 kJ/mol and 40 kJ/mol, respectively, was calculated using rates from experiments with a conversion below 25 %. (Note that for reactions with 0 order there is no difference between rates determined by a differential and integral analysis). The stability of the coated catalyst was followed at 70 °C after the series of kinetic experiments carried out up to 90 °C, showing a constant rate over 36 hours.
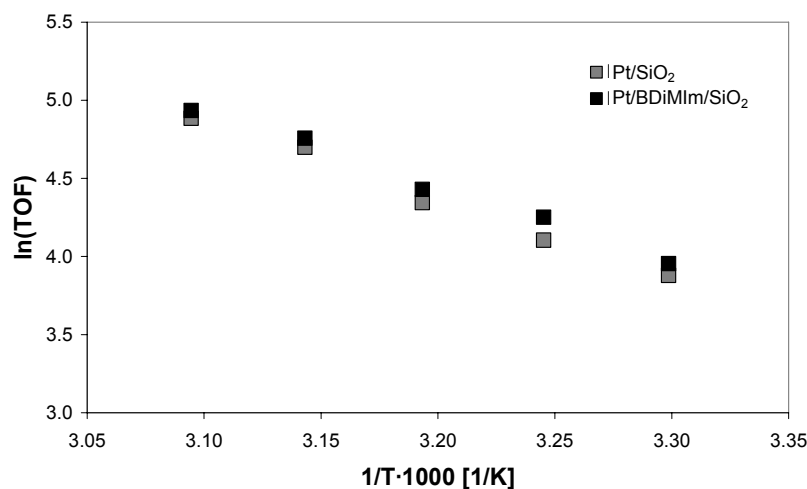
Figure 2-7   Catalytic activities for Pt/SiO$_2$ and Pt/BDiMIm/SiO$_2$

2.4. Discussion

Supported ionic liquids have been concluded to assume relative ordered states in the presence of metal organic complexes.[9] The exact degree of coordination of the ions to the dissolved and suspended substrates are unknown, but the question arises whether or not such phenomena are confined solely to metal complexes and particles or if reacting molecules would also induce locally such phenomena, when dissolved in an IL. The most important feature of such ordering phenomena for catalysis is not the overall long range ordering, but the direct interactions determining the critical properties as sorbent and catalyst. Thus, we focus in the present case on the characterization of the interactions between the ionic liquid, the support and the Pt particles using molecular spectroscopy.

For Pt on silica the intensity of the band characteristic for SiOH groups decreased by 20 % compared with the silica before impregnation. On first sight this may be attributed to dehydration of SiO$_2$ during the activation and reduction in hydrogen, since the treatment of SiO$_2$ at the same conditions (pH, Cl$^-$ concentration and temperature) lead to a similar result. However, it is striking that the perturbed OH bands (indicating hydrogen bonding between OH groups) are affected most. This indicates that the Pt particles are preferentially anchored at sites with a higher SiOH concentration, i.e., at parts of the support containing more defects. In contrast, the decrease of the band of the unperturbed

free SiOH groups at 3740 cm^{-1} was relatively small suggesting that the role of these OH groups in the anchoring of the Pt particles is negligible.

The disappearance of the band of terminal SiOH groups after coating SiO$_2$ with the ionic liquid indicates the complete coverage of the silica surface. The appearance of a new band at 3390 cm^{-1} for BDiMIm/SiO$_2$ and 3372 cm^{-1} for Pt/BDiMIm/SiO$_2$ characteristic of perturbed OH vibrations led us to conclude that the interactions between the ionic liquid film and the silica occurred *via* hydrogen bonds. The difference of 18 cm^{-1} between these two bands suggests slightly stronger hydrogen bonding when BDiMIm is supported on Pt/SiO$_2$. The reasons for this stronger interactions with the trifluoromethane sulphonate anions could be caused by the more pronounced interactions of 1-butyl-2,3-dimethyl-imidazolium cations with the metal particles. These interactions in turn allow a stronger coordination of anions to OH groups.

This conclusion is indirectly supported by the INS spectra. In these spectra the bands assigned to the deformation vibrations of the imidazolium ring increased in intensity. The increase in intensity is attributed to stronger relative displacements of the hydrogen atoms (stronger vibrations). The coordination of the basic CF$_3$SO$_3^-$ anions to the weakly acidic surface hydroxyl and the stronger interaction with the metal particle allows for a stronger displacement of the C-H vibrations. The shift of the band at 580 cm^{-1} to 610 cm^{-1} is attributed to these interactions constraining the deformation vibration of the imidazolium ring.

The line broadening observed in the NMR spectra of the supported catalysts can be attributed to differences in the T2 relaxation time that are not affected by MAS-NMR and therefore, can be used to determine the mobility of specific atomic groups.[19-21] The immobilization of the ionic liquid on the support leads to a lower mobility of the molecules and thus to an increased viscosity. Especially the nitrogen bound methylene group was affected. This was also detected by INS as the intensities of the bands ascribed to the in plane vibrations of the alkyl rests (490 cm^{-1}) decreased for the supported ionic liquid compared with the pure BDiMIm. Differences in line width were not observed when BDiMIm was supported on Pt/SiO$_2$ compared to BDiMIm/SiO$_2$, since the amount of 1 wt% of Pt on the surface is not enough to cause a further increase in viscosity. However, for a sample with a metal loading of 5 wt% a noticeable line broadening was

observed (results not reported here). After temperature increase, the line-width was reduced, as the mobility of the molecules increased due to the thermal energy. The peak assigned to the protons of the imidazolium shifted to a higher field after increasing the temperature.

In line with IR and INS, the ^{1}H MAS-NMR spectra show that upon immobilization of the ionic liquid on Pt/SiO$_2$ the protons of the imidazolium shifted to a higher field (i. e. to a 0.1 ppm downwards shift) compared to the IL supported on SiO$_2$ only. This is attributed to an increased electron density of the imidazolium ring leading to a higher shielding of the protons. As the hydrogen bonds between the ionic liquid and the surface of the support occur *via* CF$_3$SO$_3^-$ anions, the stronger bonding of the imidazolium ring to Pt, the higher the availability and base strength of the anion will be.

For the sample with 1 wt% metal loading TEM revealed that the particles were highly dispersed and that agglomerates of the metal clusters were not formed. The particle size determined by transmission electron microscopy (2.1 nm) was in good agreement with the particle size calculated from the EXAFS data (1.95 nm). The comparison of the XANES at the L$_{III}$ edge of the prepared catalysts and the reference foil indicated a higher oxidation state for the uncoated Pt/SiO$_2$ catalyst, which was also confirmed by the EXAFS containing Pt-O contributions for the Pt/SiO$_2$ catalyst. The Pt cluster particle size was reduced to 0.9 nm, but the fact that the Pt-Pt distance did not increase for the Pt/SiO$_2$ catalyst compared the bulk metal foil indicates that oxygen neighbouring atoms are in the outer shell of the Pt clusters only. In contrast, the Pt particles in the coated system were in zero oxidation state, as neighbouring oxygen atoms were not found and the XANES was identical to that of bulk Pt. This illustrates that the use of the ionic liquid protects the metal clusters from oxidation under typical sample handling conditions.

Hydrogenation of ethene showed zero order in ethene and first order (concluded from preliminary measurements) in hydrogen in a temperature interval from 30 to 50 °C. This is in perfect agreement with the literature for Pt supported on silica.[22] It is generally accepted that the reaction proceeds via the Horiuti-Polanyi mechanism.[23] According to this mechanism ethene adsorbs associatively on the metal surface, while hydrogen adsorbs dissociatively. The first order in hydrogen points to a nearly simultaneous addition of hydrogen in the rate determining step. It has been shown[23] that the sites for

ethene and hydrogen are not identical, i.e., under the conditions used the adsorption is non-competitive. The zero order in ethene indicates that the surface of the metal particles is essentially covered with ethene. This is remarkable, as the ionic liquid is present in very large excess compared to ethene. In the absence of detailed information on the heat of adsorption of the ionic liquid on metal surfaces, we speculate that the smaller size of ethene and the fact that it can form a di-σ-sorbed adsorbed state leads to a better stabilization compared with the π bonding of the imidazolium ion.

2.5. Conclusions

The detailed analysis of the supported platinum catalysts coated with a thin film of BDiMIm gave an insight to the interactions of the ionic liquid with the oxide support and the metal clusters. The spectroscopy confirmed that the vibrations of the imidazolium ring of the SiO_2 supported ionic liquid were less restricted, whereas the viscosity of the ionic liquid increased. This will have a strong impact on the diffusivity of reactants to the active sites, allowing tailoring the selectivity towards certain products. The presence of platinum clusters further modified the electron density of the ionic liquid, which changes the polarity of the ionic liquid within certain limits and can also be used to improve the selectivity. In addition, the complete coverage of the catalyst surface including the metal particles with the ionic liquid protects the catalyst from oxidation, which can be further utilized to protect air sensitive catalysts. The similar catalytic activity of the coated catalyst for ethene hydrogenation at low temperatures shows that the ionic liquid does not block the access of hydrogen or ethane to the active sites. This is important aspect which indicates that the interaction of the ionic liquid and the Pt surface is weaker compared to the reactant molecules and therefore, potential transport limitations resulting from a low solubility of reactants did not occur. This opens new possibilities for the selective hydrogenation of unsaturated compounds as the properties of the metal and of the reaction environment can be subtly tuned *via* the ionic liquid.

Acknowledgements

2.6. References

[1]   A. Riisager, R. Fehrmann, S. Flicker, R. van Hal, M. Haumann, P. Wasserscheid, *Angew. Chem., Int. Ed.* **2005**, *44*, 815.

[2]   O. Jimenez, T. E. Muller, C. Sievers, A. Spirkl, J. A. Lercher, *Chem. Commun.* **2006**, 2974.

[3]   C. Sievers, O. Jimenez, R. Knapp, X. Lin, T. E. Muller, A. Turler, B. Wierczinski, J. A. Lercher, *J. Mol. Catal. A: Chem.* **2008**, *279*, 187.

[4]   H. L. Pelt, J. Brockhus, R. P. J. Verburg, J. J. F. Scholten, *J. Mol. Catal.* **1985**, *31*, 107.

[5]   J. P. Arhancet, M. E. Davis, J. S. Merola, B. E. Hanson, *J. Catal.* **1990**, *121*, 327.

[6]   C. P. Mehnert, E. J. Mozeleski, R. A. Cook, *Chem. Commun.* **2002**, 3010.

[7]   T. Welton, *Coord. Chem. Rev.* **2004**, *248*, 2459.

[8]   R. Atkin, G. G. Warr, *J. Am. Chem. Soc.* **2005**, *127*, 11940.

[9]   C. Sievers, O. Jimenez, T. E. Muller, S. Steuernagel, J. A. Lercher, *J. Am. Chem. Soc.* **2006**, *128*, 13990.

[10]   A. Wolfson, I. F. J. Vankelecom, P. A. Jacobs, *Tetrahedron Lett.* **2003**, *44*, 1195.

[11]   H. Hagiwara, Y. Sugawara, K. Isobe, T. Hoshi, T. Suzuki, *Org. Lett.* **2004**, *6*, 2325.

[12]   M. J. Frisch, G. W. Trucks, H. B. Schlegel, G. E. Scuseria, M. A. Robb, J. R. Cheeseman, J. Montgomery, J. A., T. Vreven, K. N. Kudin, J. C. Burant, J. M.

Millam, S. S. Iyengar, J. Tomasi, V. Barone, B. Mennucci, M. Cossi, G. Scalmani, N. Rega, G. A. Petersson, H. Nakatsuji, M. E. Hada, M., K. Toyota, R. Fukuda, J. Hasegawa, M. Ishida, T. Nakajima, Y. Honda, O. Kitao, H. Nakai, M. Klene, X. Li, J. E. Knox, H. P. Hratchian, J. B. Cross, V. Bakken, C. Adamo, J. Jaramillo, R. Gomperts, R. E. Stratmann, O. Yazyev, A. J. Austin, R. Cammi, C. Pomelli, J. W. Ochterski, P. Y. Ayala, K. Morokuma, G. A. Voth, P. Salvador, J. J. Dannenberg, V. G. Zakrzewski, S. Dapprich, A. D. Daniels, M. C. Strain, O. Farkas, D. K. Malick, A. D. Rabuck, K. Raghavachari, J. B. Foresman, J. V. Ortiz, Q. Cui, A. G. Baboul, S. Clifford, J. Cioslowski, B. B. Stefanov, G. Liu, A. Liashenko, P. Piskorz, I. Komaromi, R. L. Martin, D. J. Fox, T. Keith, M. A. Al-Laham, C. Y. Peng, A. Nanayakkara, M. Challacombe, P. M. W. Gill, B. Johnson, W. Chen, M. W. Wong, C. Gonzalez, J. A. Pople, Gaussian, Inc, Wallingford CT, **2004**.

[13]   A. J. Ramirez-Cuesta, *Comput. Phys. Commun.* **2004**, *157*, 226.

[14]   K. V. Klementiev, VIPER for Windows, freeware: http://www.desy.de/~klmn/viper.html.

[15]   A. L. Ankudinov, B. Ravel, J. J. Rehr, S. D. Conradson, *Phys. Rev. B* **1998**, *58*, 7565.

[16]   A. L. Ankudinov, J. J. Rehr, *Phys. Rev. B* **2000**, *62*, 2437.

[17]   K. V. Klementiev, XANES dactyloscope, freeware: http://www.desy.de/~klmn/xanda.html.

[18]   R. E. Benfield, *J. Chem. Soc., Faraday Trans.* **1992**, *88*, 1107.

[19]   A. Johansson, J. Tegenfeldt, *J. Chem. Phys.* **1996**, *104*, 5317.

[20]   A. Lauenstein, J. Tegenfeldt, *J. Phys. Chem. B* **1997**, *101*, 3311.

[21]   R. Spindler, D. F. Shriver, *J. Am. Chem. Soc.* **1988**, *110*, 3036.

[22]   R. D. Cortright, S. A. Goddard, J. E. Rekoske, J. A. Dumesic, *J. Catal.* **1991**, *127*, 342.

[23]   I. Horiuti, M. Polanyi, *Trans. Faraday Soc.* **1934**, *30*, 1164.

Chapter 3.

Corrugated structure of ionic liquid surfaces with polymer stabilized platinum nanoparticles

Abstract

Ionic liquids such as 1-butyl-2,3-dimethyl-imidazolium trifluoromethane sulphonate stabilize complex structures of polyvinylpyrrolidone protected nanoparticles on their surface. The polyvinylpyrrolidone shell around the Pt nanoparticles remains intact, but the ionic liquid partly penetrates the protective layer and interacts with the metal. This leads to a pronounced increase of the viscosity of the ionic liquid, as observed also with metal complexes. The protected particles form small islands of aggregated moieties that are connected by interacting polymer strands, a process enhanced by diluting the sample in methanol during preparation. These ensembles segregate at the surface protruding significantly out from the bulk ionic liquid. The outermost layer of the surface, however, consists of the ionic liquid with the cation being on top and the SO_3 group of the anion underneath being oriented towards the bulk.

3.1. Introduction

The immobilization of organometallic complexes and metal nanoparticles in thin films of supported ionic liquid has been introduced as new concept to combine the high activity and selectivity of homogenous catalysts with the facile separation of solid catalysts.[1-4] Supported ionic liquid catalysts are prepared by impregnation of a porous support with an ionic liquid containing the catalytically active components. Such materials are an improved alternative to supported aqueous phase and supported liquid phase catalysts,[5] as the catalysts are particularly stable for gas phase reactions due to the low vapor pressure of the ionic liquid.[6] Catalysts with immobilized ionic liquids have successfully been used in different reactions such as achiral hydrogenation,[7] hydroformylation of olefins,[1] hydroamination,[2, 3] Heck-reaction,[8] and hydrogenation.[4, 9] The concept allows combining different functionalities in a single material as co-catalysts and stabilizing agents can be added to the ionic liquid phase.[3]

The properties of the catalyst can be fine-tuned by choosing an appropriate ionic liquid. Particularly, the solubility and, thus, the selectivity of the catalyst towards different reactants can be enhanced by adjusting the polarity of the ionic liquid. Ordering phenomena and domain formation of the ionic liquid have found to be induced by its interactions with the support as well as with the active component.[4, 10, 11] Especially strong interactions were observed with ionic liquid immobilized metal nanoparticles.[4, 12, 13] These metal nanoparticles can be either attached to the support or dispersed in the ionic liquid. Usually, the metal particles are formed by reduction of a salt or complex precursor *in situ* in the ionic liquid.[12]

A new method is presented here, whereby polymer stabilized metal nanoparticles[14] were prepared prior to the immobilization in the ionic liquid and then dispersed in it. An advantage of this method is that the particle size of the nanoparticles can be tuned by changing the conditions during their preparation. Here, we used an alcohol as reducing agent, but also hydrogen can be applied.[14] Depending on the alcohol, the reduction kinetics varies. Low molecular weight alcohols provide a higher reduction rate leading to smaller metal particles.[14]

This chapter describes a new surface corrugation of the ionic liquid BDiMIm (see Figure 3-1) with embedded Pt nanoparticles stabilized by polyvinylpyrrolidone (PVP). As the immobilized PVP stabilized metal nanoparticles in a supported film of ionic liquid are potential heterogeneous catalysts, the alignment of the ionic liquid and the nanoparticles at the surface of the ionic liquid is analyzed in detail by neutral impact collision ion scattering spectroscopy (NICISS). Special focus is laid on modeling of the local arrangement between the metal particle, the polymer and the ionic liquid.
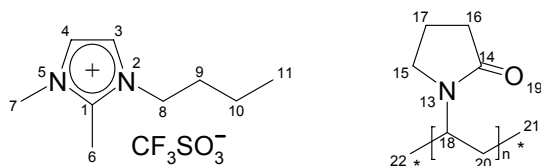
Figure 3-1: 1-Butyl-2,3-dimethyl-imidazolium trifluoromethane sulphonate (BDiMIm) and poly(n-vinyl-2-pyrrolidone) (PVP) (* indicates the end group of the polymer).

3.2. Experimental

3.2.1.   Materials

The ionic liquid 1-butyl-2,3-dimethyl-imidazolium trifluoromethane sulphonate (BDiMIm) (99 %) with maximum water and halide content of 48 and 103 ppm, respectively, was kindly provided by Solvent Innovation GmbH. Chloroplatinic acid hexahydrate (Pt content $\geq$ 37.5 %), polyvinylpyrrolidone (average molecular weight 40,000 g$^-$mol^{-1}) propanol (99.5 %) and methanol (99.8 %) were obtained from Aldrich. The silica support Aerosil 355 was provided by Degussa AG. All chemicals were used as received.

3.2.2.   Preparation of Pt nanoparticles

PVP coated Pt nanoparticles were synthesized according to the preparation method proposed by Busser et al.[14] and Teranishi et al..[15]

For the Busser method, chloroplatinic acid hexahydrate (0.032 g, 0.0615 mmol) and PVP (0.068 g, 0.615 mmol) were dissolved in 20 mL bidistilled water. The mixture was heated to 100 °C for 2 h. This mixture was rapidly mixed with 1-propanol (120 mL) and heated to 110 °C. After 48 h at 110 °C the colloidal solution was cooled with liquid nitrogen, the solvent was evaporated under vacuum, while the sample was warming up slowly, and the resulting residue was re-dissolved in 7 mL methanol. Finally BDiMIm (0.187 g, 0.615 mmol) was added to the solution.

To prove the benefits of the mixing step at 100 °C Pt nanoparticles were also prepared according to the Teranishi method, where chloroplatinic acid hexahydrate (0.032 g, 0.0615 mmol) and PVP (0.068 g, 0.615 mmol) were directly dissolved in a mixture of bidistilled water (20 mL) and 1-propanol (120 mL). The solution was heated to 110 °C for 3 h. Afterwards the sample was treated analogous to the sample prepared by the first method.

3.2.3. Preparation of supported Pt nanoparticles

For preparing a supported ionic liquid catalyst the silica support was added to the Pt/PVP/BDiMIm solution. The suspension (containing 1 wt. % Pt) was stirred at room temperature for 10 min and the volatile components were removed slowly by freeze drying to give a free flowing grey powder (Pt/PVP/BDiMIm/SiO$_2$).

A silica supported ionic liquid was prepared by adding SiO$_2$ into a solution of BDiMIm dissolved in methanol. After stirring for 10 min, the suspension was freeze dried to give a free flowing white powder (BDiMIm/SiO$_2$).

A silica supported ionic liquid containing PVP was prepared by adding SiO$_2$ into a solution of BDiMIm and PVP in methanol. After stirring for 10 min, the solvent was removed by freeze drying to give a free flowing white powder (PVP/BDiMIm/SiO$_2$).

3.2.4. Characterization of materials

Neutral Impact Collision Ion Scattering Spectroscopy (NICISS). NICISS uses the energy loss of ions being back scattered from soft matter targets under a specified

scattering angle. For the results presented in this work the scattering angle was fixed to 168°. The method was applied to determine the elemental composition and elemental concentration depth profiles of the investigated liquid surfaces.

The back scattering process can be described in a good approximation as a classical collision between two collision partners, in which the He projectiles lose a part of their kinetic energy. At a fixed scattering geometry, this elastic energy loss only depends on the mass ratio of the hit target atom and the projectile. On their trajectory through the bulk the He projectiles suffer an additional energy loss with a magnitude proportional to the depth of the target atom. This inelastic energy loss is caused by small angle scattering and electronic excitation and has been calibrated with self-assembled monolayers of alkanethiolates on gold and silver single crystals.[16]

The observation depth of the target atoms depends on the elemental composition of the liquid sample and is limited by the widening of the ion beam in the bulk due to small-angle scattering. Hence, the observation depth is up to 200 Å with a depth resolution far below 10 Å. The energy of the back-scattered ions is determined by their time-of-flight (TOF) from the target to the detector. A more detailed explanation of the method in general and the experimental setup has been described elsewhere.[17]

In general, the measured TOF spectra are composed of two different signals that have to be separated. The signals are attributed to recoil-hydrogen and backscattered projectiles (neutral and ionic helium). The hydrogen background is fitted by a polynomial function and subtracted from the TOF spectrum. The backscattered projectiles lead to step like signals. Since the mass of the projectiles is constant, each step in the spectrum can be attributed to an element.

For estimating the concentration depth profiles of each element, the elemental profiles on the time scale can be considered as energy loss spectra. The inelastic energy loss per unit of length is defined as stopping power. The stopping power depends on the ion species, the sample composition and the primary energy of the projectile. If the stopping power is known as function of the primary energy of the projectile, the penetration depth of the ions can be calculated from the energy loss. Note that the back-scattered projectiles from the outermost surface layer have not suffered an inelastic energy loss.

The elemental profiles on the time scale can be considered as a convolution (of Gauss functions) due to the energetic width of the primary ion beam and its broadening in the bulk of the sample. The beam widening in the bulk can be simulated by Gauss functions that are broadened with increasing depth of the hit target atom. To obtain an improved resolution the spectra have to be deconvoluted. The mathematical operations to calculate the depth profiles from the TOF spectra have been discussed by Andersson *et al.*.[18]

In this work, Helium ions with a primary energy of 4.5 keV were used leading to a dose of about 10^{11} He ions/cm^2. Compared with the typical number of atoms in a surface of about 10^{14} atoms/cm^2, the damage of the surface by the impinging ions can be neglected. All NICISS measurements presented here were performed at 293 K measured with a Pt-resistance thermometer. During the measurements the pressure in the vacuum chamber was below $5 \cdot 10^{-5}$ mbar.

By applying the angle resolved mode of NICISS (ARNICISS) the incident angle of the projectiles is varied (Figure 3-2). The TOF spectra become more surface sensitive with lowering the incident angle. The results of ARNICISS measurements yield the possibility to determine the local topography around atoms in soft matter and to develop a 3-dimensional model of the surface structure that is also discussed in this work. In the case of a plane and lateral homogeneous surface the concentration depth profiles show the following behavior. The lower the incident angle the concentration depth profiles are shifted into greater depths and are broadened. Both effects are only apparent due to the scaling of the depth scale with the sine of the incident angle. If angle resolved concentration depth profiles does not show the even described behavior, the surface is structured.
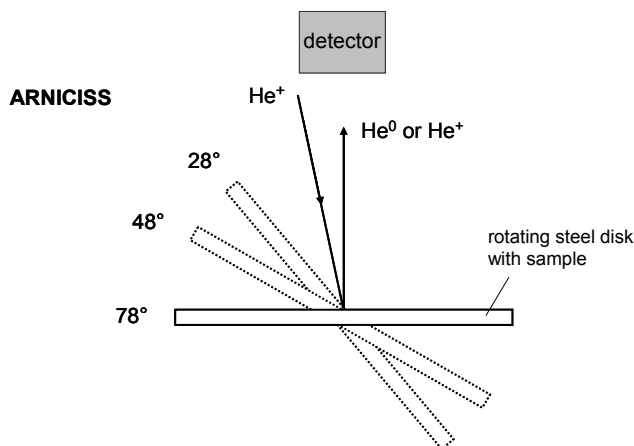
Figure 3-2: Sketch of the experimental setup of the ARNICISS measurements and definition of the incident angle of the ion beam.

For the measurements 60 µL of the Pt/PVP/BDiMIm solution (*vide supra*, undiluted or diluted with methanol in a ratio of 1:2 and 1:5, ultrasonically dispersed) were spread on a graphite target (20 mm diameter). The NICISS measurements were performed after evaporation of the solvent. The thicknesses of the resulting layers were 3.4 µm (undiluted), 1.1 µm (1:2 diluted) and 0.55 µm (1:5 diluted). The target with the sample was mounted on a rotating steel disk during NICISS measurements.

Transmission electron microscopy (TEM). For obtaining TEM images, the samples were diluted in methanol and ultrasonically dispersed. Drops of the dispersions were applied on a copper-grid supported carbon film. Micrographs were recorded on a JEM-2010 Jeol transmission electron microscope operating at 120 kV. The particle size distributions were determined by optical inspection of the photographs. At least 150 particles were counted per sample.

NMR Spectroscopy. Interactions of the Pt nanoparticles with the polymer and the ionic liquid were studied with ^{1}H and ^{13}C NMR spectroscopy. Three solutions of the polymer stabilized colloid particles in CD_3OD were prepared, whereby ionic liquid was added to the second sample, and a mixture of the ionic liquid and the polymer to the third sample. Spectra were recorded at ambient conditions using a Bruker spectrometer operating at 360 and 90 MHz, respectively, using a high-resolution 5-mm probe head for liquid samples. Furthermore ^{1}H NMR spectra of the parent ionic liquid and the ionic liquid

containing stabilized Pt particles were recorded on the 360 MHz Bruker spectrometer using a double walled NMR tube, which was charged with D_2O in the outer sample space.

For solid state NMR, the samples were packed in 4 mm ZrO_2 rotors. ^1H MAS NMR measurements were performed on a Bruker AV500 spectrometer ($B_0 = 14.1$ T) with a spinning rate of 15 kHz. For temperature adjustment, the bearing and drive gas stream were passed through a heat exchanger. The spectra were recorded as the sum of 100 scans using single pulse excitation with a pulse length of 2.6 µs and recycle time of 3 s.

Atomic force microscopy (AFM). AFM images were taken with a Veeco Multimode AFM using a Nanoscope IIIa SPM controller in the tapping mode. AFM probes (204-497 kHz, 10-130 N m^{-1}, tip radius < 7 nm) were purchased from Nanosensors. 5×5 µm images were recorded with 256 data points per line at a scanning frequency of 1 Hz. For the measurements 60 µL of the sample were spread on a n-doped Si(100) target (10 mm diameter) at room temperature.

3.2.5.   Catalytic activity

The hydrogenation of ethylene was studied for Pt/PVP/BDiMIm/SiO$_2$ 30 and 50 °C with a hydrogen to ethylene ratio of 2.5 : 1 in a fixed bed reactor filled with 0.1 mg catalyst (diluted with SiO$_2$ and SiC). The products were analyzed using a Shimadzu GC-2014 gas chromatograph.

3.3. Results

3.3.1.   Transmission electron microscopy

Pt sols were prepared by reduction of aqueous chloroplatinic acid with alcohols in the presence of PVP as stabilizer. A typical TEM micrograph of the Pt sol is depicted in Figure 3-3 indicating a mean particle size of ca. 2.2 nm. Closer inspection of the TEM images indicated that frequently several nanoparticles were in vicinity to each other, whereas single nanoparticles were the exception. To probe whether or not this

observation is related to the sample preparation, the TEM specimens were prepared from a highly diluted suspension of the Pt particles (Figure 3-4). Even under such conditions Pt nanoparticles were always closely associated with each other.
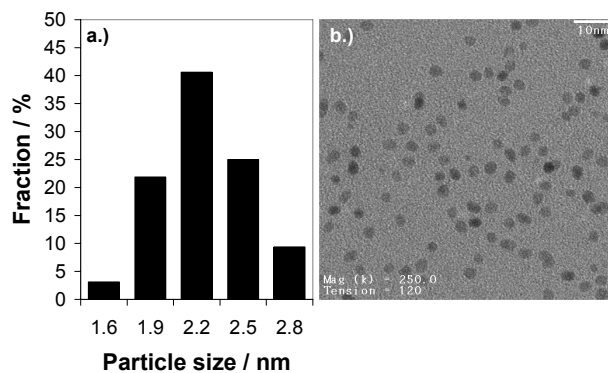
Figure 3-3: Particle size distribution (a) and TEM image (b) of PVP stabilized Pt nanoparticles (undiluted)
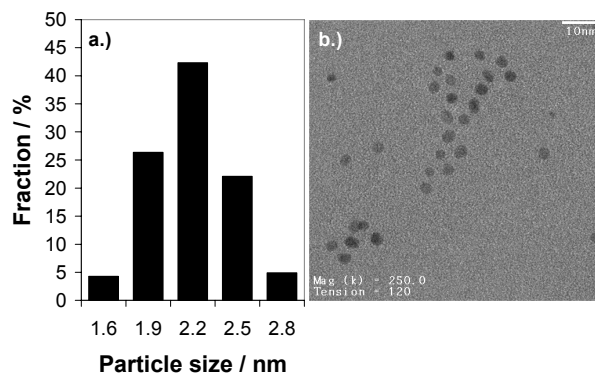
Figure 3-4: Particle size distribution (a) and TEM image (b) of PVP stabilized Pt nanoparticles (1:5 diluted)

3.3.2. *Liquid and solid state NMR spectroscopy*

^{1}H or ^{13}C NMR spectroscopy was used to characterize the strength of the interaction between the polymer and the ionic liquid. Spectra of a solution of the stabilized Pt clusters in methanol-d4 were recorded. For comparison, also NMR spectra of solutions of BDiMIm and a mixture of PVP and BDiMIm were measured. Differences in the chemical

shifts for the polymer and the ionic liquid were not observed in the ^{1}H or ^{13}C NMR spectra. Furthermore NMR spectra of the parent ionic liquid and of the ionic liquid containing Pt/PVP were recorded. While the signals of the parent ionic liquid were well resolved, a considerable line broadening was observed for the sample containing Pt nanoparticles (Figure 3-5). As illustration of this broadening note the absence of the triplet for the protons of C11 (for the numbering, see Figure 3-1 and Table 3-1). The line width observed for the protons of C7 increased from 6 to 27 Hz. In the sample containing Pt, also two signals below 4 ppm were observed and attributed to PVP.
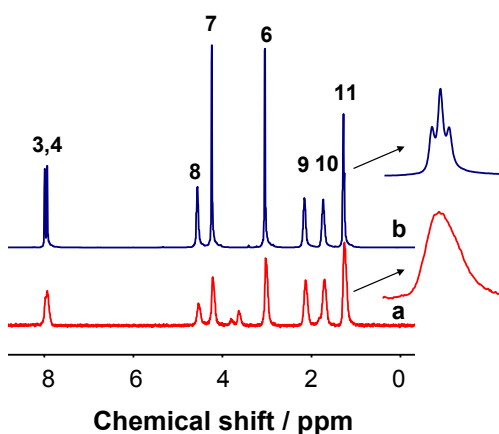
Figure 3-5: ^{1}H NMR spectra of a solution of (a) Pt/PVP/BDiMIm and (b) the parent ionic liquid BDiMIm.

When BDiMIm was immobilized on silica, a noticeable line broadening in the ^{1}H MAS NMR spectra relative to the parent ionic liquid was observed (Figure 3-6). The peak positions, the assignments and the line width are compiled in Table 3-1. The highest increase in line width was found for the peaks assigned to the methylene group at the nitrogen atom (C8), while the least line broadening was observed for the terminal methyl and methylene groups of the alkyl chain. This line broadening indicates reduced mobility of the imidazolium cation, when the ionic liquid forms a thin film on SiO_2.[11]

To test, if PVP or Pt/PVP have an impact on the mobility of the supported ionic liquid, the ^{1}H MAS NMR spectra of PVP/BDiMIm/SiO_2 and Pt/PVP/BDiMIm/SiO_2 were also recorded. The presence of PVP did not lead to further increase of the line width, while

dispersed Pt/PVP led to a marked increase of the line width compared to the other samples.
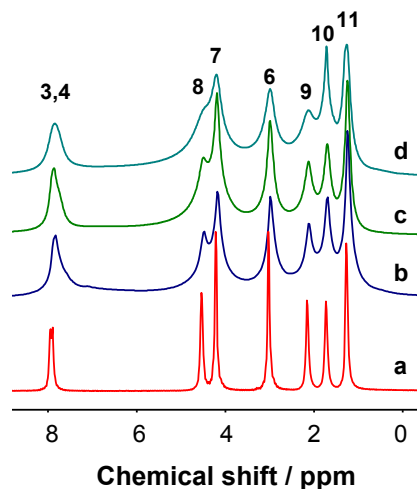
Figure 3-6:   Solid state ^{1}H NMR spectra of BDiMIm (a), BDiMIm/SiO$_2$ (b), PVP/BDiMIm/SiO$_2$ (c) and Pt/PVP/BDiMIm/SiO$_2$ (d).

Table 3-1:   Signal position, width at half maximum and assignment for the ^{1}H MAS NMR spectra of BDiMIm, BDiMIm/SiO$_2$, PVP/BDiMIm/SiO$_2$ and Pt/PVP/BDiMIm/SiO$_2$ (CS chemical shift / ppm; LW line-width / Hz).

Assignment	BDiMIm CS (LW)	BDiMIm/SiO$_2$ CS (LW)	PVP/BDiMIm/SiO$_2$ CS (LW)	Pt/PVP/BDiMIm/SiO$_2$ CS (LW)
4	7.46 (25)	7.40 (152)	7.40 (151)	7.40 (205)
3	7.41 (27)			
8	4.05 (30)	4.05 (125)	4.05 (122)	4.05 (180)
7	3.73 (27)	3.73 (101)	3.73 (96)	3.73 (134)
6	2.54 (27)	2.53 (101)	2.53 (102)	2.53 (126)
9	1.67 (33)	1.67 (108)	1.67 (105)	1.67 (140)
10	1.24 (35)	1.25 (104)	1.25 (103)	1.25 (133)
11	0.78 (30)	0.80 (81)	0.80 (80)	0.80 (103)

The signal assignments for the NMR spectra recorded in MeOH-d4 are given in Table 3-2 and Table 3-3. The ^{13}C signal of BDiMIm atom number 8 is overlaid by the signal of the solvent (methanol). ^{13}C signals of PVP atoms number 20, 15 and 18 are expected at 35, 43 and 46 ppm, respectively.[25]

Table 3-2: Assignment of the ^{1}H NMR signals of solutions of BDiMIm and PVP in MeOH-d4 (CS chemical shift / ppm)

BDiMIm		PVP	
Assignment	CS	Assignment	CS
4	7.51 (d)		3.90
3	7.47 (d)	16, 18	3.76
8	4.10 (s)		3.32
7	3.83 (s)		2.44
6	2.63 (s)		2.30
9	1.81 (m)	15, 17, 20, 21, 22	2.05
10	1.41 (m)		1.75
11	1.00 (t)		1.52

Table 3-3: Assignment of the ^{13}C NMR signals of solutions of BDiMIm and PVP in MeOH-d4 (chemical shift / ppm)

BDiMIm		PVP	
Assignment	Chemical shift	Assignment	Chemical shift
1	144.8	14	176.8
4	122.6	18	---
3	121.1	15	---
8	---	20	---
9	34.3	16	31.5
7	31.8	17	18.2
10	19.5		
11	12.8		
6	8.4		

3.3.3. NICISS analysis

The spectra of the undiluted, the 1:2 and 1:5 diluted samples (dilution refers to treatment prior to the application on the graphite wafer; higher dilution ultimately reduces the thickness of the film applied) recorded at an incident angle of 78° plotted against the time of flight in μs are shown in Figure 3-7. Depending on the molar weight of the target atoms the He ions are scattered from, the time of flight varies. It decreases with increasing mass. The following signals in the TOF-spectra can be assigned to Pt (2.66 μs), S (3.32 μs), F (4.00 μs), O (4.33 μs), N (4.71 μs) and C (5.26 μs). Note that the TOF values given in the brackets are expected values.
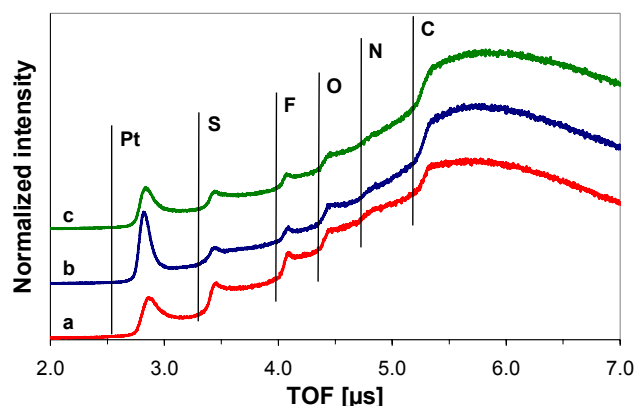
Figure 3-7: NICISS spectra recorded at an incident angle of 78° of (a) the undiluted sample as well as at 1:2 and 1:5 dilution (b and c, respectively). The spectra are vertically offset for clarity.

The angular dependence of the concentration depth profiles is depicted in Figure 3-8. It is apparent that the profiles vary strongly with the angle. For lower incident angles the profiles are flattened, which is particularly noticeable for the signal attributed to Pt.
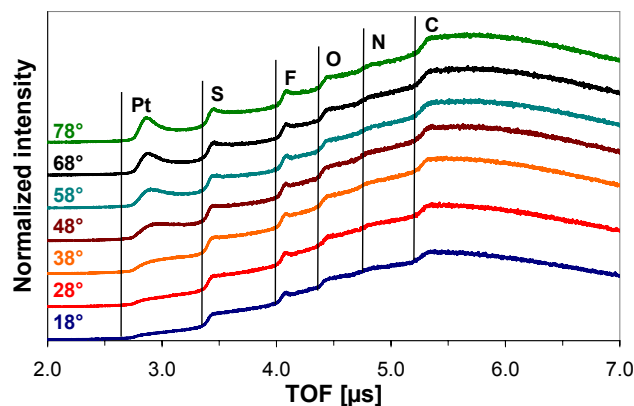
Figure 3-8: NICISS spectra of the PVP stabilized Pt nanoparticles in BDiMIm (undiluted sample) measured at different incident angles. The spectra are vertically offset for clarity.

From the TOF spectra, concentration depth profiles can be calculated as described above. Figure 3-9 shows these profiles for carbon, fluorine, sulfur and platinum at 78° and 18° incident ion beam angle. Note that the concentration of each element was normalized to its bulk density. For each element a maximum was observed at a certain

depth below the sample/gas interface, i.e., at an incident ion beam angle of 78°, a weak maximum due to carbon occurred at a depth of 4.2 Å, fluorine at 6.9 Å, sulfur at 11.1 Å and a very broad and intense signal attributed to Pt at around 51.4 Å. When changing the incident ion beam angle to 18°, the maximum of the carbon signal mildly changed to a depth of 3.6 Å. No change in depth was observed for the fluorine and sulfur signal. The intensity of the fluorine signal, however, increased. The most obvious change was observed for the Pt profile, as the peak was flattened and a clear maximum cannot be identified.
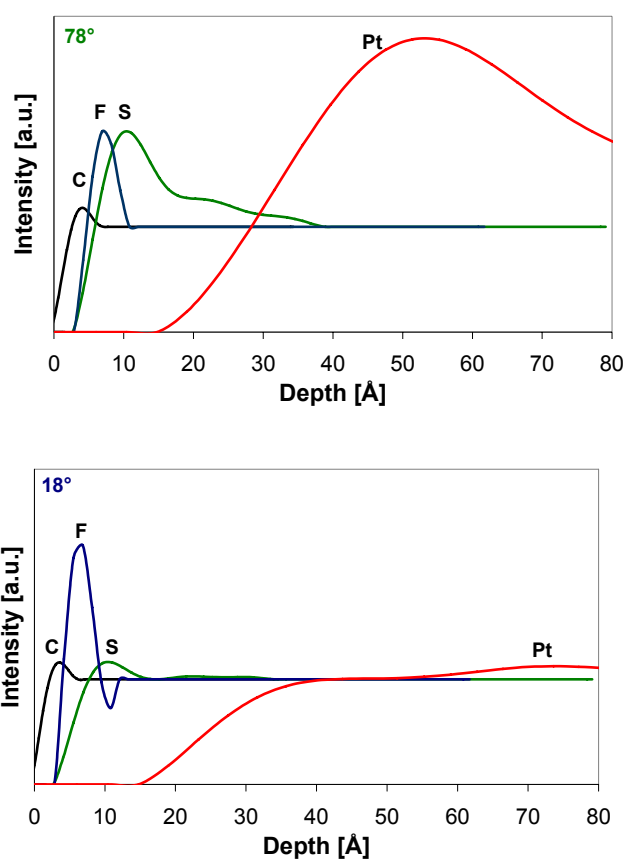
Figure 3-9: Depth profile of C, F, S and Pt for an undiluted sample at an incident angle of 78° (upper) and of 18° (lower graph).

Upon dilution of the samples with methanol (1:2 and 1:5) prior to the NICISS investigations the maximum of the Pt signal was shifted to lower depth (37.5 and 41.5 Å

for the 1:2 and 1:5 dilutions, respectively). The maximum in the fluorine signal increased relative to the maximum in the Pt signal as well as relative to the bulk signal.

The profiles for carbon, fluorine and platinum at 78° and 18° incident ion beam for the 1:5 diluted sample are shown in Figure 3-10.
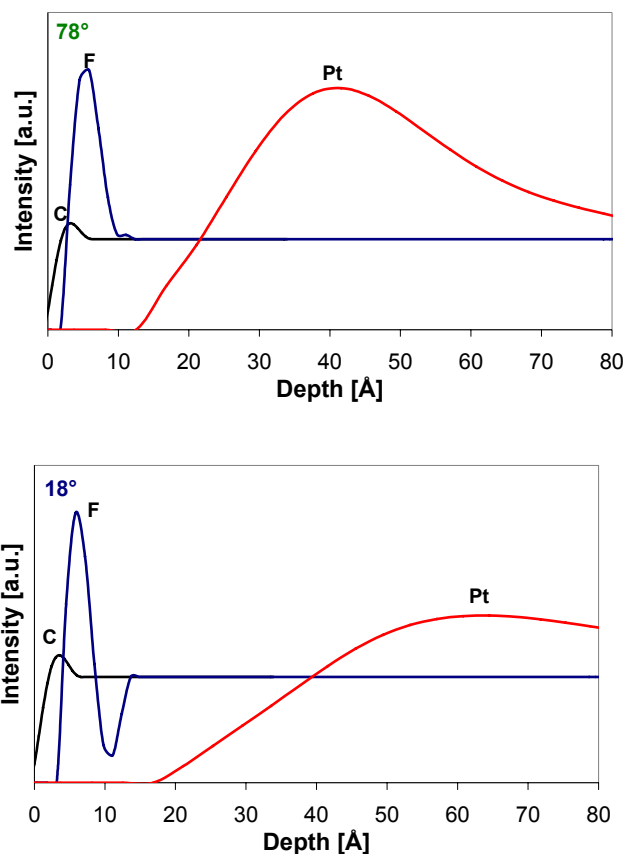
Figure 3-10: Depth profile of C, F, S and Pt for a 1:5 diluted sample at an incident angle of 78° (upper) and of 18° (lower graph).

If the angle between the ion beam and the surface of the sample is close to the surface normal, Pt is observed at a depth equal to the polymer and ionic liquid film thickness. For lower incident angles, the film thickness will apparently increase, as the path length of the He-ions through the ionic liquid and the polymer layer is longer (see Figure 3-11).
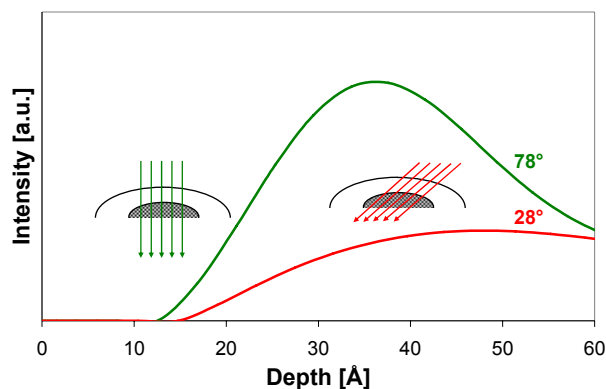
Figure 3-11:   Influence of the incidenct angle of the ion beam on the depth profile of Pt for PVP stabilized Pt nanoparticles in BDiMIm.

As discussed, a Pt/PVP sample prepared after a method by Teranishi *et al.*[15] was also studied for comparison. The results of the undiluted sample are very similar to the results presented above. However, after dilution of the sample with an eightfold amount of methanol the shape of the Pt profile and the angular dependence changed markedly, while the onset of the Pt signal was hardly shifted with angle. The signal for Pt did not saturate, but increased at large times of flight (corresponding to a depth of about 20 nm).

3.3.4.   Atomic force microscopy (AFM)

To further analyze the surface structure AFM images of PVP, BDiMIm, BDiMIm/PVP and Pt/PVP/BDiMIm were recorded. The 2D and 3D AFM images of Pt/BDiMIm/PVP (Figure 3-12) indicate that elevations of 8 to 10 nm can be found on the surface of the sample.
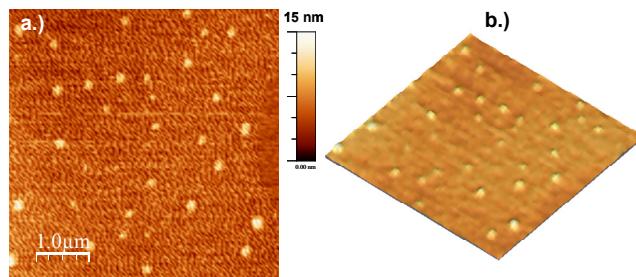
Figure 3-12: 2D (a.) and 3D (b.) AFM images of Pt/PVP/BDiMIm. (Further AFM images available in the supporting material)

The 2D and 3D AFM images of PVP, BDiMIm and a mixture of PVP and BDiMIm are given in Figure 3-13, Figure 3-14 and Figure 3-15, respectively.
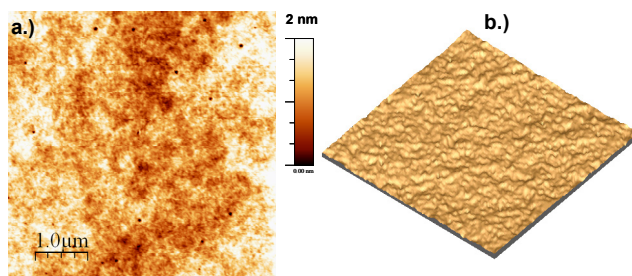
Figure 3-13: 2D (a.) and 3D (b.) AFM images of the surface of a thin film of PVP.
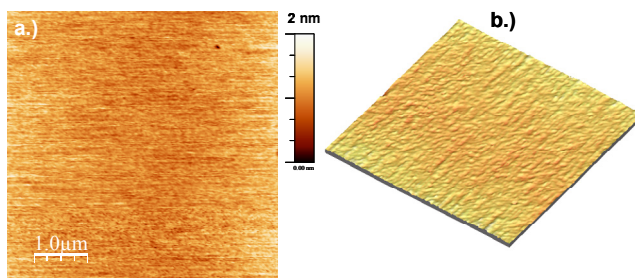
Figure 3-14: 2D (a.) and 3D (b.) AFM images of the surface of a thin film of BDiMIm.
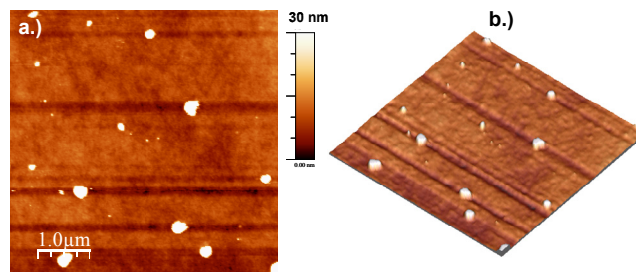
Figure 3-15: 2D (a.) and 3D (b.) AFM images of the surface of a thin film of PVP/BDiMIm.

The AFM images of PVP and BDiMIm indicate that the surface of these samples is relatively flat, whereas larger structures (higher than 30 nm) can be found on the surface of the PVP/BDiMIm sample.

3.3.5. Catalytic hydrogenation of ethene

To explore the accessibility of the Pt nanoparticles, the activity of Pt/PVPV/BDiMIm/SiO$_2$ for catalytic hydrogenation of ethylene reaction was tested. The apparent activation energy of 39 kJ/mol is approximately half of that reported for a series of Pt catalysts.[19] This indicates that Pt particles can be accessed by the reactants and that the reaction is not controlled by film diffusion limitations.

The activity of Pt/PVPV/BDiMIm/SiO$_2$ for catalytic hydrogenation of ethylene reaction is shown in Figure 3-16.
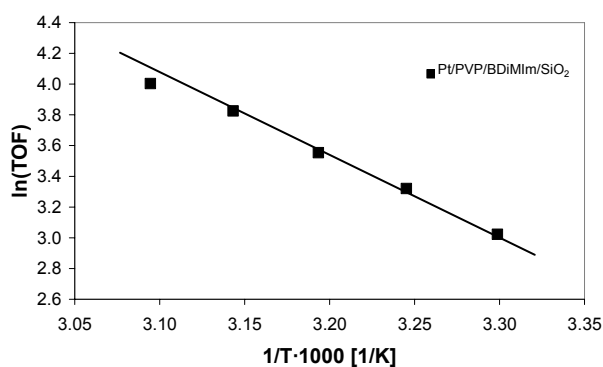
Figure 3-16: Catalytic activities for Pt/PVP/BDiMIm/SiO$_2$ in the hydrogenation of ethylene

3.4. Discussion

3.4.1.   *Properties of prepared nanoparticles*

According to Busser *et al.*[14] three elementary steps determine the size of PVP stabilized Pt nanoparticles prepared by reduction of Pt precursors with alcohol: (*i*) the mixing of the Pt salt and the polymer, (*ii*) the reduction of the salt to metal particles and (*iii*) the stabilization of the particles formed by the polymer. A good interaction of the polymer with the metal salt prior to the reduction step has been reported to be essential to obtain small particles.

Note that individual Pt atoms were not found in the polymer layer indicating in the present study that all Pt atoms are situated in nanoparticles, when using the preparation method by Busser *et al.*[14]. In contrast, dilution of the sample prepared by Teranishi *et al.*[15] led to a material, in which also Pt atoms were found in the polymer film. This demonstrates that the contact of the Pt ions with the polymer at higher temperatures without the presence of the reducing agent is needed to anchor the Pt cations.

In accordance with the previous reports the nanoparticles synthesized in this work had, according to TEM, a very narrow dispersion with a maximum at 2.2 nm. Assuming cuboctahedral geometry, this corresponds to average 210 atoms per Pt nanoparticle, of which 120 Pt atoms are on the surface.[20] As the molar ratio of Pt and PVP was 1/10 and a PVP chain consists of *ca.* 350 monomer units, each Pt nanoparticle is encapsulated in average by six PVP molecules.

Closer inspection of the TEM images showed that generally several nanoparticles were close to each other (see Figure 3-17). Single nanoparticles, as well as larger assemblies as observed for the undiluted samples, were the exception. With surprisingly high probability, the distance between particles varied between 1.1 to 2.0 nm. We would like to speculate at this point that the constancy of the distance is related to strong interactions between the covered Pt nanoparticles that are associated together by parts of the polymer chain.
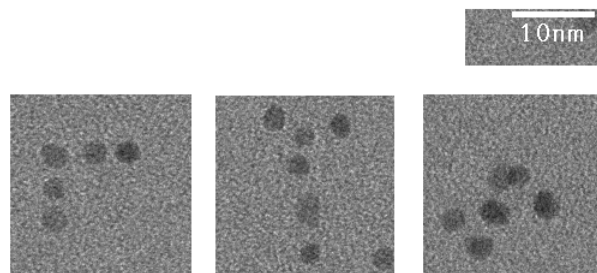
Figure 3-17: TEM images of PVP stabilized Pt nanoparticles, whereby the sample used for preparation of the TEM grids was highly diluted in methanol

The fact that that Pt/PVP dispersed in SiO$_2$ supported BDiMIm was active in the hydrogenation of ethylene shows, that the PVP protected nanoparticles are accessible for reactants and can thus catalyze the hydrogenation reaction.

3.4.2. Liquid and solid state NMR spectroscopy

The NMR spectra did not show changes in the chemical shift between the different samples. Note that a shift of the polymer carbonyl group was reported when Rh^{3+} ions interacted with PVP, indicating that the less sterically hindered carbonyl group is more important for the interactions to the metal salt than the nitrogen with strong electron-pair donor properties.[14] In the present case the coordination of the polymer to the Pt nanoparticles was so weak that the spectrum of the Pt containing sample was identical to the reference sample. As also the signals assigned to the ionic liquid did not vary with respect to the pure substances, we conclude that the interaction between the polymer molecules and the ionic liquid are very weak. The lack of strong interactions also indicates indirectly that Pt was quantitatively reduced in the preparation procedure.

The line broadening observed in the MAS NMR spectra of the supported catalysts is attributed to differences in the T2 relaxation time. These differences are not affected by magic angle spinning and, therefore, can be used to determine the mobility of specific atomic groups.[21-23] The line broadening indicates that the immobilization of the ionic liquid on silica led to a lower mobility of the cations of BDiMIm and to an increased viscosity. Especially the nitrogen bound methylene group was affected.

A further increase in line width was not observed, when also PVP was present in the supported film (PVP/BDiMIm/SiO$_2$) indicating that PVP did not interact strongly with the supported ionic liquid. When Pt/PVP (with 1 wt.% of Pt) were immobilized in the supported film of BDiMIm, the line width of the signals of the ionic liquid increased further indicating that the mobility of the molecules decreased. This indicates that the ionic liquid molecules are surrounding the Pt nanoparticles even in the presence of the polymer protection inducing so a substantial decrease in the mobility of the ionic liquid. The intensity of this interaction can be indirectly estimated. The presence of 1 wt.% of Pt supported directly on SiO$_2$ did not lead to an increase in the line width of the ionic liquid signals compared to a supported ionic liquid demonstrating that the mobility of Pt particles is needed for the self organization of the ionic liquid.[4] On the other hand, the increase in line width was not as distinct as for immobilized organometallic complexes.[11] Thus, we conclude that ionic liquid components are able to directly interact with the polymer protected particles, but that these interactions are moderated by the polymer.

3.4.3. Orientation of particles derived from analysis of NICISS

The angular dependence of the measured NICISS spectra contains detailed information of the film structure. As expected the profiles were flattened for low incident ion beam angles.

The concentration depth profiles calculated from the time of flight spectra indicate (see Figure 3-9) that the outer layer of the sample is structured in depth with the enrichment of carbon atoms, followed by fluorine, sulfur and platinum along the surface. Note that the signals for nitrogen and oxygen are not sufficiently resolved for interpretation. This sequence indicates that the ionic liquid is surface active, with the cation in the outer layer and the anion oriented with the CF$_3$ group pointing to the surface and the SO$_3$ group pointing to the bulk liquid. This finding is supported by the observation that the intensity of the fluorine signal is increased at lower incident angles, whereas the signals for sulfur and platinum are decreased. As pointed out above the path length through the film of IL

and PVP is longer for smaller angles and at the same time the atoms closer to the surface will be detected with higher probability.

The distance between the maxima of F and S is about 4.2 Å, whereas the distance in the triflate molecule amounts 2.8 Å. Thus, the distance between the observed maxima is larger than the F-S distance in a triflate molecule. To check, if this discrepancy is due to the sample or the analytical method, the amount of F was analyzed in circles of 3 Å around different locations of the S depth profile and *vice versa*. The ratio of F to S was always 3:1, showing that the data are in perfect agreement with stoichiometry.

So far no signals were assigned to PVP that functions as spacer between the ionic liquid and the platinum nanoparticles. This is firstly supported by the fact that only ionic liquid is found at the surface of the sample and the onset of the Pt signal is at a depth of 19 Å. Thus, Pt nanoparticles are not exposed at the surface. Secondly, if the triflate molecule would strictly coordinate to Pt, the distribution of F and S would have to follow that of Pt, which is not observed.

Figure 3-18 shows schematically and in an idealized way the alignment of the ionic liquid and polymer molecules around the Pt nanoparticles.
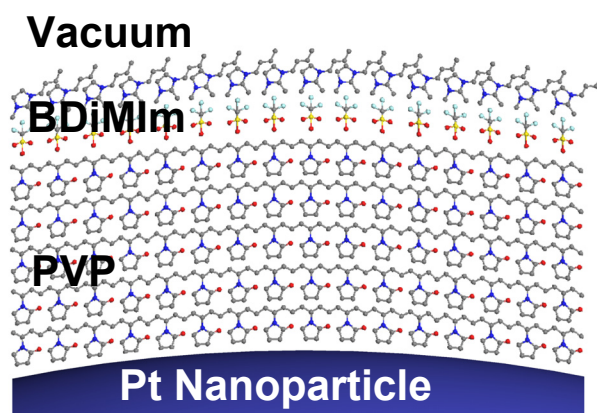
Figure 3-18:   Alignment of PVP, BDiMIm molecules and Pt nanoparticles along the surface (schematically).

Based on the assumptions made above, we can calculate the average thickness of the polymer layer around platinum to be 5 nm, corresponding to 5 monolayers of PVP in line with the onset of the Pt signal. It should be noted that after evaporation of methanol, a

highly concentrated solution is obtained. The volume ratio between Pt, PVP (density 1.2 g/cm^3) and the IL (density 1.38 g/cm^3) is roughly 0.026:1:2.391.

As we speculated that the dilution of the sample prior to application on graphite wafer and evaporation of the solvent might influence the local surface structure of the sample, 1:2 and 1:5 diluted samples were also measured. Indeed, diluting the sample prior to the NICISS experiments led to a decrease in the distance between the maxima for Pt and F, with the maximum of Pt moving closer to the surface of the sample. As the maximum in the fluorine signal increased relative to the maximum in the Pt signal as well as relative to the bulk signal, we conclude that a higher relative concentration of the IL is at the surface. This also indicates that the PVP layer got thinner presumably by dissolving and detaching parts of the polymer that is protecting the Pt nanoparticle. Note that these results are in line with the observation of assembles of Pt particles by TEM, as these detached polymer chains open the possibility to connect the Pt nanoparticles.

The data presented for the "undiluted" as well as for the "diluted" samples exclude the possibility that the surface is flat and laterally homogeneous, since the onset of the platinum signal shifts to larger depths, when the angle of the incident beam is decreased. Thus, we assume that the surface is composed of local structures that are described by droplet like ellipsoids. Figure 3-19 shows the cross section of the structure that has been fitted to the data. For this fit, ellipsoidal regions were allowed, where either only PVP or Pt and PVP were present. (Note that the measured data could not be fitted acceptably, when non ellipsoidal distributions of Pt and PVP were applied). For each incident angle He trajectories were distributed laterally over the model structure. For calculating the parameters, all spectra (i.e., all angles) were fitted simultaneously. The typical ellipsoid has a diameter of ca. 46 nm and an elevation of ca. 12 nm (blue line). The distribution of Pt is found within an ellipsoid as well (red line). The ellipsoid containing Pt indicates a region of increased Pt concentration, while Pt is not found outside of this ellipsoid. The region between the blue and the red line contains the polymer, whereby the boundary between polymer and Pt is very sharp. The ionic liquid forms a very thin layer on top of the polymer ellipsoid. Note that a single Pt nanoparticle has a diameter of 2 nm and, if encapsulated by PVP, of approximately 12 nm. This is much smaller than the structure size, which was observed.

This is in perfect agreement with the data obtained from the AFM measurements, where the surface of the Pt/PVP/BDiMIm sample contained elevations with a height of approximately 10 nm and a width of ca. 100 to 200 nm, whereas the PVP and BDiMIm samples were relatively flat. This clearly indicates that PVP encapsulated Pt aggregates are floating (the density of one Pt/PVP assembly with a polymer film thickness of 5 nm is 1.29 g·cm^{-1}, whereas the density of BDiMIm is 1.38 cm^{-1}) at the surface of the ionic liquid and are wetted by the ionic liquid, due its higher surface activity. The PVP/BDiMIm sample had higher (ca. 25 nm) and broader (up to 400 nm) elevations than the Pt/PVP/BDiMIm sample, suggesting that large aggregates of PVP are formed and are floating on the surface of the ionic liquid.
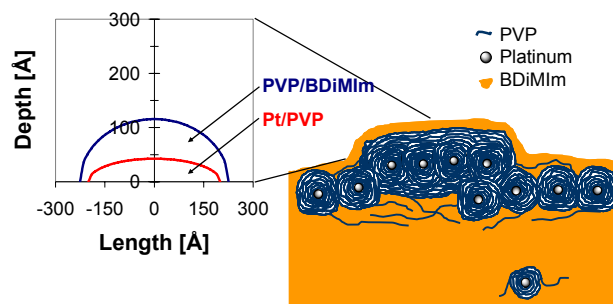
Figure 3-19: Cross section of the average surface structure derived by fitting the NICISS data for the undiluted sample and graphical representation.

In the diluted sample the surface is more structured (containing smaller elevations) than in the non-diluted sample. We speculate that a time critical process occurs during evaporation of the methanol, which is faster than the relaxation processes. After diluting the sample also Pt is found nearer to the surface of the sample. This shows that the detached polymer chains (*vide supra*) are partially in the bulk of the ionic liquid and mainly PVP around Pt clusters is at the top. Note that the apparent density (which is lower than the normal density) has to be considered for a coiled polymer in solution. Detached PVP with a chain length between 300 and 400 monomers is only moderately coiled in methanol[24] and thus, will be found in the bulk or at the bottom of the solution, whereas PVP coiled around Pt accumulate at the top.

3.4.4.   Influence of the preparation method on the results obtained by NICISS

The NICISS results for the Pt/PVP sample prepared according to a method by Teranishi *et al*.[15] indicated that after dilution of the sample in an eightfold amount of methanol the shape of the Pt profile and the angular dependence changed significantly (onset of the Pt signal hardly shifted with angle and no saturation of the signal). This was in contradiction to the expectation that after evaporation of the methanol, the same film structure as for the undiluted sample would be obtained, since the observation depth of our NICISS technique is up to 20 nm and, thus, by orders of magnitude smaller than the film thickness (0.48 μm for the 1:8 diluted sample). The interpretation of these results indicates that a significant amount of Pt is atomically dispersed in the polymer film (note that it is not possible to differentiate between Pt^0 and Pt^{2+} with NICISS), if the Pt salt does not have the possibility to age during preparation. It is interesting to note that the small atomically dispersed particles are only observed after dilution of the samples, as the film thickness of the polymer is reduced in that case and Pt is mainly to be found in the inner polymer layers.

3.5. Conclusions

The combination of physicochemical methods shows that the local surface chemistry of polymer protected Pt particles is complex, but can be well understood. The PVP shell (up to 5 nm in thickness) around the Pt nanoparticles remains intact under all circumstances. The ionic liquid partly penetrates the protective layer and interacts with the metal. This leads to a significant reduction of the mobility of the ionic liquid molecules as also observed with metal complexes. The protected particles form small islands of aggregated moieties that are connected by interacting polymer strands. Dilution of the sample in methanol leads to partial detachment or dissolution of polymer chains and enhances the island formation. These ensembles segregate at the surface protruding significantly out from the bulk ionic liquid. The ionic liquid covers these ensembles, the organic cation being on top and the SO_3 group of the anion underneath being oriented towards the bulk. This indicates that density differences between the protected Pt particles and the ionic

liquid must be a stronger driving force for the corrugation of the surface than classical chemical hydrophobic/hydrophilic interactions. If the latter forces were dominating an even dispersion of the protected particles in the ionic liquid would be the thermodynamically more favored situation.

A good interaction between the polymer and the metal salt prior to the reduction step is essential to assure that all Pt is within the nanoclusters and that Pt is not arbitrarily dispersed in the polymer layer. It is noteworthy to mention that the free mobility of the Pt particles markedly enhances the interaction with the ionic liquid in comparison to Pt particles supported on silica. The Pt nanoparticles dispersed in supported ionic liquids are furthermore accessible for reactants and able to catalyze hydrogenation reactions.

Acknowledgements

3.6. References

[1]   A. Riisager, R. Fehrmann, S. Flicker, R. van Hal, M. Haumann, P. Wasserscheid, *Angew. Chem., Int. Ed.* **2005**, *44*, 815.

[2]   O. Jimenez, T. E. Muller, C. Sievers, A. Spirkl, J. A. Lercher, *Chem. Commun.* **2006**, 2974.

[3]   C. Sievers, O. Jimenez, R. Knapp, X. Lin, T. E. Muller, A. Turler, B. Wierczinski, J. A. Lercher, *J. Mol. Catal. A: Chem.* **2008**, *279*, 187.

[4]   R. Knapp, A. Jentys, J. A. Lercher, *Green Chemistry* **2009**, *11*, 656.

[5]   C. P. Mehnert, E. J. Mozeleski, R. A. Cook, *Chem. Commun.* **2002**, 3010.

[6]   T. Welton, *Coord. Chem. Rev.* **2004**, *248*, 2459.

[7]   A. Wolfson, I. F. J. Vankelecom, P. A. Jacobs, *Tetrahedron Lett.* **2003**, *44*, 1195.

[8]   H. Hagiwara, Y. Sugawara, K. Isobe, T. Hoshi, T. Suzuki, *Org. Lett.* **2004**, *6*, 2325.

[9]   K. L. Fow, S. Jaenicke, T. E. Muller, C. Sievers, *J. Mol. Catal. A: Chem.* **2008**, *279*, 239.

[10]   R. Atkin, G. G. Warr, *J. Am. Chem. Soc.* **2005**, *127*, 11940.

[11]   C. Sievers, O. Jimenez, T. E. Muller, S. Steuernagel, J. A. Lercher, *J. Am. Chem. Soc.* **2006**, *128*, 13990.

[12]   J. P. Mikkola, J. Warna, P. Virtanen, T. Salmi, *Ind. Eng. Chem. Res.* **2007**, *46*, 3932.

[13]   J. Huang, T. Jiang, H. X. Gao, B. X. Han, Z. M. Liu, W. Z. Wu, Y. H. Chang, G. Y. Zhao, *Angew. Chem., Int. Ed.* **2004**, *43*, 1397.

[14]   G. W. Busser, J. G. van Ommen, J. A. Lercher, *J. Phys. Chem. B* **1999**, *103*, 1651.

[15]   T. Teranishi, M. Hosoe, M. Miyake, *Advanced Materials* **1997**, *9*, 65.

[16]   G. Andersson, H. Morgner, *Nuclear Instruments & Methods in Physics Research Section B-Beam Interactions with Materials and Atoms* **1999**, *155*, 357.

[17]   G. Andersson, H. Morgner, *Surf. Sci.* **1998**, *405*, 138.

[18]   G. Andersson, H. Morgner, H. Pohl, *Phys. Rev. A* **2008**, *78*.

[19]   S. D. Jackson, G. D. McLellan, G. Webb, L. Conyers, M. B. T. Keegan, S. Mather, S. Simpson, P. B. Wells, D. A. Whan, R. Whyman, *J. Catal.* **1996**, *162*, 10.

[20]   R. E. Benfield, *J. Chem. Soc., Faraday Trans.* **1992**, *88*, 1107.

[21]   A. Johansson, J. Tegenfeldt, *J. Chem. Phys.* **1996**, *104*, 5317.

[22]   A. Lauenstein, J. Tegenfeldt, *J. Phys. Chem. B* **1997**, *101*, 3311.

[23]   R. Spindler, D. F. Shriver, *J. Am. Chem. Soc.* **1988**, *110*, 3036.

[24]   E. Killmann, H. G. Wiegand, *Makromol. Chem.* **1970**, *132*, 239.

[25]   H. N. Cheng, T. E. Smith, D. M. Vitus, *J. Polym. Sci. Polym. Lett. Ed.* **1981**, *19*, 29.

Chapter 4.

INS and MAS NMR analysis of ionic liquid coated catalysts

Abstract

Supported ionic liquids were studied by inelastic neutron scattering (INS) and solid state nuclear magnetic resonance (NMR) spectroscopy to investigate on the influences of different support materials on the ionic liquid. Also the immobilization of metal nanoparticles, in thin films of supported ionic liquid, was studied as a novel concept to combine the high selectivity of homogeneous catalysts with the easy separation of a heterogeneous system. Focus was put on the interaction of the highly polar ionic liquid with the metal particles in order to understand the activity and selectivity of these catalysts.

4.1. Introduction

Immobilization of organometallic complexes and metal nanoparticles (see Figure 4-1) in thin films of supported ionic liquid has been suggested as a novel concept to combine the high selectivity of homogeneous catalysts with the easy separation of a heterogeneous system.[1] By using this concept complex catalysts can be assembled from well-characterized and well-defined building blocks. Supported Ionic liquids are an ideal medium for reactions with strong interactions of reactants and products. The use of ionic liquids also prevents oxidation of supported metal particles,[2] mediates interactions with reactants and products and also allows tuning the solubility of reactants.[3]
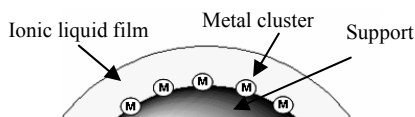
Figure 4-1   Catalyst concept with metal clusters immobilized in thin films of ionic liquid

The question arises, however, to what extent the highly polar ionic liquid influences the structure and properties of immobilized metal organic complexs and how the ionic liquid is influenced by the presence of metal nanoparticles. In order to understand these effects and their influence on the activity and selectivity of the catalysts, it is essential to study the nature of the interaction between the active component as well as the support with the ionic liquid. INS is the most appropriate technique to study these effects because (i) it is highly selective to hydrogen containing compounds, (ii) it offers a particularly good contrast to the bulk phase of the catalyst and (iii) it provides data that can be readily understood using modern *ab-initio* calculations.

The intensity of the bands in INS spectra depends on the total scattering cross-section, the momentum transfer and the amplitude of motion.[4] In the present case the incoherent cross-section of hydrogen is by far higher than all other occurring elements (see Table 4-1), so the recorded spectra will be dominated by modes associated with the cation of the used ionic liquid. The electronic properties, as e.g. the dipole moment or the

polarisability, do not influence the intensity, so all modes are allowed and no no symmetry-based selection rules have to be applied.[4]

In this chapter ionic liquids immobilized on different supports and on supported ionic liquids containing metal nanoparticles were in the focus. The materials were investigated by inelastic neutron scattering (INS) and solid sate nuclear magnetic resonance (NMR) spectroscopy to elucidate the influences of support and the active component of heterogeneous catalysts on the ionic liquid. The data obtained is interesting, since the samples used for this study are candidates for catalysts in the low temperature water-gas shift reaction. (See for example Chapter 5 of this work)

Table 4-1 Coherent, incoherent and absorption scattering cross sections in barn (1 barn = 10^{-28} m^2) for relevant elements present in study.[5, 6]

Element	Atomic number	σ_{coh}	σ_{inc}	σ_{abs}
H	1	1.7589	79.91	0.19
C	6	5.554	0.001	0.0
N	7	11.01	0.034	0.0
O	8	4.235	0.49	1.1
Al	13	1.495	0.009	0.13
S	16	1.019	0.007	0.3
Si	14	2.16	0	0.1

4.2. Experimental

4.2.1. Materials

The ionic liquid 1-butyl-2,3-dimethyl-imidazolium trifluoromethane sulphonate (BDiMIm) (99 %) with a maximum water and halide content of 47.8 and 103.1 ppm, respectively, was kindly provided by Solvent Innovation GmbH. Copper(II) nitrate trihydrate (>99 %) and methanol (99.8 %) were obtained from Aldrich. The alumina supports were kindly provided by Chemie AG. All chemicals were used as received. CO (purity 4.0), CO_2 (purity 4.5), Ar (purity 5.0), H_2 (purity 5.0) and N_2 (purity 5.0) were purchased from Westfalen.

2.1. Preparation of the supported catalysts

The alumina was dried at 200 °C for 24 hours before use. Catalysts with immobilized metal clusters were prepared by incipient wetness impregnation. Copper(II) nitrate trihydrate was dissolved in the appropriate amount of bi-distilled water; the solution was trickled onto the support and stirred until the water was completely absorbed. The water was removed by freeze drying. The precursors were calcined at 300 °C for three hours and at 450 °C for four hours in synthetic air and subsequently reduced at 250 °C for three hours in a flow of hydrogen.

For preparing the supported ionic liquid catalysts Cu/Al_2O_3 was added to a solution of BDiMIm dissolved in methanol. The suspension was stirred at room temperature for 10 min and the volatile components were slowly removed by freeze drying to give a free flowing black powder ($Cu/BDiMIm/Al_2O_3$).

Samples with different amounts of ionic liquid supported on alumina were prepared by adding Al_2O_3 into a solution of BDiMIm dissolved in methanol. After stirring for 10 min, the suspension was freeze dried to give a free flowing white powder ($BDiMIm/Al_2O_3$). To investigate on influences resulting from the preparation method the support was treated with diluted HNO_3 at the same pH as the samples that were impregnated with solutions of Copper(II) nitrate trihydrate. These precursors were also calcined and treated in hydrogen at the same conditions as the copper catalysts.

Furthermore three alumina supports with different acid/base properties (Al_2O_3-A pH = 4.42, Al_2O_3-N pH = 7.22 and Al_2O_3-B pH = 9.66) were used.

The BET surface areas, pore volumes and pore radii of the Al_2O_3 supports are listed in Table 4-2.

Table 4-2   BET surface areas, pore volumes and pore radii of alumina supports

Support	BET surface area [$m^2 \cdot g^{-1}$]	Pore volume [$mL \cdot g^{-1}$]	Pore diameter [nm]
Al_2O_3	214	0.60	8
Al_2O_3-calcined	210	0.51	8
Al_2O_3-HNO_3	208	0.50	8
Cu(5%)/Al_2O_3	174	0.64	7
BDiMIm(10%)/Al_2O_3	180	0.39	7
BDiMIm(20%)/Al_2O_3	124	0.31	7
BDiMIm(30%)/Al_2O_3	87	0.23	7
Al_2O_3-A	150	0.23	5
Al_2O_3-N	147	0.25	5
Al_2O_3-B	98	0.23	7

4.2.2.   Characterization

The copper content of the supported catalysts was determined by AAS using a UNICAM 939 spectrometer. The amount of ionic liquid adsorbed on the surface was determined by elemental analysis.

INS experiments were carried out at 15 K on the hot neutron 3-axis spectrometer IN1-BeF at Institut Laue-Langevin (ILL) in Grenoble, France using a Berylliumfilter-analyser (BeF) a Cu (220) monochromator. The instrument resolution was 4 cm^{-1} between 181 and 880 cm^{-1}, 8 cm^{-1} between 881 and 2020 cm^{-1}, 16 cm^{-1} between 2021 and 2745 cm^{-1} and 25 cm^{-1} at higher energy transfers. The spectra were recorded as a sum of at least two scans, with an error bar smaller the 200 neutron counts (smaller 1 %). The IN1-BeF spectrometer is optimized for studies of molecular dynamics, phonon density-of-states measurements and atomic bonding in hydrogen-containing matter, materials and compounds.[7]

The samples (each 20 to 25 g) were transferred to cylindric aluminium containers (see Figure 4-2 and Figure 4-3). The packed cylinders were checked for leaks, evacuated (< 0.001 Torr) for 120 minutes at 100 °C and flushed two times with helium. The cells were sealed at a pressure of 0.9 Torr helium. The sample containers were inserted in the cryostat, which was then cooled to -258 °C.
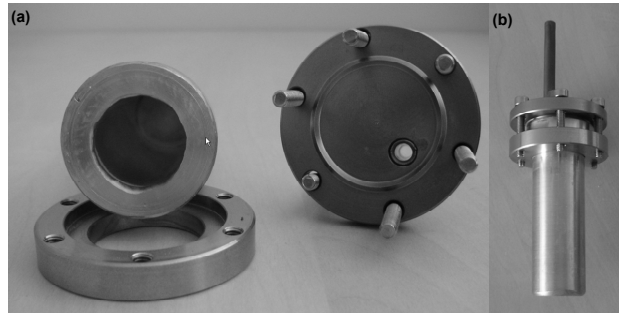
Figure 4-2 Photograph of an opened (a) and a closed (b) aluminum cylinder used for INS measurements.
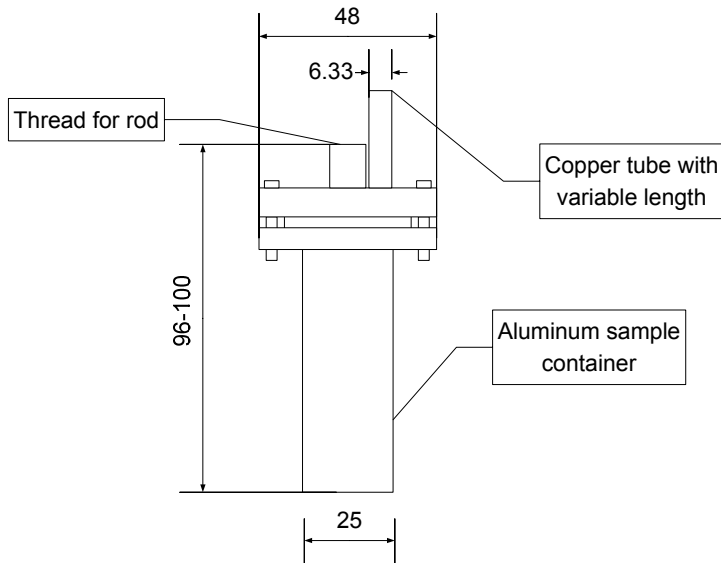
Figure 4-3 Schematic drawing of aluminum cylinder used for INS measurements.

A list of the measured samples is given in Table 4-3.

Table 4-3   Samples prepared for INS measurements.

Sample	Amount [g]	N_H / g_{sample}
BDiMIm	29.99	$3.41 \cdot 10^{22}$
BDiMIm(20%)/Al_2O_3-calcined	23.56	$5.65 \cdot 10^{21}$
BDiMIm(20%)/Al_2O_3-HNO_3	23.32	$5.65 \cdot 10^{21}$
Cu(5%)/BDiMIm(20%)/Al_2O_3	22.64	$5.75 \cdot 10^{21}$
BDiMIm(10%)/Al_2O_3	24.17	$3.07 \cdot 10^{21}$
BDiMIm(20%)/Al_2O_3	25.08	$5.64 \cdot 10^{21}$
BDiMIm(30%)/Al_2O_3	28.28	$7.82 \cdot 10^{21}$
BDiMIm(20%)/Al_2O_3-A	23.90	$5.64 \cdot 10^{21}$
BDiMIm(20%)/Al_2O_3-N	23.60	$5.65 \cdot 10^{21}$
BDiMIm(20%)/Al_2O_3-B	23.63	$5.64 \cdot 10^{21}$

The vibrational modes of hydrogen atoms of the ionic liquid were calculated with *GAUSSIAN03*.[8] The B3LYP hybrid functional and a 6-31G** basis set were applied. Vibrational modes were calculated for the optimized geometry. The resulting displacement vectors for each vibrational mode were used to derive the INS-spectra using *a-CLIMAX*.[9] The vibrational modes were visualized and assigned with Molview 3.0.

For solid state NMR, the samples were packed in 4 mm ZrO_2 rotors. ^{1}H MAS NMR measurements were performed on a Bruker AV500 spectrometer (B_0 = 14.1 T) with a spinning rate of 15 kHz. For temperature adjustment the bearing and drive gas stream were passed through a heat exchanger. The spectra were recorded as the sum of 100 scans using single pulse excitation with a pulse length of 2.6 μs and recycle time of 3 s.

4.3. Results

4.3.1.   Inelastic neutron scattering

Figure 4-4 shows the spectrum of pure BDiMIm. The assignment of the observed bands using the simulated spectra (Figure 4-5) is given in Table 4-4.
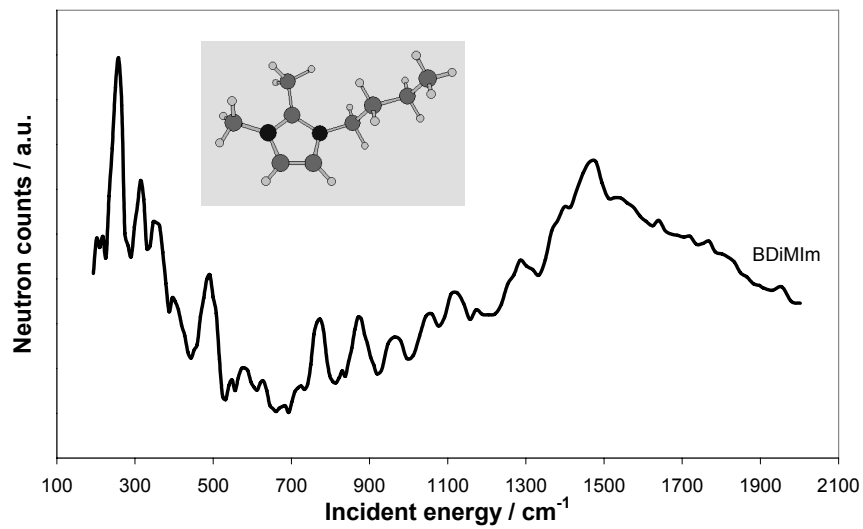
Figure 4-4   INS spectrum of parent BDiMIm.
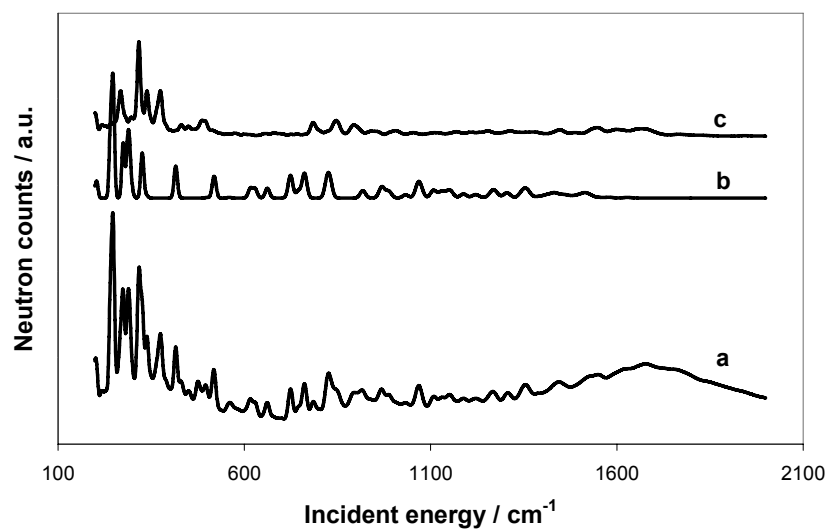
Figure 4-5   Calculated INS spectra of BDiMIm: total (a), first (b) and second overtone (c) spectrum.

Table 4-4   Assignment for observed (ν_{INS}) and calculated ($\nu_{sim.}$) INS bands of BDiMIm.

ν_{INS} [cm^{-1}]	Description	Type of vibration	$\nu_{sim.}$ [cm^{-1}]
201	Fundamental vibration	$CH_3(N)$- twist (s) CCCC deformation (w)	196
217	2. overtone	CCCC twist (m)	74 (222)
258	Fundamental vibration	Ring op deformation (s)	264
282	Fundamental vibration	Ring op deformation (s)	280
314	Fundamental vibration	$CH_3(C)$ ip deformation (s) $CH_3(N)$ ip deformation (m)	313
354	1. overtone	CH_3-twist (s) CCCC bond (m)	180 (360)
403	Fundamental vibration	CCCC valence (s)	400
491	Fundamental vibration	CCCC ip deformation (m) $CH_3(N)$ ip deformation (m) $CH_3(C)$ ip deformation (w)	498
548	Fundamental vibration	CCCC deformation (m)	537
580	Fundamental vibration	Ring op deformation (m) CCCC deformation (m) $(CH_3)C$ deformation (m)	590
628	Fundamental vibration	Ring op deformation (s)	635
685	Fundamental vibration	Ring HCCH op sym (s)	695
725	Fundamental vibration	CCCC deformation (w) Ring ip deformation (w)	730
773	Fundamental vibration	CCCC valence (s) Ring HCCH deformation (s)	789
830	Fundamental vibration	Ring HCCH ip asym (s)	825
878	Fundamental vibration	CCCC deformation (s)	881
963	Fundamental vibration	Ring ip deformation (s) $CH_3(C)$ deformation (m)	950
1059	Fundamental vibration	Ring HCCH sym deformation (s) $N(CH_3)$ deformation (s) Ring asym (w)	1039
1108	Fundamental vibration	$CH_3(N)$ twist (s)	1107
1172	Fundamental vibration	Ring ip deformation (s) CCCC deformation (w)	1172
1269	Fundamental vibration	CCCC deformation (s)	1253
1285	Fundamental vibration	CCCC deformation (s)	1292
1370	Fundamental vibration	$CH_3(C)$ deformation (s)	1370
1398	Fundamental vibration	CH_3 (N) sym (s) CH_3 (C) sym (m) Ring deformation (w)	1403
1462	Fundamental vibration	$CH_3(N)$ asym (s) CCCC deformation (m) $CH_3(C)$ asym (m)	1464

The amount of ionic liquid was varied to analyze to what extent the support has an influence on the ionic liquid (see Figure 4-6). When supporting 10 wt.% of ionic liquid on Al_2O_3 a shift of the band at 258 cm^{-1} to 246 cm^{-1} can be observed. Also the intensity of this band is increased upon immobilization. Furthermore the band at 403 cm^{-1} is shifted to higher energy (420 cm^{-1}). The band attributed to out of plane vibrations -CH groups of the imidazolium ring (at 725 cm^{-1}) is increased, relative to the surrounding peaks, for the supported ionic liquid. The intensity of all bands in the region from 400 to 1400 cm^{-1} is higher and when having a closer look at this region, the peaks from 830 to 1084 cm^{-1} (especially the peak at 963 cm^{-1}) are increased relative to the peak at 1108 cm^{-1}.

A higher loading of ionic liquid does not lead to any observable shifts of the bands of BDiMIm. Nevertheless changes in intensity can be observed, as the intensity of the bands in the region from 400 to 1400 cm^{-1} is decreased (becoming more similar to the parent ionic liquid) with a higher loading of ionic liquid. The decrease in intensity is more distinct when increasing the amount of ionic liquid from 10 to 20 wt.%. Relative to the other bands the bands at 1108 ($CH_3(N)$ twist vibrations) and 1370 cm^{-1} ($CH_3(C)$) deformation vibrations) have the highest intensity.
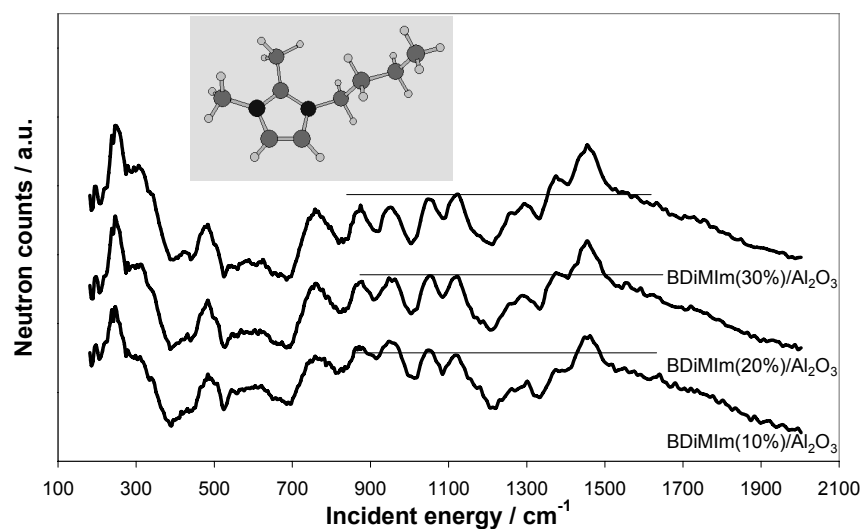
Figure 4-6   Influences of ionic liquid loading: INS spectra of BDiMIm(10%)/Al_2O_3, BDiMIm(20%)/Al_2O_3 and BDiMIm(30%)/Al_2O_3.

Figure 4-7 shows the influences of the support treatment on the ionic liquid. Besides an untreated support, two differently treated materials were examined and compared to Al_2O_3 impregnated with 5 wt.% Cu. Prior to the coating with ionic liquid, one support was treated in synthetic air and hydrogen at temperatures used for the calcination and reduction of the copper catalyst. The second support was impregnated with HNO_3 before the treatment in synthetic air and hydrogen.

Due to the different treatments of the supports only the bands in the region between 400 and 1200 cm^{-1} were affected. Calcining and treatment in hydrogen lead to an increase of the band at 420 cm^{-1} (vibration of the butyl chain) and a decrease of the bands between 700 and 1200 cm^{-1}. The smallest decrease was observed for the band located at 963 cm^{-1}. Treatment of the support with HNO_3 before impregnation with ionic liquid lead to further changes in the spectrum of BDiMIm, as the intensities of the bands at 491, 580 and 963 cm^{-1} decreased. Furthermore the bands at 773 and 1059 cm^{-1} were also less intense. Only minor changes (lower intensity of the bands located at 491 and 580 cm^{-1}) to the HNO_3 treated sample were observed when the ionic liquid was supported on Cu/Al_2O_3.
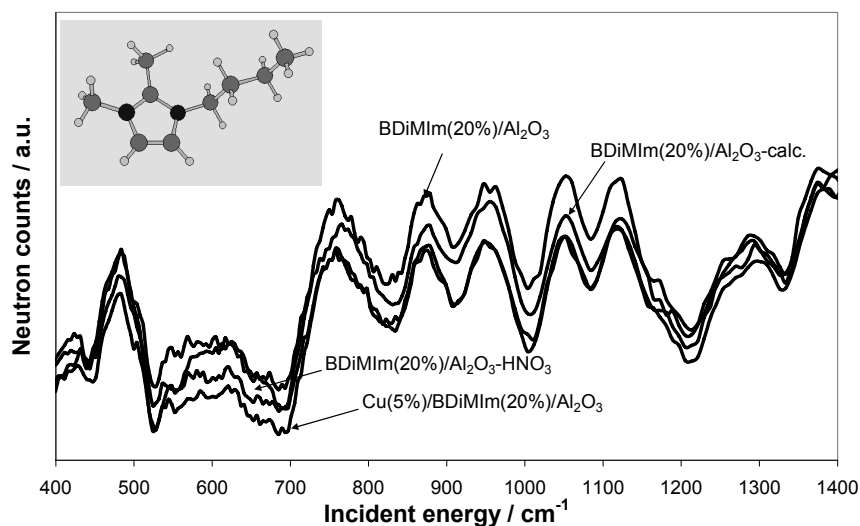
Figure 4-7   Influences due to support treatment: INS spectra of BDiMIm/Al_2O_3, BDiMIm supported on calcined Al_2O_3 and BDiMIm supported on calcined Al_2O_3 treated with HNO_3.

The influence of the acidity of the support in the ionic liquid is depicted in Figure 4-8. No differences between the spectra for neutral and the acidic support were observed.

When using the basic support some minor changes in the spectrum of the ionic liquid were observed (decrease of the bands located at 580, (773), 878, 963, 1052 and 1172 cm^{-1})
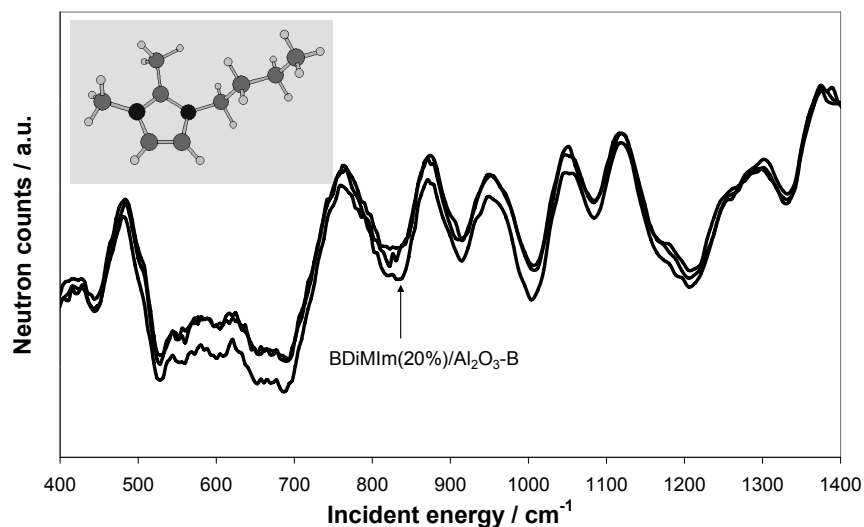
Figure 4-8 Influences of support acidity: INS spectra of BDiMIm/Al$_2$O$_3$-A, BDiMIm/Al$_2$O$_3$-N and BDiMIm/Al$_2$O$_3$-B.

4.3.2. *Solid state NMR spectroscopy*

When alumina was impregnated with 10 wt.% BDiMIm a noticeable line broadening in the ^{1}H MAS NMR spectra relative to the parent ionic liquid was observed (Figure 4-9) (for signal positions, assignments and line width, see Table 4-5. The highest increase in line width was found for the peaks assigned to the methylene group at the nitrogen atom (C5), while the least line broadening was observed for the terminal methyl and methylene groups of the alkyl chain. The line broadening is indicative of a reduced mobility of the imidazolium cation, when the ionic liquid was immobilized as thin film on Al$_2$O$_3$. When more ionic liquid was used for the impregnation of the materials (Figure 4-9), the line width of the NMR signals decreased. At a loading of 30 wt.% the line width of the signals attributed to the groups in the proximity of the imidazolium ring were increased by about 20 to 30 %, whereas the signals of the terminal groups of the butyl chain were not broadened compared to the parent ionic liquid.

When impregnating the alumina support with HNO_3 prior to the coating with ionic liquid, the line width increased by ca. 25 to 30 % compared to the immobilization the untreated support. A remarkable increase of the line width was observed when coating $Cu(5\%)/Al_2O_3$.

The inspection of the MAS NMR spectra of the ionic liquid immobilized on the supports with different acidity (Table 4-6) showed an increase in line width from $BDiMIm(20\%)/Al_2O_3$-B to $BDiMIm(20\%)/Al_2O_3$-A. Note that the line width was about two times higher compared to the other samples were 20 wt.% ionic liquid were used.
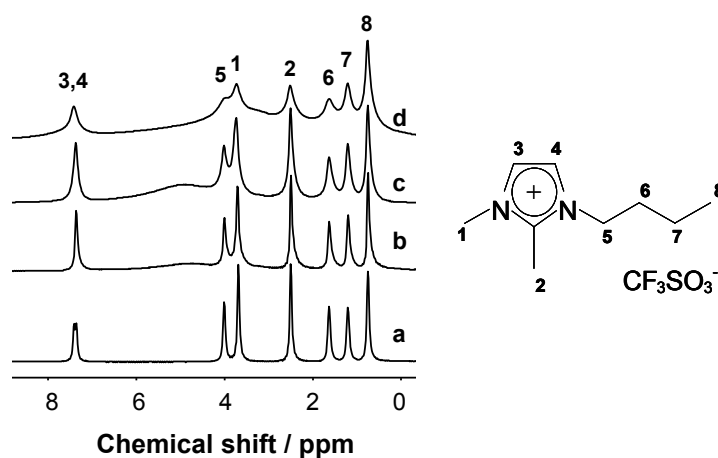
Figure 4-9   Solid state ^{1}H NMR spectra and signal assignments for pure BDiMIm (a), $BDiMIm(30\%)/Al_2O_3$ (b), $BDiMIm(20\%)/Al_2O_3$ (c) and $BDiMIm(10\%)/Al_2O_3$ (d).

Table 4-5   Signal position, width at half maximum and assignment for the ^{1}H MAS NMR spectra of BDiMIm, $BDiMIm(10\%)/Al_2O_3$, $BDiMIm(20\%)/Al_2O_3$, $BDiMIm(30\%)/Al_2O_3$ and $BDiMIm(20\%)/Al_2O_3$-HNO_3 (CS chemical shift / ppm; LW line-width / Hz)

	BDiMIm	$BDiMIm(10\%)/Al_2O_3$	$BDiMIm(20\%)/Al_2O_3$	$BDiMIm(30\%)/Al_2O_3$	$BDiMIm(20\%)/Al_2O_3$-HNO_3
Assignment	CS (LW)	CS (LW)	CS (LW)	CS (LW)	CS (LW)
3	7.46 (25)	7.43 (109)	7.39 (61)	7.37 (34)	7.39 (75)
4	7.41 (27)				
5	4.05 (30)	4.03 (175)	4.01 (73)	4.00 (38)	4.02 (92)
1	3.73 (27)	3.73 (151)	3.75 (66)	3.71 (39)	3.75 (81)
2	2.54 (27)	2.52 (93)	2.51 (52)	2.49 (29)	2.50 (63)
6	1.67 (33)	1.63 (105)	1.63 (77)	1.62 (45)	1.63 (90)
7	1.24 (35)	1.21 (91)	1.21 (60)	1.20 (38)	1.21 (73)
8	0.78 (30)	0.76 (69)	0.75 (51)	0.74 (30)	0.76 (60)

Table 4-6   Signal position, width at half maximum and assignment for the ^{1}H MAS NMR spectra of BDiMIm(20%)/Al$_2$O$_3$-A,BDiMIm(20%)/Al$_2$O$_3$-N, BDiMIm(20%)/Al$_2$O$_3$-B and Cu(5%)BDiMIm(20%)/Al$_2$O$_3$ (CS chemical shift / ppm; LW line-width / Hz)

Assignment	Cu(5%)BDiMIm(20%)/Al$_2$O$_3$ CS (LW)	BDiMIm(20%)/Al$_2$O$_3$-A CS (LW)	BDiMIm(20%)/Al$_2$O$_3$-N CS (LW)	BDiMIm(20%)/Al$_2$O$_3$-B CS (LW)
3 4	7.47 (414)	7.46 (272)	7.45 (250)	7.49 (234)
5	4.06 (424)	4.06 (291)	4.06 (273)	4.06 (254)
1	3.76 (391)	3.76 (259)	3.76 (205)	3.76 (203)
2	2.53 (327)	2.54 (254)	2.54 (245)	2.56 (216)
6	1.64 (258)	1.66 (236)	1.64 (227)	1.66 (225)
7	1.23 (269)	1.25 (242)	1.24 (237)	1.25 (220)
8	0.76 (252)	0.77 (245)	0.77 (234)	0.77 (234)

4.4. Discussion

The assignment of the bands observed for the parent ionic liquid was done by comparison of the vibrational modes of hydrogen with the recorded INS spectrum. The calculated data fits very well since only a maximal deviation of 2.5 % was observed.

The analysis of the INS spectra of the samples with a different loading of ionic liquid (Figure 4-6) showed that the bands assigned to the out of plane (258 cm^{-1}) and in plane (963 cm^{-1}) deformation vibrations of the imidazolium ring increased in intensity compared to the spectrum of the parent ionic liquid. This increase is attributed to stronger relative displacements of the hydrogen atoms (stronger vibrations) of the imidazolium ring. The coordination of the basic CF$_3$SO$_3^-$ anions to the surface hydroxyl allows for a stronger displacement of the C-H vibrations. The fact that the anion is coordinated to the surface is also supported by the shift of the band at 258 cm^{-1} to lower energy, indicating that less energy is needed to excite the vibrations of the imidazolium ring. At the same time the band located at 403 cm^{-1} (vibration of the butyl chain) is shifted to 420 cm^{-1}, indicating that the mobility of alky chain is reduced upon the immobilization of the ionic liquid. With increasing ionic liquid loading the intensities of the bands attributed to the vibrations of the CH$_3$(N) (1108 cm^{-1}) and CH$_3$(C) (1370 cm^{-1}) groups were increased indicating that the mobility of these groups was less restricted. The ^{1}H MAS-NMR spectra confirmed this, since the line width of the signals, that can be used to determine the mobility of certain atomic groups,[10-13] was reduced for the materials with a higher

ionic liquid loading. So for an increasing amount of IL the interactions between IL molecules more pronounced, i.e. the coordination via the imidazolium ring to the anion is more distinct (decreased flexibility of the ring) and the mobility of side chains is less restricted, e.g. by the pores or surface structures of the support.. Since the differences between the spectra are less articulated when going from 20 to 30 wt.%, 20 wt.% is the optimal amount of ionic liquid to study the interactions of the ionic liquid molecules with the support and with each other. At loadings higher than 20 wt.% mainly the interactions between the ionic liquid molecules would be observed. A loading of 10 wt.% would probably give more information about the interactions to the surface, but this would not only need more measurement time but would also not resemble the materials used for catalysis.[2]

The support was also treated at the conditions used during the preparation of the catalysts, to see whether the copper nanoparticles or the support have stronger interactions to the ionic liquid. In the INS spectra mainly the vibrations attributed to the alkyl rests were decreased upon calcinations of the support, indicating the flexibility of the side chains was reduced. The treatment of the support with HNO_3 before the calcination step only led to small changes in the INS spectra (further decrease in intensity of the same bands). This shows that a moderate structural change of the support occurred, restricting the mobility of the ionic liquid. Most probably defect sites were generated by the thermal treatment and the interactions of HNO_3 with the surface OH groups. The higher rigidity of the ionic liquid on the HNO_3 impregnated Al_2O_3-sample was also confirmed by the MAS NMR spectra since the line with of the signals increased when a treated support was used.

Adding copper to the materials leads to an observable decrease of the flexibility of the imidazolium ring and the butyl chain in the INS spectra. However, a marked increase in line width was found in the MAS NMR spectra indicating a dramatic increase of the viscosity of BDiMIm when copper was used. This shows that the copper nanoparticles strongly interact with the ionic liquid at room temperature. At lower temperatures where the INS spectra were recorded the interaction with the copper nanoparticles is by far not so pronounced, since the spectra are very similar to that of the HNO_3 treated sample. This shows that at lower temperatures the INS spectra are mainly influenced by the structure

of the support (note that the BET surface area and the pore volume of both samples are nearly identical, leading to only small changes in the spectra), whereas at higher temperatures also the interactions to the support and the immobilized particles play a major role for the alignment of the ionic.

When the acidity of the support was varied, no differences were observed between the neutral and the acidic support in the INS spectra, whereas, according to INS, the basic support constrains the in plane vibrations of the imidazolium ring. This also indicates that the ionic liquid is coordinating to the support via the anion. When using the basic support the interactions of triflate with the support are weakened, this in turn leading to stronger interactions between the anion and the cation. In the MAS NMR spectra a decrease in line width was observed when going from the acidic to the basic support. This indicates that the ionic liquid is interacting stronger with the support when an acidic support is used, leading to a closer packing of the IL molecules and thus to a reduced mobility. Again the differences between the two used methods can be seen. At low temperatures (INS) mainly the structure of the support has an influence on the ionic liquid, whereas at higher temperatures (MAS NMR) also the interactions between the support and the ionic liquid

4.5. Conclusions

INS and MAS NMR spectroscopy gave insight to the interactions of supported ionic liquids with different alumina supports and supported copper nanoparticles. INS can be used to determine the influences of the support structure on the ionic liquid whereas solid state NMR spectroscopy gives information about the electrostatic interactions of the support and metal nanoparticles with the ionic liquid. The ionic liquid was aligned with the anion coordinated to the surface of the support. In the INS investigations the acidity of the support and metal nanoparticles had only a minor influence on the supported ionic liquid. At room temperature, however, supported metal nanoparticles have a dramatic influence on the structure of the ionic liquid, as the viscosity is drastically reduced. At higher temperatures also the acidity of the support is influencing the alignment of

BDiMIm (higher acidity leads to a lower mobility of the IL, so the diffusion of reactants through the ionic liquid to the active site will be slowed down).

Acknowledgements

4.6. References

[1]   O. Jimenez, T. E. Muller, C. Sievers, A. Spirkl, J. A. Lercher, *Chem. Commun.* **2006**, 2974.

[2]   R. Knapp, A. Jentys, J. A. Lercher, *Green Chemistry* **2009**, *11*, 656.

[3]   C. Sievers, O. Jimenez, R. Knapp, X. Lin, T. E. Muller, A. Turler, B. Wierczinski, J. A. Lercher, *J. Mol. Catal. A: Chem.* **2008**, *279*, 187.

[4]   G. Auffermann, Y. Prots, R. Kniep, S. F. Parker, S. M. Bennington, *ChemPhysChem* **2002**, *3*, 815.

[5]   G. Ertl, in *Handbook of heterogeneous Catalysis*, 4 ed., VCH, Weinheim, **1997**, p. 1838.

[6]   *http://webster.ncnr.nist.gov/resources/n-lengths/*, **accessed Nov. 2009**.

[7]   *http://www.ill.eu/instruments-support/instruments-groups/instruments/in1/characteristics/*, **accessed in Nov. 2009**.

[8]   M. J. Frisch, G. W. Trucks, H. B. Schlegel, G. E. Scuseria, M. A. Robb, J. R. Cheeseman, J. Montgomery, J. A., T. Vreven, K. N. Kudin, J. C. Burant, J. M. Millam, S. S. Iyengar, J. Tomasi, V. Barone, B. Mennucci, M. Cossi, G. Scalmani, N. Rega, G. A. Petersson, H. Nakatsuji, M. E. Hada, M., K. Toyota, R. Fukuda, J. Hasegawa, M. Ishida, T. Nakajima, Y. Honda, O. Kitao, H. Nakai, M. Klene, X. Li, J. E. Knox, H. P. Hratchian, J. B. Cross, V. Bakken, C. Adamo, J. Jaramillo, R. Gomperts, R. E. Stratmann, O. Yazyev, A. J. Austin, R. Cammi, C. Pomelli, J. W. Ochterski, P. Y. Ayala, K. Morokuma, G. A. Voth, P. Salvador, J. J. Dannenberg, V.

G. Zakrzewski, S. Dapprich, A. D. Daniels, M. C. Strain, O. Farkas, D. K. Malick, A. D. Rabuck, K. Raghavachari, J. B. Foresman, J. V. Ortiz, Q. Cui, A. G. Baboul, S. Clifford, J. Cioslowski, B. B. Stefanov, G. Liu, A. Liashenko, P. Piskorz, I. Komaromi, R. L. Martin, D. J. Fox, T. Keith, M. A. Al-Laham, C. Y. Peng, A. Nanayakkara, M. Challacombe, P. M. W. Gill, B. Johnson, W. Chen, M. W. Wong, C. Gonzalez, J. A. Pople, Gaussian, Inc, Wallingford CT, **2004**.

[9] A. J. Ramirez-Cuesta, *Comput. Phys. Commun.* **2004**, *157*, 226.

[10] A. Johansson, J. Tegenfeldt, *J. Chem. Phys.* **1996**, *104*, 5317.

[11] A. Lauenstein, J. Tegenfeldt, *J. Phys. Chem. B* **1997**, *101*, 3311.

[12] C. Sievers, O. Jimenez, T. E. Muller, S. Steuernagel, J. A. Lercher, *J. Am. Chem. Soc.* **2006**, *128*, 13990.

[13] R. Spindler, D. F. Shriver, *J. Am. Chem. Soc.* **1988**, *110*, 3036.

Chapter 5.

Water-gas shift catalysts based on ionic liquid mediated supported Cu nanoparticles

Abstract

The effects of the presence of ionic liquids on the sorptive and catalytic properties of alumina supported Cu nanoparticles for low temperature water-gas shift has been explored using supported catalysts coated with a thin film of 1-butyl-2,3-dimethyl-imidazolium trifluoromethane sulphonate (BDiMIm). For parent uncoated catalysts the catalytic activity passed through a maximum with increasing concentration of oxygen on the Cu surface. With more reduced catalysts the presence of oxygen facilitates the dissociation of water, while excess concentrations of oxygen decreases the reaction rates due to limiting the concentrations of reactants. Catalysts coated with the ionic liquid showed higher water-gas shift activities at low temperatures compared to uncoated parent catalysts and the best commercial systems. This is attributed due to a higher concentration of water in the proximity of the active sites and due to facilitating the decomposition of carboxyl intermediates by the interaction with the ionic liquid. In addition, the presence of the ionic liquid reduces the sorption strength of CO lading to a better balance at the surface between the reactants.

5.1. Introduction

The water-gas shift reaction (Equation 1) allows adjusting the CO to H_2 ratio in synthesis gas. Since the reaction is exothermic, the formation of hydrogen is favored at low temperatures and, thus, the lower limit of the CO concentration decreases with decreasing temperature. The exit stream after the water-gas shift reaction step at approximately 200 °C, for example, contains less than 0.5 % CO.[1]

$$CO + H_2O \; \leftrightharpoons \; CO_2 \; + \; H_2 \qquad \Delta H^o = \text{-41 kJ/mol} \qquad \textbf{(1)}$$

In industrial implementations the water-gas shift reaction is performed in two steps, i.e., a high-temperature and a low-temperature reaction. The low-temperature water-gas shift reaction (LTWGS) is performed at temperatures between 210-250 °C over catalysts based on copper supported on zinc oxide. These catalysts are pyrophoric and deactivate in the presence of liquid water and by thermal sintering. Moreover, a clean feed is needed in order to avoid deactivation by sulfur and halides. Since the reaction is reversible, the rate of the CO conversion is reduced by the presence of the products CO_2 and H_2.[2]

Two different reaction mechanisms, the associative and the surface redox mechanism have been discussed for LTWGS.[3-10] Recent publications show that in the reaction pathway of the associative mechanism CO reacts with OH groups to a formyl (carboxyl) species (COOH). [5, 11] Under these conditions formate species can be also formed by CO_2 hydrogenation acting as stable spectator species. The elementary steps are compiled in equations (6) to (10).[5] Water and CO adsorb on the catalyst surface and the dissociation of the adsorbed water contains the first significant energy barrier. Its height depends on the Cu particle size and varies between 86 and 135 kJ·mol^{-1} being about seven times higher than the barrier to desorb molecular H_2O. [4, 5] Thus, the abstraction of hydrogen from water seems to be the rate controlling step from the energetic point of view.[5] The nature of the transition state and the energy barrier depend on the catalyst used and its surface properties. Adsorbed CO and OH react to COOH and the carboxyl species decompose to the products H_2 and CO_2 desorbing in the last step from the catalyst surface. The decomposition of COOH step is the second high energy barrier of the reaction. The

calculated potential energy diagram and the formed intermediate species are depicted in Figure 5-1.

$$H_2O_{(g)} + * \rightleftharpoons H_2O* \qquad \textbf{(6)}$$

$$H_2O* + * \rightleftharpoons OH* + H* \qquad \textbf{(7)}$$

$$CO_{(g)} + * \rightleftharpoons CO* \qquad \textbf{(8)}$$

$$OH* + CO* \rightleftharpoons COOH* + * \qquad \textbf{(9)}$$

$$2\ COOH* \rightleftharpoons CO_{2(g)} + H_2 + 2* \qquad \textbf{(10)}$$
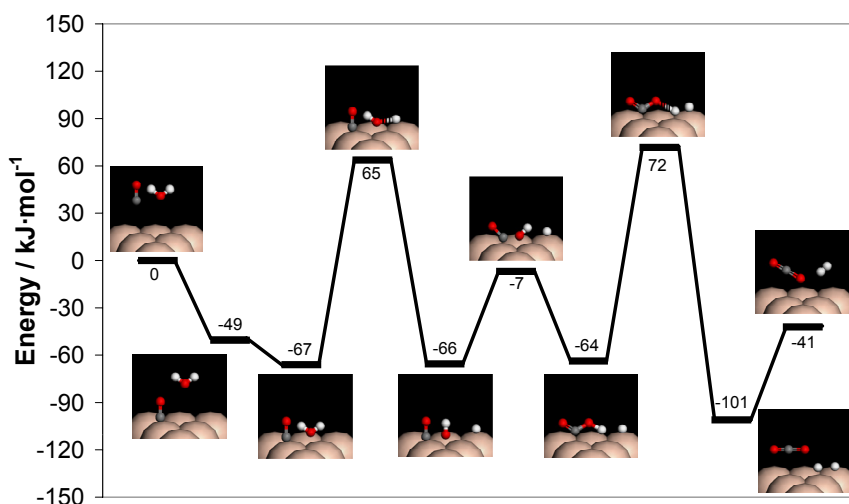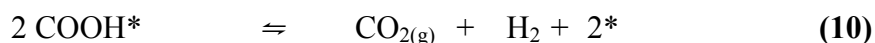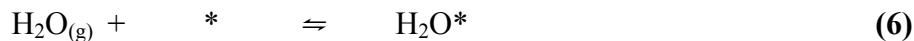
Figure 5-1: Calculated potential energy diagram for the water-gas shift reaction associative mechanism (over the carboxyl species).[5]

The second proposed reaction mechanism is the surface redox mechanism. Its elementary steps are shown in reactions (11) to (18).[7] The first step is the adsorption of water on the catalyst surface and its dissociation to oxygen and hydrogen, followed by a bond formation between oxygen and absorbed CO. The rate determining step depends on the partial pressure of the reactants.[8] Hydrogen and CO_2 adsorbed on Cu(100) surfaces can form formate species, which block the active sites of the catalyst. These formate species can undergo hydrogenation to methanol, but since their surface concentration is low under industrial conditions, the formation of methanol is not very important.[9]

$$H_2O_{(g)} \quad + \quad * \quad \rightleftharpoons \quad H_2O^* \tag{11}$$

$$H_2O^* \quad + \quad * \quad \rightleftharpoons \quad OH^* \quad + \quad H^* \tag{12}$$

$$2\,OH^* \quad \rightleftharpoons \quad H_2O^* \quad + \quad O^* \tag{13}$$

$$OH^* \quad + \quad * \quad \rightleftharpoons \quad O^* \quad + \quad H^* \tag{14}$$

$$2\,H^* \quad \rightleftharpoons \quad H_{2(g)} \quad + \quad 2^* \tag{15}$$

$$CO_{(g)} \quad + \quad * \quad \rightleftharpoons \quad CO^* \tag{16}$$

$$CO^* \quad + \quad O^* \quad \rightleftharpoons \quad CO_2^* \quad + \quad * \tag{17}$$

$$CO_2^* \quad \rightleftharpoons \quad CO_{2(g)} \quad + \quad * \tag{18}$$
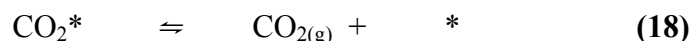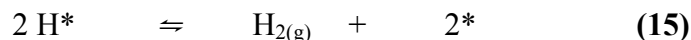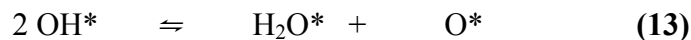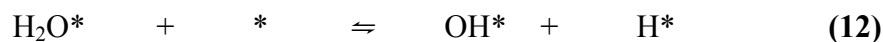
In contrast to the associative mechanism, the oxidation state of the catalytically active Cu-species changes during the reaction in the surface redox mechanism. The formation of hydrogen leads to oxidation of the catalyst surface, while the formation of CO_2 reduces the surface (schemes (19) and (20)).

$$H_2O_{(g)} \quad + \quad Red.^* \rightleftharpoons \quad H_{2(g)} \quad + \quad Ox.^* \tag{19}$$

$$CO_{(g)} \quad + \quad Ox.^* \rightleftharpoons \quad CO_{2(g)} \quad + \quad Red.^* \tag{20}$$

It is generally assumed that both reaction pathways may occur under low-temperature water-gas shift conditions over copper based catalysts and as the reaction is reported to be structure sensitive, the particle size should play a major role in the associative mechanism.[10]

Modifying the local concentration of reactants and products at the active sites, e.g., by using an environment with different solubilities of the gases, appears to be an option to enhance the activity of the catalysts. In the particular case, we intended to improve the availability of water in the water gas shift reaction by the presence of the ionic liquid. Supported ionic liquid catalysts,[12-15] are a special variant of supported liquid phase catalysts, [16] where the catalytically active components are immobilized in the ionic

liquid. Due to the low vapor pressure of the ionic liquid these catalysts can be readily applied in gas phase reactions.[17] The interactions of the ionic liquid with the support as well as with the active component have been studied showing ordering phenomena and domain formation of the ionic liquid.[15, 18, 19] Catalysts with immobilized ionic liquids were successfully used in reactions such as hydroformylation of olefins[12], achiral hydrogenation[20], Heck-reaction[21], hydroamination[13, 14] and hydrogenation[15].

This chapter focuses on the synthesis and characterization of catalysts based on ionic liquid (1-butyl-2,3-dimethyl-imidazolium trifluoromethane sulfonate) mediated Cu nanoparticles as catalysts for the low-temperature water-gas shift reaction. The correlation between the oxidation state of the metal and the reactivity in the low temperature water-gas shift reaction as well as the enhanced activity of the coated system at lower temperatures are addressed using *in situ* XAFS and IR spectroscopy in combination with investigating the activity for the low-temperature WGS reaction.

5.2. Experimental

5.2.1.   *Materials*

The ionic liquid 1-butyl-2,3-dimethyl-imidazolium trifluoromethane sulphonate (BDiMIm) (99 %) with a maximum water and halide content of 48 and 103 ppm, respectively, was provided by Solvent Innovation GmbH. Copper(II) nitrate trihydrate (> 99 %) and methanol (99.8 %) were obtained from Aldrich. The γ-alumina supports with pore volumes between 0.3 and 0.98 mL·g^{-1} and the ShiftMax-240 catalyst were provided by Süd Chemie AG. All chemicals were used as received. CO (purity 4.0), CO_2 (purity 4.5), Ar (purity 5.0), H_2 (purity 5.0) and N_2 (purity 5.0) were purchased from Westfalen.

2.1. Preparation of the supported catalysts

Before use, the series of alumina supports was dried at 200 °C for two hours. Cu was loaded onto the supports (5 wt. % metal) by incipient wetness impregnation using an aqueous solution of copper(II) nitrate trihydrate. After impregnation water was removed by freeze drying. The materials were calcined at 300 °C for three hours and at 450 °C for

four hours in synthetic air and subsequently reduced at 250 °C for three hours in hydrogen flow.

For preparing supported ionic liquid catalysts the corresponding Cu/Al_2O_3 catalysts were added to a solution of BDiMIm dissolved in methanol. The suspension was stirred at room temperature for 10 min and the volatile components were slowly removed by freeze drying to give a free flowing black powder ($Cu/BDiMIm/Al_2O_3$).

The BET surface areas, pore volumes and pore radii of the γ-Al_2O_3 supports are listed in Table 5-1.

Table 5-1   BET surface areas, pore volumes and pore radii of used support materials

Support	BET surface area $[m^2 \cdot g^{-1}]$	Pore volume $[mL \cdot g^{-1}]$	Pore radius [nm]
Al_2O_3-54	54	0.30	21.9
Al_2O_3-99	99	0.51	12.0
Al_2O_3-100	100	0.55	20.7
Al_2O_3-149	149	0.52	13.4
Al_2O_3-151	151	0.74	19.5
Al_2O_3-214	214	0.52	9.7
Al_2O_3-257	257	0.98	7/500 (bimodal)
Al_2O_3-360	360	0.30	3.5

5.2.2.   Characterization

The copper content of the supported catalysts was determined by atomic absorption spectroscopy using a UNICAM 939 spectrometer. The concentration of ionic liquid adsorbed on the surface was determined by elemental analysis.

IR spectra were measured on a Bruker IFS 88 spectrometer using a vacuum and a flow cell in transmission mode. The spectra were recorded at a resolution of 4 cm^{-1} in the region from 4000 to 400 cm^{-1}. The samples were pressed into self-supporting wafers and activated in vacuum for 1 h at 120 °C or in He flow at 120 °C for 1 h. The reduction was carried out at 215 °C and 0.8 bar hydrogen for 60 minutes for the vacuum experiments and in a hydrogen/helium mixture at 215 °C for 60 minutes for the experiments under flow conditions. CO, CO_2 and D_2O were dosed at pressures between 0.01 and 1.5 mbar.

For the reaction a gas mixture of 2.5 mL·min^{-1} CO and 2.5 mL·min^{-1} H$_2$O diluted in 20 mL·min^{-1} He was used.

The X-ray absorption spectra were collected at the beamline X1 at HASYLAB, DESY, Hamburg, Germany and at the beamline BM26A at the ESRF, Grenoble, France. The Si (111) double-crystal monochromator was detuned to 60% of the maximum intensity to minimize the intensity of the higher harmonics in the X-ray beam. The catalysts were pressed into self supporting wafers (ca. 150 mg) and the X-ray absorption spectra were collected at the Cu K edge (8979 eV) in He flow at liquid N$_2$ temperature for EXAFS analysis and at room temperature or under *in situ* conditions during activation (250 °C in a H$_2$/He mixture) and reaction (150 °C with a CO, He and water flow). The XAFS data were analyzed using the *Six Pack* software.[22] For EXAFS analysis, the scattering contributions of the background were removed from the X-ray absorption by a third-order polynomial function. The oscillations were weighted with k^2 and Fourier-transformed within the limit k = 3.5–12 Å^{-1}. The local environment of the Cu atoms was determined from the EXAFS using the phase-shift and amplitude function for Cu–Cu and Cu–O calculated including multiple scattering processes (FEFF version 8.40).[23, 24]

For the analysis of the XANES, the spectra were normalized to unity using the *XANES dactyloscope* software.[25] The position of the edge was calibrated using the spectra of a Cu reference-foil measured simultaneously.

5.2.3.   *Catalytic activity*

The low temperature water-gas shift reaction was studied at temperatures between 160 and 250 °C and a pressure of 2 bars. The gas-composition used was: 75 % H$_2$, 8 % CO, 13 % CO$_2$ and 4 % N$_2$, at a steam to gas ratio of 3 to 10. A fixed bed reactor filled with 200 mg catalyst (diluted with SiC) was used. The products were analyzed using a Shimadzu GC-2014 gas chromatograph.

For comparison also a commercial catalyst (ShiftMax-240) was also tested at temperatures between 160 and 250 °C.

5.3. Results

5.3.1.   *Activity of the uncoated catalysts*

The activities of the uncoated Cu/Al_2O_3 catalysts in the low temperature water-gas shift reaction as function of temperature are shown in Figure 5-2, the apparent energies of activation are given in Table 5-2.
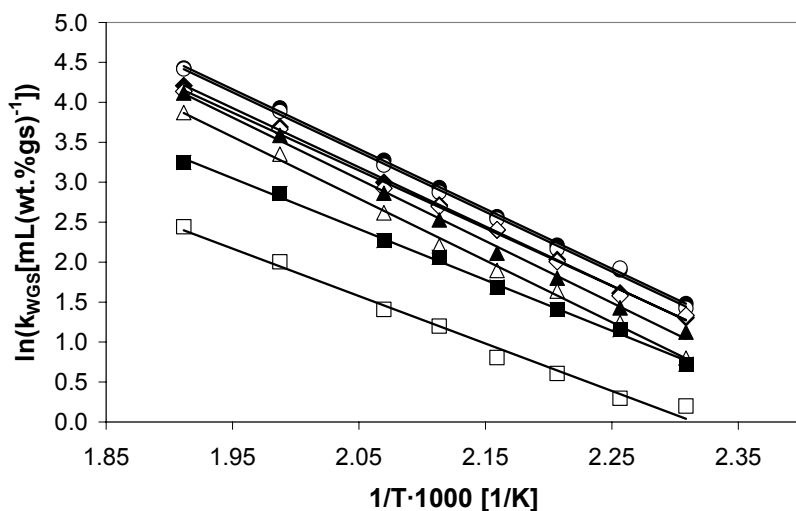
Figure 5-2   Activities of uncoated copper catalysts between 160 and 250 °C ($\triangle$ Cu/Al_2O_3-54, $\diamond$ Cu/Al_2O_3-99, $\blacklozenge$ Cu/Al_2O_3-100, $\bullet$ Cu/Al_2O_3-149, $\bigcirc$ Cu/Al_2O_3-151, $\blacktriangle$ Cu/Al_2O_3-214, $\blacksquare$ Cu/Al_2O_3-257 and $\square$ Cu/Al_2O_3-360)

Table 5-2:   Apparent energies of activation for the uncoated catalysts.

Catalyst	Apparent energy of activation [kJ·mol^{-1}]
Cu/Al_2O_3-54	64 ± 0.2
Cu/Al_2O_3-99	60 ± 0.2
Cu/Al_2O_3-100	62 ± 0.3
Cu/Al_2O_3-149	62 ± 0.1
Cu/Al_2O_3-151	62 ± 0.1
Cu/Al_2O_3-214	64 ± 0.2
Cu/Al_2O_3-257	53 ± 0.2
Cu/Al_2O_3-360	49 ± 0.6

With increasing surface area also the activity increased, reaching a maximum for the catalysts with an average surface area of 150 m^2·g^{-1} (Cu/Al_2O_3-149 and Cu/Al_2O_3-151).

Higher surface areas lead to lower CO conversions (lowest activities observed for Cu/Al$_2$O$_3$-360 with 360 m$^2 \cdot$g^{-1}). The apparent energies of activations were lower, when a support with a high surface area was used. A slight kinetic isotope effect was observed when D$_2$O was used instead of H$_2$O (see Figure 5-3) leading to an approximately 16 % lower rate of reaction.
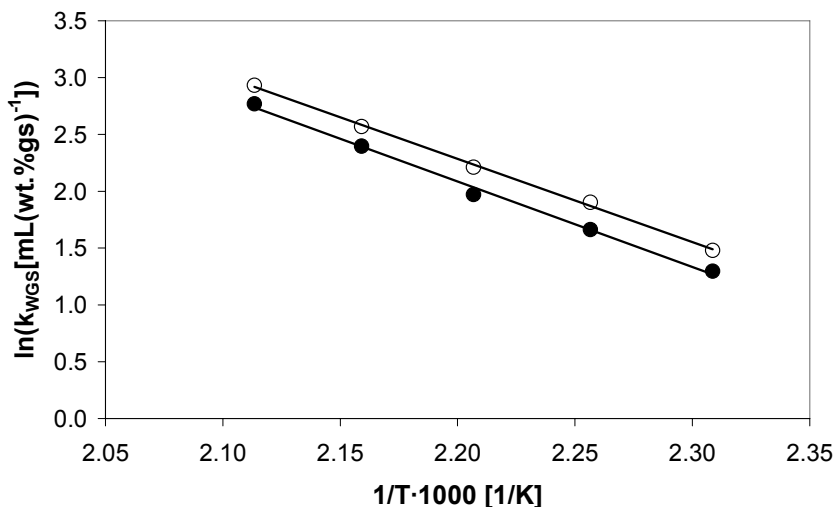
Figure 5-3   Activities of Cu/Al$_2$O$_3$-149 in the water-gas shift reaction with D$_2$O (●) and H$_2$O (○).

5.3.2.   *Structural and electronic properties of uncoated catalysts*

To determine the electronic structure of copper the uncoated catalysts were reduced *in situ* at 250 °C and examined by X-ray absorption spectroscopy (XAS) after reduction as shown in Figure 5-4. The fraction of oxidized Cu varies sympathetically with the specific surface area of the support. The degree of reduction of the Cu/Al$_2$O$_3$ catalysts was calculated from a linear combination of the XANES of Cu^0 and Cu^I references (Figure 5-5), and varied between 85 and 66 % (see Table 5-3).
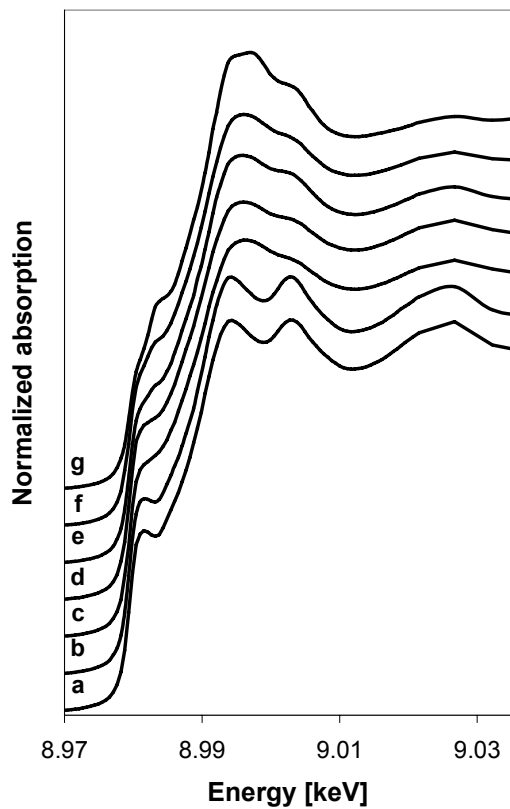
Figure 5-4 XANES of uncoated copper catalysts ((a) Cu/Al_2O_3-54, (b) Cu/Al_2O_3-99, (c) Cu/Al_2O_3-149, (d) Cu/Al_2O_3-151, (e) Cu/Al_2O_3-214, (f) Cu/Al_2O_3-257 and (g) Cu/Al_2O_3-360.) after reduction at 250 °C.
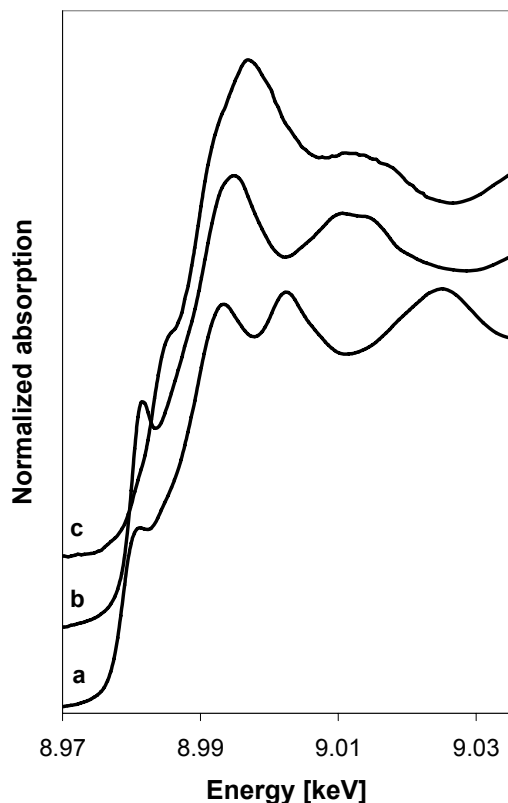
Figure 5-5   XANES of Cu^0 (a), Cu^I (b) and Cu^{II} (c) references (Cu^0 foil, Cu_2O and CuO).

The local environment of the Cu atoms with respect to the number of neighbors (coordination number N), the distance between them (r) and the statistical order (Debye-Waller factor σ^2) calculated from the EXAFS as well as the zero energy correction (E_0) are shown in Table 5-3. The particle size was determined from the average coordination number of the nearest metal neighbor atoms assuming a cuboctahedral geometry.[26] As indicated by XANES, the Cu-O concentration increases with increasing specific surface area.

A particle size of 1.1 nm for the Cu clusters, which can be related to a dispersion of 0.82, was determined for the catalysts with the highest activities in the low temperature WGS reaction (Cu/Al_2O_3-149 and Cu/Al_2O_3-151). In contrast, the catalysts with the lowest activities either consisted of larger Cu particles (2.1 nm) not indicating oxygen neighboring atoms (Cu/Al_2O_3-54) or of smaller copper clusters (0.7 nm) with a coordination number higher than 1 for oxygen neighbors (Cu/Al_2O_3-360).

Table 5-3   Results from XAS analysis for uncoated copper catalysts after reduction at 250 °C

	Al$_2$O$_3$-54	Al$_2$O$_3$-99	Al$_2$O$_3$-149	Al$_2$O$_3$-151	Al$_2$O$_3$-214	Al$_2$O$_3$-257	Al$_2$O$_3$-360
r$_{CuO}$ [Å]	---	---	1.84	1.88	1.89	1.87	1.91
N$_{Cu-O}$	0	0	0.6	0.6	0.8	1.0	1.2
σ^2	---	---	0.003	0.004	0.003	0.005	0.004
E$_0$ [eV]	---	---	1.7	6.2	7.7	5.3	6.6
r$_{CuCu}$ [Å]	2.53	2.53	2.53	2.53	2.53	2.53	2.53
N$_{Cu-Cu}$	9.4	9.2	7.1	7.0	6.0	5.8	5.5
σ^2	0.006	0.007	0.012	0.011	0.009	0.011	0.010
E$_0$ [eV]	4.5	4.4	2.8	3.4	2.6	1.5	3.6
Dispersion	0.56	0.59	0.81	0.82	0.89	0.90	0.92
Particle size	2.1 nm	2.0 nm	1.1 nm	1.1 nm	0.9 nm	0.8 nm	0.7 nm
Degree of reduction	95 %	91 %	83 %	84 %	76 %	72 %	66 %

5.3.3.   *Catalytic activity of ionic liquid coated copper catalysts*

A comparison of the water-gas shift activity between coated and uncoated catalysts is shown in Figure 5-6. Catalysts based on Al$_2$O$_3$-54, Al$_2$O$_3$-149 and Al$_2$O$_3$-257 were tested. With increasing temperature the activity of the coated catalysts decreased indicating an apparent negative energy of activation. We can exclude that this is an effect of deactivation as coated catalysts at 160 and 200 °C indicated that under all conditions the activity of the catalysts was higher at the lower reaction temperature.

At lower temperatures (below 180 °C), the coated copper catalysts showed higher conversions of CO than the uncoated catalysts.
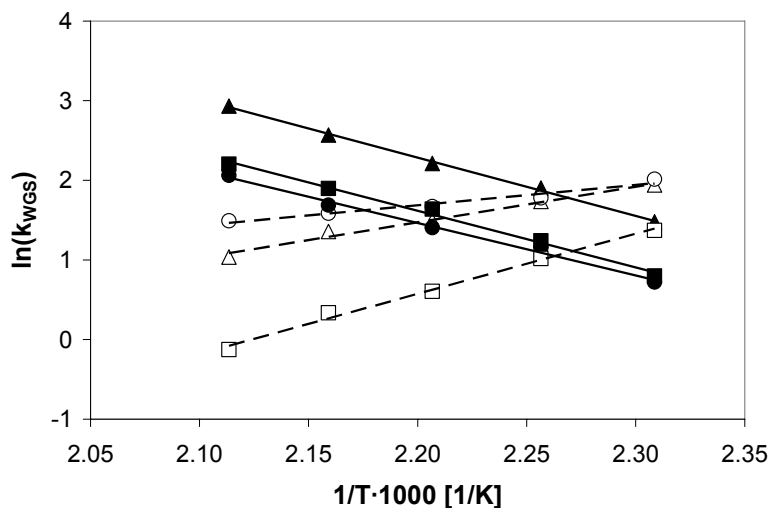
Figure 5-6 Water-gas shift activities for ionic liquid coated ($\square$ Cu/BDiMIm/Al$_2$O$_3$-54, $\triangle$ Cu/BDiMIm/Al$_2$O$_3$-149, $\bigcirc$ Cu/BDiMIm/Al$_2$O$_3$-257) and uncoated ($\bullet$ Cu/Al$_2$O$_3$-257, $\blacksquare$ Cu/Al$_2$O$_3$-54, $\blacktriangle$ Cu/Al$_2$O$_3$-149) copper catalysts

The deactivation over time of a coated catalyst at 160 °C and at 200 °C is shown in Figure 5-7.
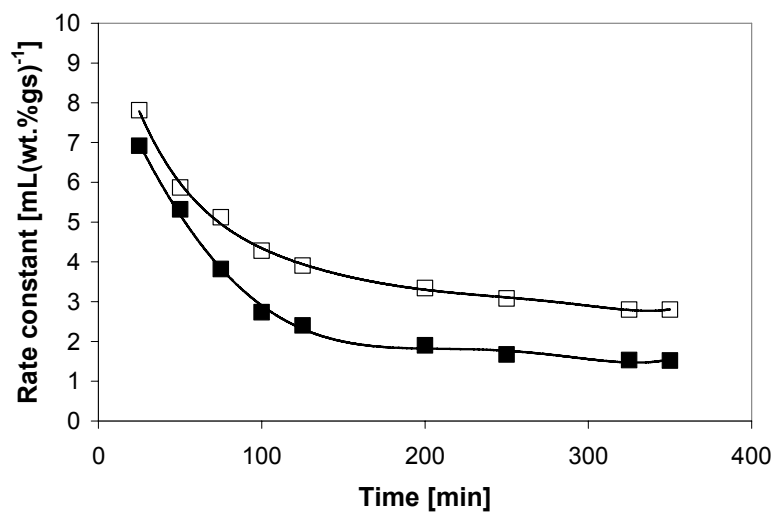
Figure 5-7: Deactivation over time of a coated catalyst at 160 °C ($\square$) and at 200 °C ($\blacksquare$).

A comparison of the coated catalyst with the highest activity in the water-gas shift reaction (Cu/BDiMIm/Al$_2$O$_3$-257) and a commercial catalyst (ShiftMax-240) is given in

Figure 5-8. It is interesting to note that the coated catalyst was 5 times more active at 160 °C, although the metal loading of the commercial catalyst was ten times higher.
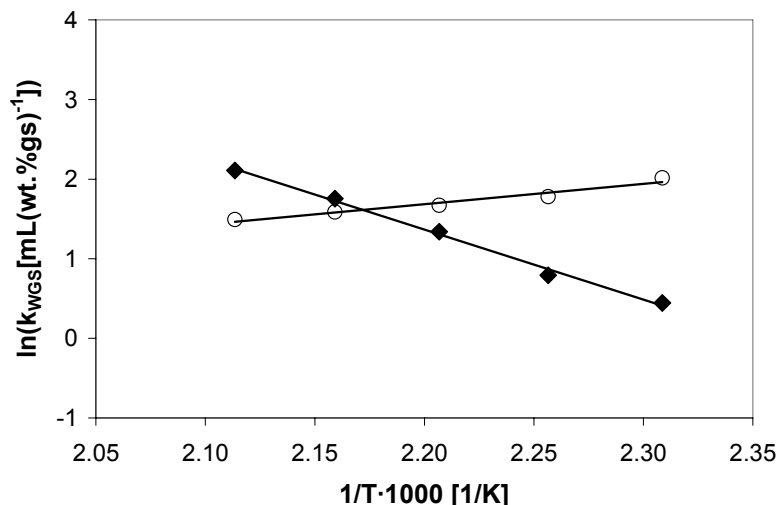
Figure 5-8   Comparison of activity for an ionic liquid coated copper catalyst (○ Cu/BDiMIm/Al$_2$O$_3$-257) and a commercial catalyst (◆)

5.3.4.   *Characterization of the electronic and structural properties of the ionic liquid coated catalysts under reaction conditions*

The XANES collected during the reduction of an uncoated catalyst as well as of four BDiMIm coated (5, 10, 20 and 30 wt.%) copper catalysts in H$_2$ flow at 210 °C are complied in Figure 5-9. In general, a higher amount of ionic liquid present on the catalysts led to a higher degree of reduction of the Cu clusters, whereas for the uncoated catalyst XANES indicates partial oxidation of the Cu particles. Using a linear combination of the XANES of Cu^0 and Cu^I references for the quantitative analysis of the XANES structure, the average concentration of Cu^0 was determined to increase for example from 40 % for the uncoated catalyst to 66 % for the catalyst coated with 30 wt. % BDiMIm.
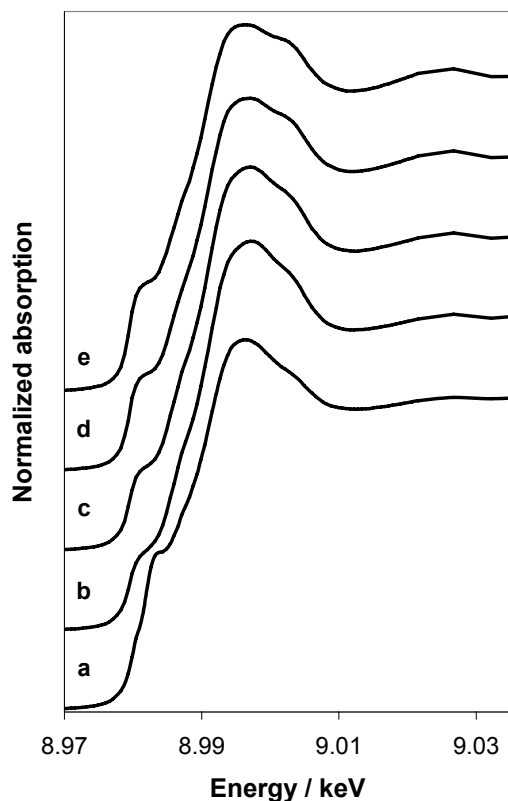
Figure 5-9   XANES of Cu/Al$_2$O$_3$-214 (a) and of Cu/Al$_2$O$_3$-214 coated with coated with 5 (b), 10 (c), 20 (d) and 30 wt.% (e) BDiMIm after reduction at 210 °C in H$_2$ for … h.

The catalysts used for the comparison of coated and uncoated systems (based on Al$_2$O$_3$-54, Al$_2$O$_3$-149 and Al$_2$O$_3$-257) were also examined by *in situ* XAS experiments. After the reduction of the catalyst at 215 °C, XAS was measured at liquid nitrogen temperature for the EXAFS analysis. Then, the sample was heated to 150 °C under He flow. Figure 5-10 shows the spectra of Cu/Al$_2$O$_3$-149 in He at 150 °C, after dosing CO at 150 °C for 30 minutes, after 60 minutes under reaction conditions (CO to H$_2$O ratio 1:2) and again in He after the reaction at 30 °C. When CO is added to the system the oxidation state is lowered and a further reduction takes place, when the sample is additionally exposed to water by the hydrogen generated. The structure of the copper nanoparticles after the reaction was determined by EXAFS analysis.

The oxidation state of the coated catalysts after the reduction step is lower than for the uncoated systems. In presence of the reactants the coated catalysts were also reduced,

but the differences in the XAS compared to XAS in the absence of reactants are not as distinct as for the uncoated catalysts.
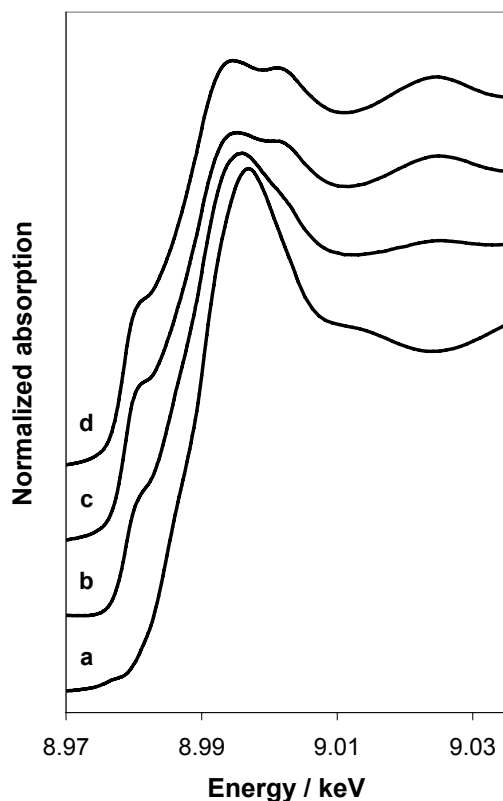
Figure 5-10   XANES spectra of Cu/Al$_2$O$_3$-149 after reduction (a), in CO flow (b), under reaction conditions (c) and after reaction (d) (Note that the catalysts were reduced at 215 °C before reaction and not at 250 °C as the catalysts shown in Figure 5-4)

The XANES for the uncoated and coated catalysts after the reaction are compared in Figure 5-11 and Figure 5-12, respectively. With Cu/Al$_2$O$_3$-149 the degree of reduction is higher compared to the other two tested uncoated supports. The XANES of the coated catalysts show the same oxidation state after treatment at reaction conditions and indicate an oxidation state closer to 0 (95 % compared to 87 %) than the uncoated catalysts.
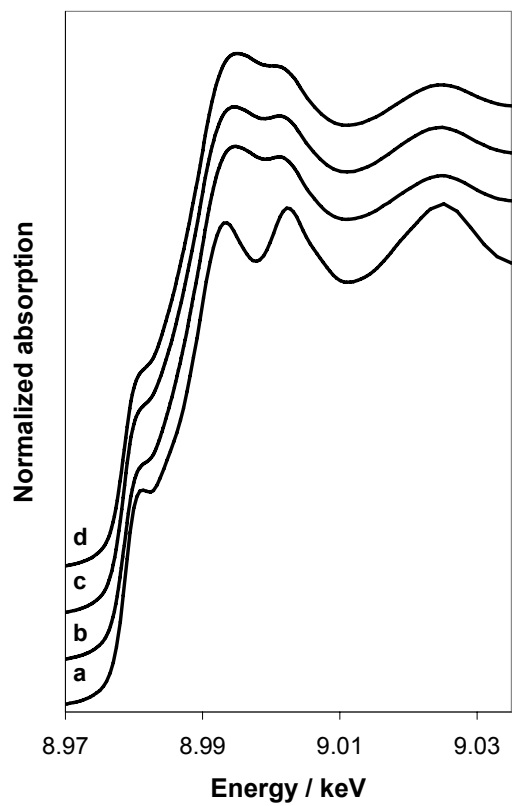
Figure 5-11   XANES spectra of Cu(0) reference foil (a), Cu/Al$_2$O$_3$-54 (b), Cu/Al$_2$O$_3$-149 (c) and Cu/Al$_2$O$_3$-257 (d) after *in situ* reaction at 150 °C
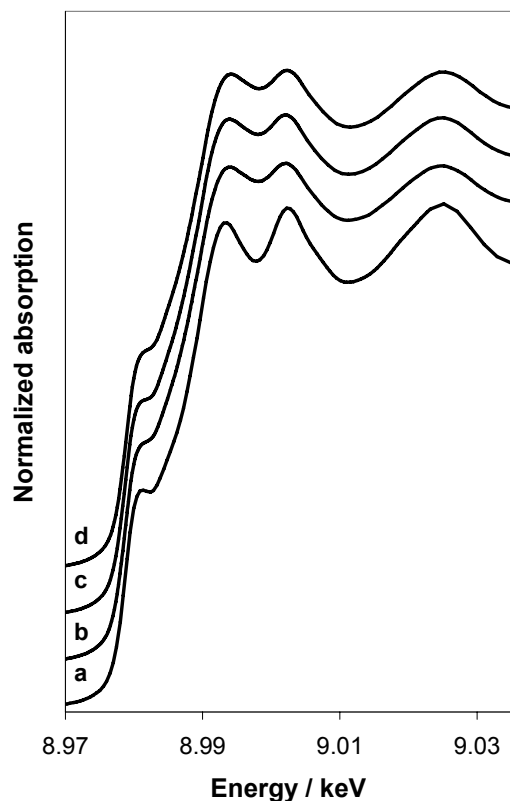
Figure 5-12 XANES spectra of Cu(0) reference foil (a), Cu/BDiMIm/Al$_2$O$_3$-54 (b), Cu/BDiMIm/Al$_2$O$_3$-149 (c) and Cu/BDiMIm/Al$_2$O$_3$-257 (d) after *in situ* reaction at 150 °C

The results of the EXAFS analysis before and after the treatment under reaction conditions are compiled in Table 5-4 (uncoated systems) and Table 5-5 (coated systems) (note that the catalysts were reduced at 215 °C before reaction and not at 250 °C as the catalysts shown in Table 5-3, leading to lower states of reduction).

For the uncoated catalysts the number of copper-oxygen neighbors is (almost) identical before and after and the treatment at reaction conditions, while the number of copper-copper neighbors increases indicating a sintering of the metal particles.

Table 5-4   Results of EXAFS analysis for uncoated copper catalysts before and after reaction at 150 °C

	Cu/Al$_2$O$_3$-54		Cu/Al$_2$O$_3$-149		Cu/Al$_2$O$_3$-257	
	before	after	before	after	before	after
r$_{CuO}$ [Å]	1.97	1.97	1.91	1.92	1.91	1.95
N$_{Cu-O}$	0.8	0.6	1.0	0.6	1.1	0.6
σ^2	0.003	0.003	0.005	0.005	0.005	0.004
E$_0$ [eV]	21.4	13.8	8.6	8.8	9.8	12.1
r$_{CuCu}$ [Å]	2.53	2.54	2.53	2.54	2.53	2.54
N$_{Cu-Cu}$	6.2	7.8	5.2	8.1	4.6	7.7
σ^2	0.008	0.006	0.009	0.007	0.010	0.007
E$_0$ [eV]	3.5	4.2	1.9	3.9	2.8	3.8
Dispersion	0.88	0.77	0.93	0.73	0.94	0.74
Particle diameter	0.9 nm	1.3 nm	0.7 nm	1.4 nm	0.6 nm	1.2 nm

For the coated catalysts copper-oxygen neighbors were not found after treatment at water-gas shift reaction conditions. The largest particles (d = 2.7 nm) after reaction can be found for the catalyst based on Al$_2$O$_3$-149. Note that the copper particle size was bigger compared to the uncoated systems.

Table 5-5   Results of EXAFS analysis for coated copper catalysts before and after reaction at 150 °C

	Cu/BDiMIm/Al$_2$O$_3$-54		Cu/BDiMIm/Al$_2$O$_3$-149		Cu/BDiMIm/Al$_2$O$_3$-257	
	before	after	before	after	before	after
r$_{CuO}$ [Å]	1.94	---	1.99	---	1.93	---
N$_{Cu-O}$	0.5	---	0.3	---	0.6	---
σ^2	0.006	---	0.001	---	0.006	---
E$_0$ [eV]	9.3	---	17.5	---	6.4	---
r$_{CuCu}$ [Å]	2.54	2.54	2.54	2.54	2.54	2.54
N$_{Cu-Cu}$	9.0	9.7	9.4	10.0	9.0	9.7
σ^2	0.006	0.006	0.006	0.006	0.006	0.006
E$_0$ [eV]	4.8	4.6	5.2	4.6	4.9	4.1
Dispersion	0.63	0.51	0.54	0.46	0.63	0.51
Particle diameter	**1.8 nm**	2.4 nm	**2.2 nm**	2.7 nm	**1.8 nm**	2.4 nm

3.5 Adsorption of CO, CO$_2$ and D$_2$O followed by IR spectroscopy

Adsorption of CO, CO$_2$ and D$_2$O was followed by IR spectroscopy in order to understand the interactions of the reactants with the active sites. Note that D$_2$O was used

instead of H_2O to avoid absorption bands in the region of the perturbed OH vibrations resulting from the hydrogen bonding interaction between the OH groups of the support and ionic liquid.[15]

The IR spectra of CO adsorbed on Cu/Al_2O_3 (a) and CO adsorbed on $Cu/BDiMIm/Al_2O_3$ (b) are shown in Figure 5-13. For the uncoated catalyst the adsorption of CO led to a band at 2088 cm^{-1} assigned to CO linearly adsorbed on Cu^0. For the coated catalyst this band was smaller and shifted to 2117 cm^{-1}. In both cases, adsorbed CO was not observed after evacuation.
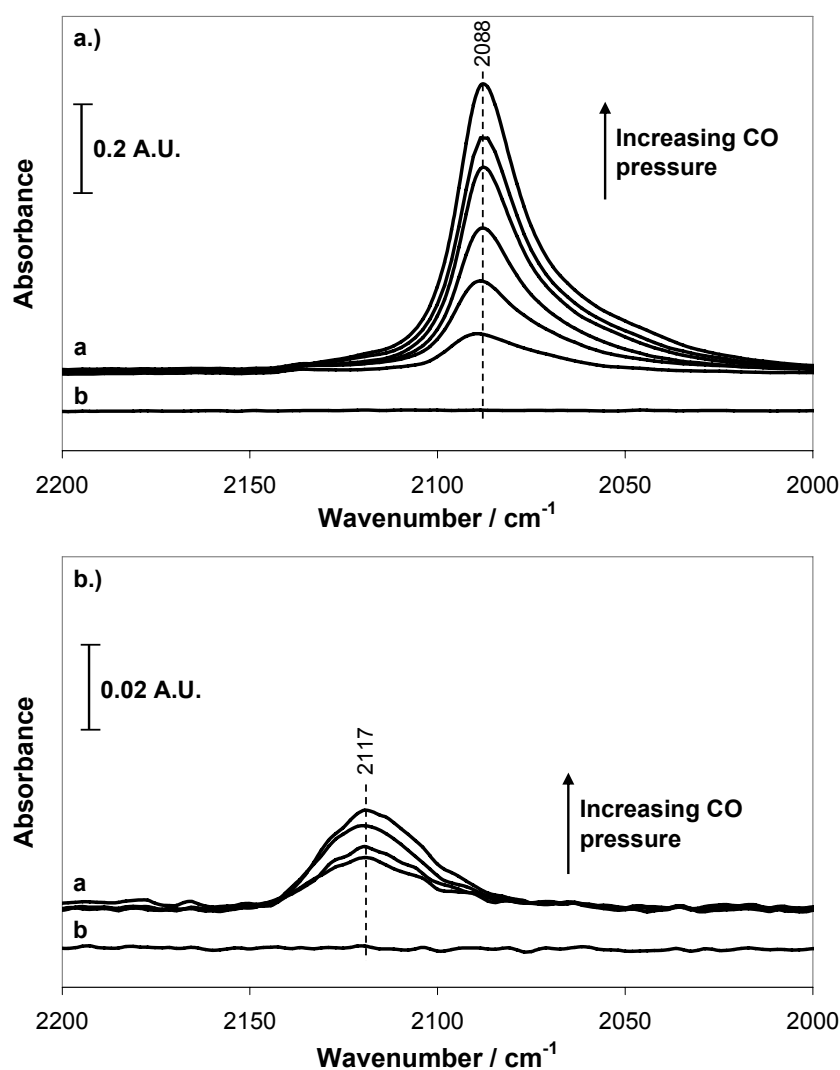
Figure 5-13   IR absorption spectra of CO adsorbed on copper supported on alumina (a) and CO adsorbed on $Cu/BDiMIm/Al_2O_3$ (b) (spectrum b after evacuation)

The adsorption of CO_2 on Cu/Al_2O_3 (shown in Figure 5-14) led to bands at 1657 cm^{-1}, 1228 cm^{-1} (bridged bidentate carbonate), 1429 cm^{-1} (ionic carbonate) and 1600 cm^{-1}, 1391 cm^{-1} (carboxyl). Bands characteristic for the formation of bridged bidentate carbonate (1637 cm^{-1}), carboxyl (1570 cm^{-1}) and an ionic carbonate species (1442 cm^{-1}) were only observed on $Cu/BDiMIm/Al_2O_3$. The region below 1400 cm^1 was dominated by changes of the absorption bands of the trifluoromethanesulfonate anion of the ionic liquid (vide infra). The concentration of CO_2 remaining on the sample after evacuation was higher for the coated catalyst. It should be noted that CO_2 was also adsorbed on the parent support. The observed bands were attributed to bridged bidentate carbonate species (1650 and 1228 cm^{-1}) and an ionic carbonate species at 1435 cm^{-1}.
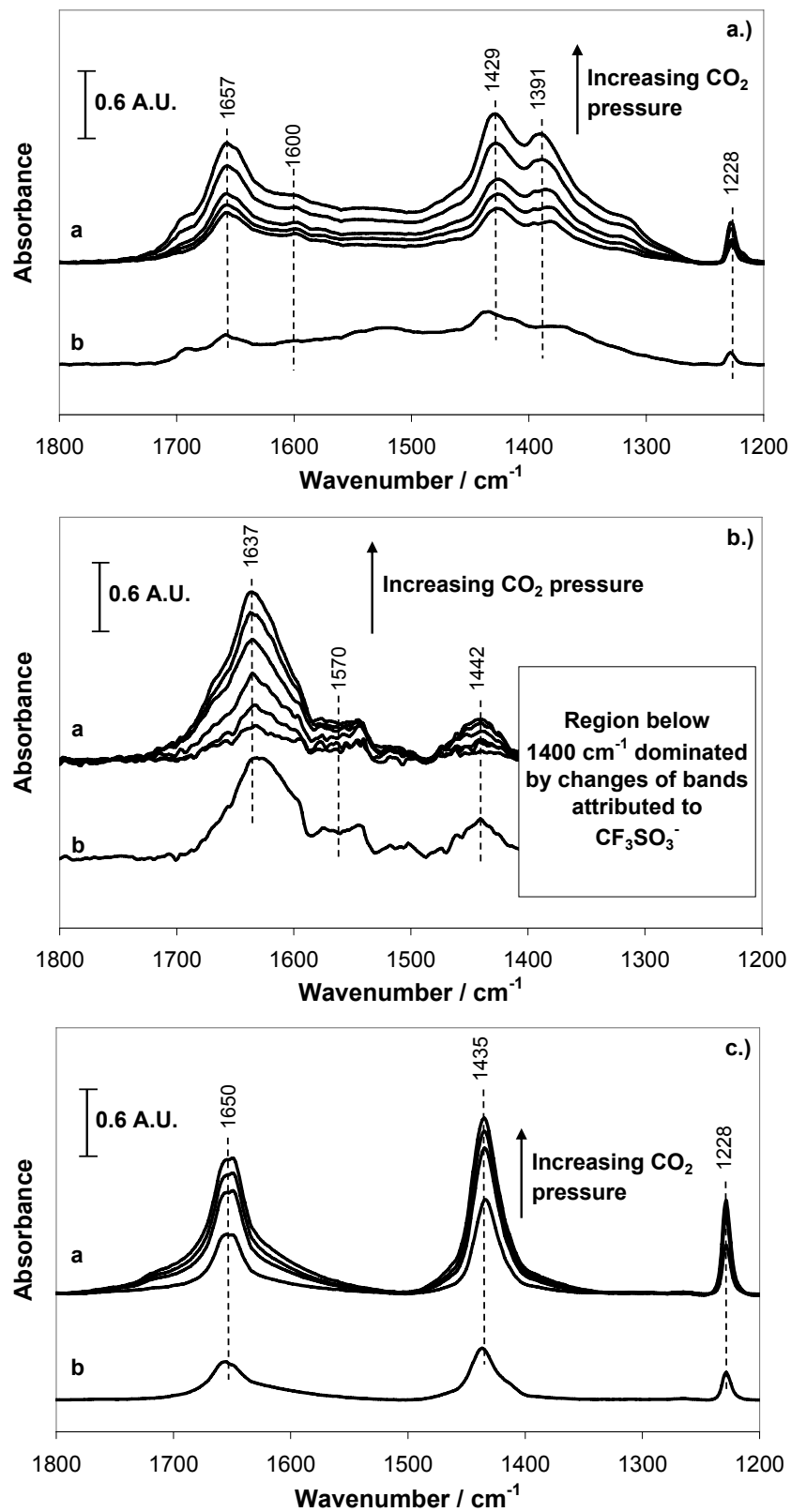
Figure 5-14 IR absorption spectra of CO_2 adsorbed on copper supported on alumina (a), CO_2 adsorbed on Cu/BDiMIm/Al_2O_3 (b) and CO_2 adsorbed on Al_2O_3 (c) (spectrum b after evacuation)

Figure 5-15 compiles the IR spectra after adsorption of D_2O. A broad band around 2570 cm^{-1} (symmetric and asymmetric stretching vibrations) with a feature at 2715 cm^{-1} (due to the formation of surface OD groups) for Cu/Al_2O_3 and around 2615 cm^{-1} for $Cu/BDiMIm/Al_2O_3$ was observed. (Note that due to D-bonding, the bands for the symmetric and antisymmetric stretching vibrations were broadened resulting in only one band around 2570 cm^{-1}.[27]) After evacuation, surface OD groups appeared at 2635, 2710 and 2745 cm^{-1} for the uncoated catalyst and OD-hydrogen bonds were observed at 2625 cm^{-1} for the coated material. It should be noted, that the maximum concentration of adsorbed D_2O was two times higher for $Cu/BDiMIm/Al_2O_3$. The adsorption of D_2O on Al_2O_3 showed identical result to the adsorption on Cu/Al_2O_3 indicating that the observed features are characteristic of adsorption on the support.
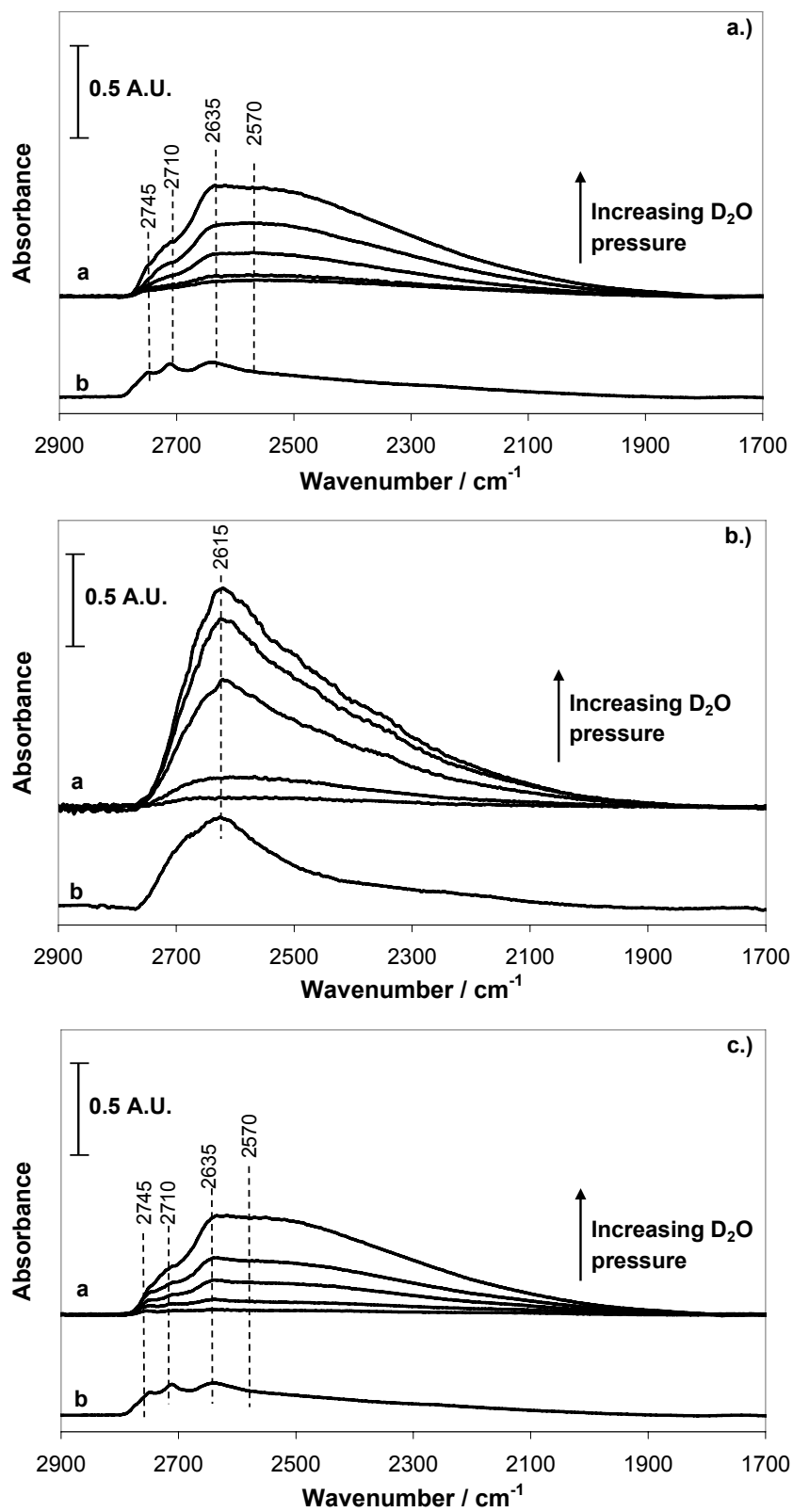
Figure 5-15 IR absorption spectra of D_2O adsorbed on copper supported on alumina (a), D_2O adsorbed on Cu/BDiMIm/Al_2O_3 (b) and D_2O adsorbed on Al_2O_3(c) (spectrum b after evacuation).

5.3.5. In situ infrared spectroscopy during reaction

Figure 5-16 shows the surface species during the course of an experiment with an uncoated catalyst. After admitting CO at 150 °C the band at 2088 cm^{-1} indicated CO adsorbed on Cu^0. The concentration of adsorbed CO was reduced as soon as 10 vol. % water vapor were added to the reactant gas stream. The two bands appearing around 2330 and 2360 cm^{-1} correspond to CO_2 in the gas phase. The band at 1645 cm^{-1} is assigned to OH-bending vibrations of water. The band at 1574 cm^{-1} (appearing at temperatures higher than 170 °C) indicates a carboxyl species and the bands at 1460 cm^{-1} and 1420 cm^{-1} indicate the formation of monodentate and ionic carbonate species, respectively. With increasing temperature the concentration of adsorbed CO and water was reduced, whereas the concentration of carbonates and gas phase CO_2 increased. Purging the catalysts with He at 150 °C after the reaction led to almost complete removal of adsorbed CO with a significant concentration of carbonates remaining on the surface.

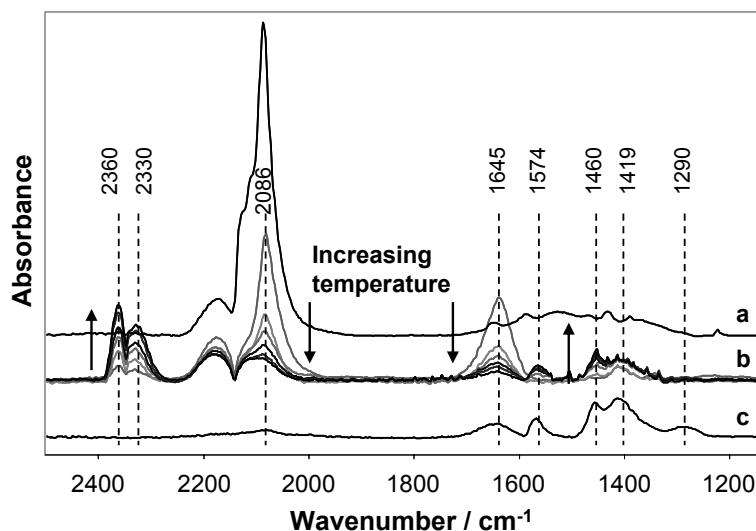**Figure 5-16** Difference spectra of *in situ* IR experiment with uncoated Cu catalyst: 2.5 mL·min^{-1} CO (a), temperature ramp with CO and water (b) and spectrum after exposure at reaction conditions (c).

Figure 5-17 shows the difference IR spectra at reaction conditions for Cu/Al$_2$O$_3$-149, Cu/Al$_2$O$_3$-257 and Cu/Al$_2$O$_3$-54. (Note that the bands attributed to CO in the gas-phase

were subtracted from the spectra.) The position and intensity of the band assigned to CO on Cu^0 varies for the three catalysts. The smallest concentration of adsorbed CO was found for Cu/Al_2O_3-54 showing a band at 2110 cm^{-1}. With Cu/Al_2O_3-257, the band for monodentate CO was found at lower energy (2086 cm^{-1}) and an additional band at 2000 cm^{-1} was observed, which is attributed to CO adsorbed in a bridged mode. The intensity of the CO bands increased from Al_2O_3-54, over Cu/Al_2O_3-149 to Al_2O_3-257 with a ratio of 1:1.8:2.0. The intensity of the band attributed to the OH-bending remained constant for all three catalysts.
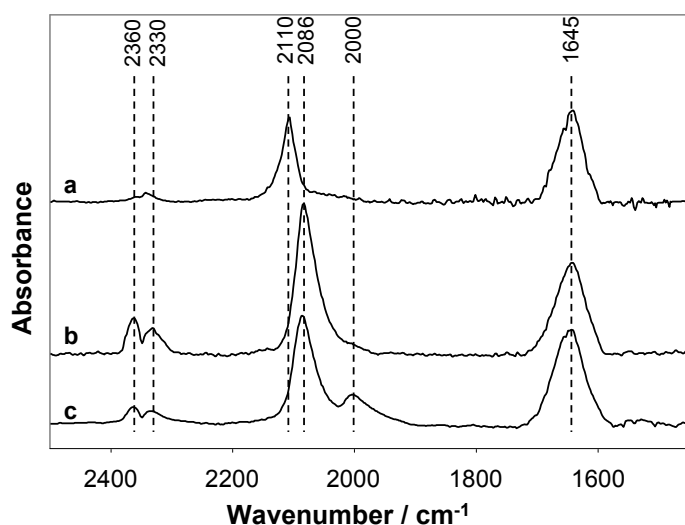
Figure 5-17   Difference IR spectra at *in situ* conditions for Cu/Al_2O_3-54 (a), Cu/Al_2O_3-149 (b) and Cu/Al_2O_3-257 (c).

The comparison between the uncoated (Cu/Al_2O_3-149) and a coated sample ($Cu/BDiMIm/Al_2O_3$-149), shown in Figure 5-18 indicates that only a small concentration of CO is adsorbed on the surface of the ionic liquid coated catalyst (when purging with He a band at 2110 cm^{-1} indicates that CO is adsorbed on Cu). It should, however, be emphasized that also the intensity of the band for OH-bending vibrations of molecular water is smaller for the coated catalyst. The bands at 1485 and 1570 cm^{-1}, observed only on the coated catalyst, indicate the formation of carbonate and carboxyl species on $Cu/BDiMIm/Al_2O_3$-149.
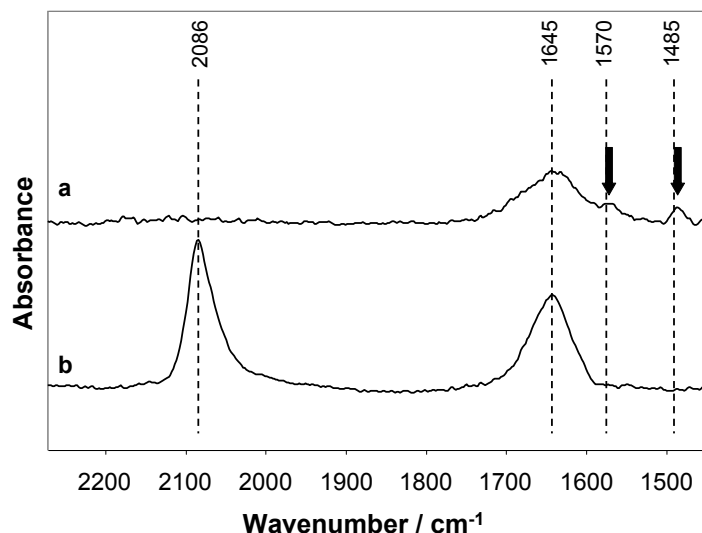
Figure 5-18   Comparison of the difference spectra of an uncoated (a) and an coated(b) copper catalyst.

To investigate the influence of the reactants on the ionic liquid the absorption region of the trifluoromethanesulfonate anion of two samples with a ionic liquid coating of 5 and 20 wt.% are compared in Figure 5-19 and Figure 5-20, respectively. In both cases the IR spectra before reduction, after reduction, in a flow of CO, at reaction conditions (10 % water) and after reaction are displayed.

For the catalyst with a loading of 5 wt. % ionic liquid, bands were observed at 1171 cm^{-1} (antisymmetric CF$_3$), 1225 cm^{-1} (symmetric CF$_3$), 1242 cm^{-1} (antisymmetric SO$_3$ stretching of trifluoromethanesulfonate ion pairs) and 1275 cm^{-1} (antisymmetric SO$_3$ deformation vibrations). After reduction of the catalyst, the bands attributed to the antisymmetric SO$_3$ stretching of trifluoromethanesulfonate ion pairs and to the antisymmetric SO$_3$ deformation vibrations decreased in intensity and a new band was observed at 1330 cm^{-1}. At the same time the bands attributed to CF$_3$ vibrations were shifted to lower wavenumbers. Upon flowing CO over the catalyst, only small changes were observed in the spectrum, but after adding water the spectrum changed appeared to be very similar to the spectrum before reduction. This indicates that the presence of water seems also to induce changes in the interaction of the ionic liquid with the metal surface.

Figure 5-19 Trifluoromethanesulfonate region of IR difference spectra during *in situ* experiments for a Cu catalyst coated with 5 wt.% BDiMIm (before reduction at (a), after reduction (b), under CO (c), under reaction conditions (d) and after reaction (e)).

The spectra of the catalyst with an ionic liquid loading of 20 wt. % showed four bands before admission of H_2. Antisymmetric and symmetric CF_3 vibrations were observed at 1154 cm^{-1} and at 1222 cm^{-1}, the antisymmetric SO_3 stretching of trifluoromethanesulfonate ion pairs and the antisymmetric SO_3 deformation vibrations at 1240 and 1275 cm^{-1}. A band at 1330 cm^{-1} appeared again after reduction and disappeared after exposing the catalyst to CO/H_2O. In contrast to the catalyst with the lower loading, the other parts of the spectra were hardly influenced by changing the gas atmosphere.

The spectra of the catalyst with a higher loading of ionic liquid implies that only the direct interaction with the surface can be observed. The changes of the oxidation state of copper and the interaction of the surface species with the ionic liquid can only be observed by the appearance and disappearance of the band at 1330 cm^{-1}. The changes of the other bands are overlaid by the vibrations of molecules in the bulk phase.
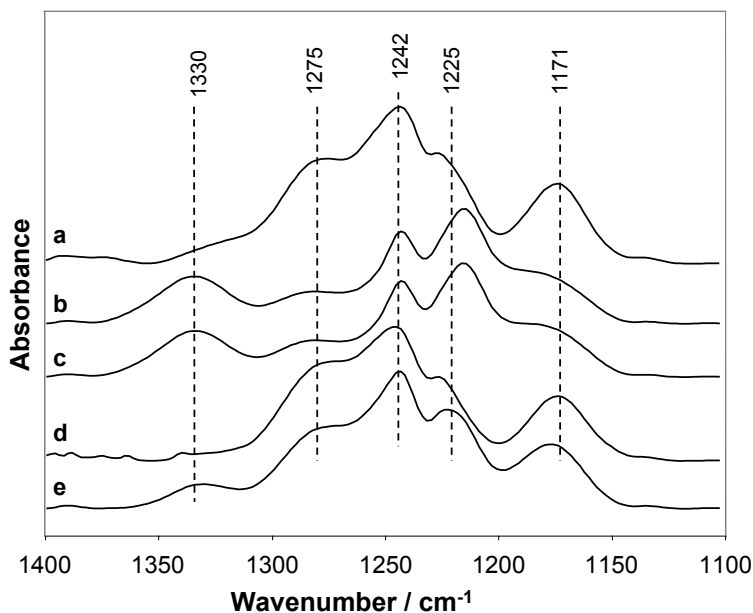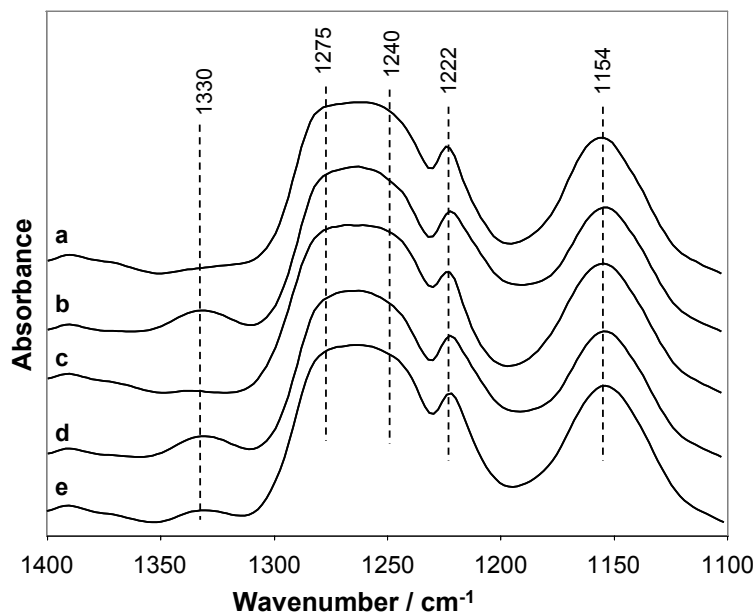
Figure 5-20 Trifluoromethanesulfonate region of IR difference spectra during *in situ* experiments for a Cu catalyst coated with 20 wt.% BDiMIm (before reduction at (a), after reduction (b), under CO (c), under reaction conditions (d) and after reaction (e)).

5.3.6. CO Adsorption isotherms

The adsorption isotherms of CO at 70 °C for $BDiMIm/Al_2O_3$ and Cu/Al_2O_3 are shown in Figure 5-21.
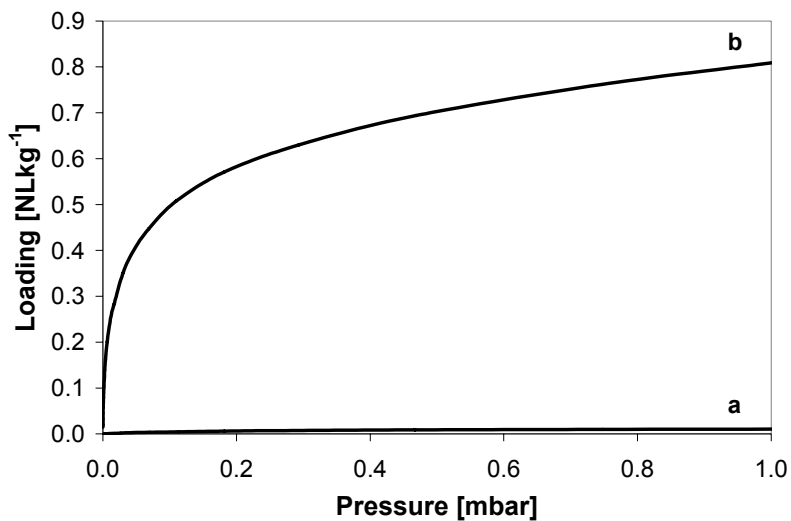
Figure 5-21: CO adsorption isotherms (70 °C) for $BDiMIm/Al_2O_3$ (a) and Cu/Al_2O_3 (b).

5.4. Discussion

5.4.1.   *State of the catalysts*

XANES indicated that the fraction of oxidized Cu in the uncoated catalysts increased in parallel to the specific surface area of the support. Cu/Al_2O_3-54 and Cu/Al_2O_3-99, for example, were nearly fully reduced, while a significant fraction of oxidized Cu was observed with the other catalysts. In line with the increase in the white line, EXAFS showed that the number of oxygen neighbors increased in parallel to the surface area of the support also indicating a higher fraction of oxidized Cu. As the copper particles size decreased with increasing specific surface area of the support, the results show that the fraction of oxidized Cu increases, as the particle size decreases.

Because the Cu-Cu distances in the particles were identical with those of metallic Cu, the oxygen atoms are concluded to be located at the surface of the copper particles. Figure 5-22 shows the maximum number of oxygen neighbors possible at the surface assuming that the oxygen atoms are located in the tetrahedral and octahedral vacancies of the copper surface. A visualization of the location of O on the surface of Cu (111) and (100) terminated particles are shown in Figure 5-23. A cluster containing 147 Cu atoms has 6 (100) and 8 (111) surfaces with 16 and 10 Cu atoms respectively. For each (100) surface 9 oxygen atoms can be coordinated to the vacancies, whereas for the (111) surfaces maximally 6 oxygen atoms can be coordinated leading to maximum 102 oxygen atoms that can be coordinated to a Cu cluster with 147 atoms. The maximum number of oxygen neighbors is then 2.45 whereas the Cu coordination number is 8.97. For a given copper particle size, the number of oxygen neighbors found experimentally were 20 to 30 % of that maximum coordination number determined from the model structure. Thus, we conclude that at most about one third of the copper surface atoms were blocked by oxygen. It should be noted at this point that the oxygen on the copper surface plays an important role for the structure the nanoparticles adopt, if exposed to water-gas shift conditions (*vide infra*).

Because the fraction of the potential interface between the metal particle and the oxide support is much smaller than the fraction of the oxidized Cu, we conclude the oxygen

atoms on the surface are located to a large extent on the accessible part of the copper nanoparticles.
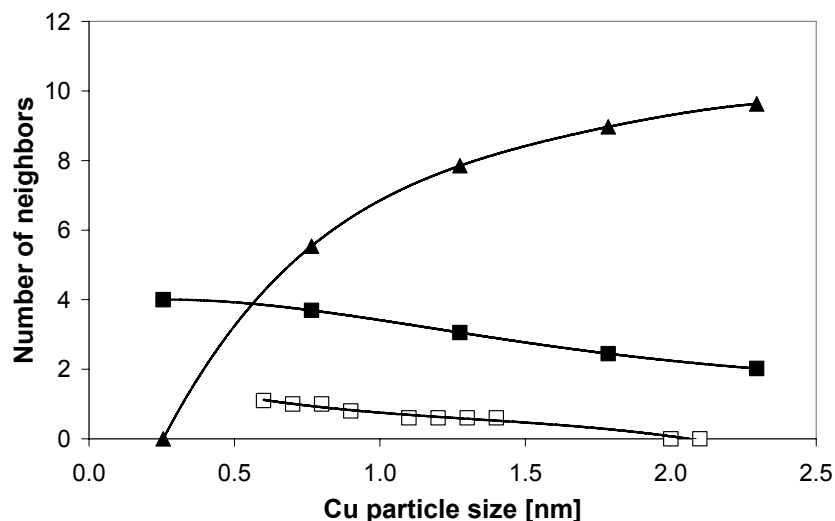
Figure 5-22   Calculated maximum number of copper (▲) and oxygen neighbors (■) assuming cuboctahedral geometry and the observed numbers of neighbors for oxygen (□) in dependence of copper particle size (oxygen is only located on the surface of the catalyst).

Cu cluster, 147 atoms
92 surface atoms

6 x 100 surface
with 16 Cu atoms

8 x 111 surface
with 10 Cu atoms

CuO cluster
102 oxygen atoms

9 oxygen per surface
→ 54 oxygen atoms

6 oxygen per surface
→ 48 oxygen atoms

Figure 5-23   Model of ideal cuboctahedral Cu cluster with oxygen atoms in tetrahedral and octahedral vacancies.

The presence of large copper particles observed for supports with a lower specific surface area (see Figure 5-24) is attributed to the fact that during the preparation

procedure the local concentration of the copper ions is higher in the case of a low surface area support (8.8 Cu^{2+} per nm^2) compared to a high surface area support (1.3 Cu^{2+} per nm^2). This facilitates agglomeration of the precursor or the metal atoms in formation process.
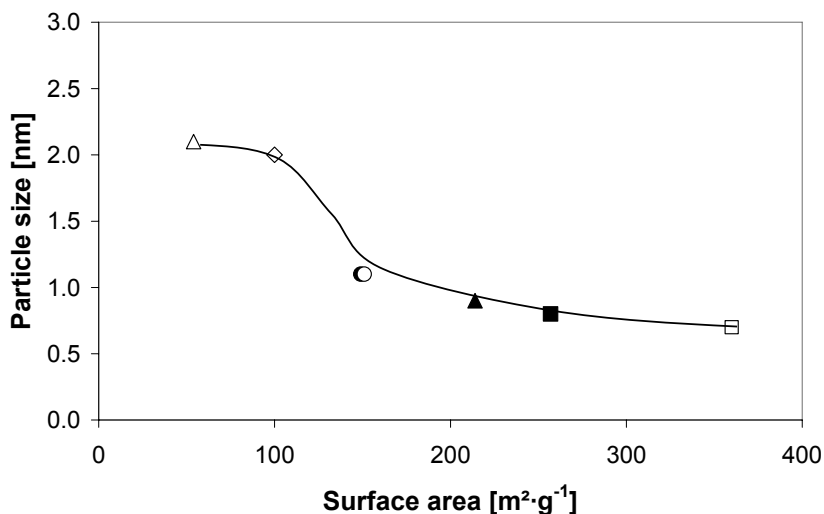
Figure 5-24   Particle size in dependence of support surface area ($\square$ Cu/Al_2O_3-360, $\blacksquare$ Cu/Al_2O_3-257, $\blacktriangle$ Cu/Al_2O_3-214, $\bullet$ Cu/Al_2O_3-149, $\bigcirc$ Cu/Al_2O_3-151, $\diamond$ Cu/Al_2O_3-99 and $\triangle$ Cu/Al_2O_3-54).

Compared to the uncoated catalysts, the IL coated catalysts show a higher degree of Cu reduction after treatment in hydrogen. As the concentration of the supported ionic liquid increases, the fraction of metallic Cu increased. This is attributed to the high solubility of water, formed during reduction as well as the low solubility of oxygen in the polar ionic liquid. With the coated catalysts also the copper particle size was higher than with uncoated catalysts. This indica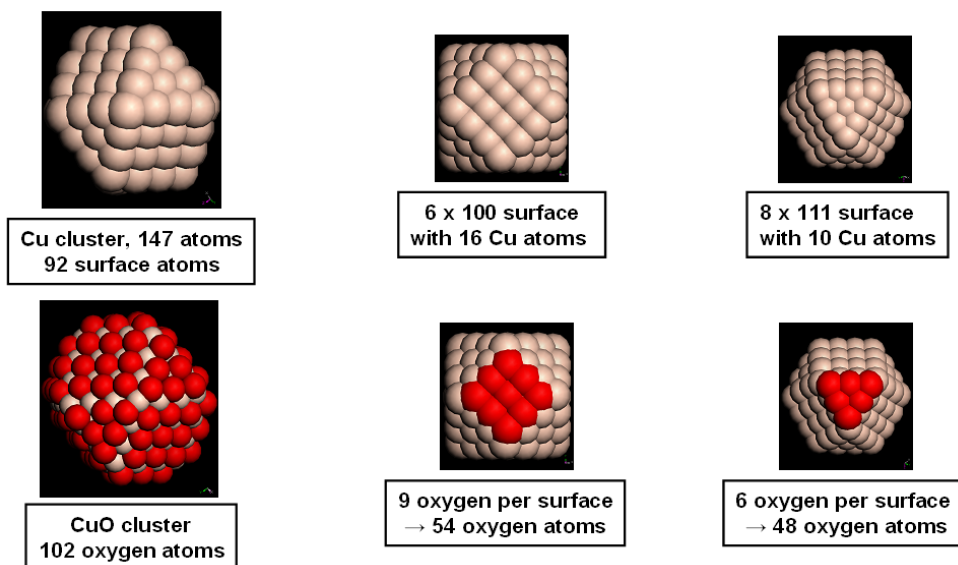tes that the ionic liquid increases either the mobility of the precursor salt or of the Cu particles as they are formed indicating that the restructuring of nanoparticles is facilitated by the ionic liquid.

5.4.2.   Sorption of reactants

For the uncoated catalysts the *in situ* IR spectra reflect the different size of the copper particles. The wavenumber of the band attributed to CO adsorbed on Cu^0 was shifted

from 2082 cm^{-1} (Cu/Al$_2$O$_3$-149) to 2110 cm^{-1} (Cu/Al$_2$O$_3$-54). As the fraction of oxygen on the Cu surface is lower on the larger particles than on the smaller, the increase in wavenumber of adsorbed CO indicates stronger dipole-dipole interactions of CO adsorbed on larger particles. However, we cannot rule out strong bonding on defect sites of the smaller particles. This is supported by the fact that for the Cu/Al$_2$O$_3$-257 catalyst bridged bound CO was found indicating an even stronger bond to the surface compared to the other catalysts. Note that this is in good agreement with the fact that the observed apparent energy of activation for the catalyst with the highest surface area was lower.) Corrected for free accessible surface atoms of Cu, the concentration of adsorbed CO was identical on all samples (see Figure 5-25). The linear correlation passes however, not through the origin indicating that a certain constant fraction of the reduced Cu is blocked by other species or is not accessible for CO, e.g., the interface between the particle and the support.
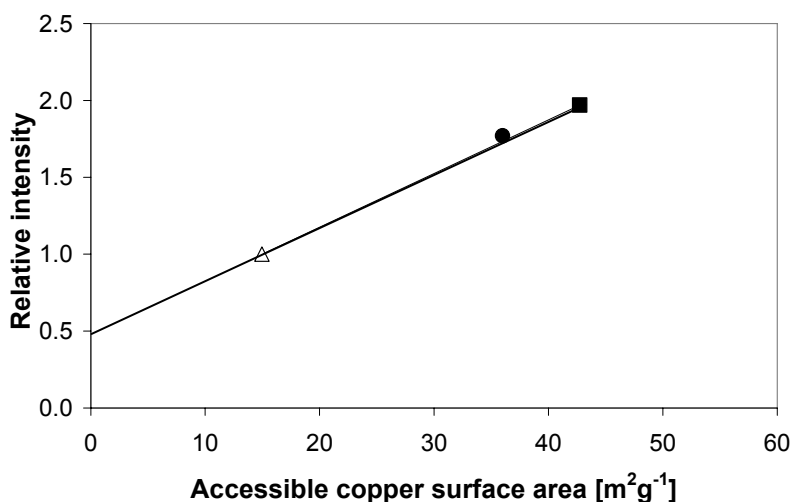
Figure 5-25   Relative intensity of adsorbed CO on Cu/Al$_2$O$_3$-257 (■), Cu/Al$_2$O$_3$-149 (●) and Cu/Al$_2$O$_3$-54 (△) versus Copper surface area determined by EXFAS.

In addition to the bands of bridged bidentate carbonates and ionic carbonates, which were also observed with the parent support, bands attributed to carboxylic species were observed on the uncoated copper catalyst indicating that in the presence of Cu CO$_2$ forms a carbon-metal bond. As this carboxyl species is also observed in the *in situ* experiments,

we conclude that the reaction involves the formation of COOH group on the surface, i.e., that the reaction follows the associative mechanism.[5, 11]

Because the IR spectra after of D_2O on the uncoated copper catalyst and the parent support were identical, we conclude that water is adsorbed in its majority on the support and that the adsorption is not influenced by the presence of copper nanoparticles. This fact obscures that dissociation of water on the Cu particles that is the prerequisite for the catalytic chemistry. As the dissociation of water, which is facilitated by the presence of adsorbed oxygen[28] is generally considered to be the rate determining step, the concentration of OH groups on Cu is assumed to be small.

With coated catalysts the band of adsorbed CO on Cu covered with IL at 2117 cm^{-1} appeared at higher wavenumber than the corresponding band with uncovered Cu particles. The lower coverage in the case of IL covered Cu particles (in line with the low activity of CO dissolved in the ionic liquid in accordance with the literature[29-31]) allows us to exclude CO dipole coupling as cause for this blue-shift. Because the oxygen coverage of the IL covered particles after reduction with H_2 at 215 °C is minimal (judged from the XAFS data) the blue shift is tentatively concluded to be related to markedly weakened CO adsorption in the presence of the ionic liquid. This is attributed to the competitive interaction of the ionic liquid with the Cu surface.

While, the concentration of CO_2 adsorbed was higher for the coated catalyst after evacuation, the principal states of adsorbed CO_2 on the uncoated and coated catalysts were concluded to be identical. The downward shift of the bands of the bridged bidentate carbonate and carboxylic species together with the changes in the bands of the trifluoromethanesulfonate species with the coated catalyst indicates that the ionic liquid interacts with chemisorbed CO_2. The higher concentration of bidentate carbonate indicates that chemisorbed CO_2 is stabilized by the ionic liquid, in good agreement with the strong interaction of CO_2 with the CF$_3$-group (*vide infra*).[32-34].

D_2O adsorption showed that the concentration of adsorbed water was two times higher for the coated catalyst, which indicates that the ionic liquid[35] increases the activity of water during the water-gas shift reaction. It is interesting to note that despite the stronger interactions, the IR stretching band of adsorbed water was broader in the

case of the uncoated catalyst than with the IL covered samples indicating a less diverse environment in the latter case.

The strong interactions between the reactants and the ionic liquid are also reflected in the changes of the IR bands of the IL $CF_3SO_3^-$ groups. Note that mainly the anion of the ionic liquid is interacting with the surface.[15] The change from $Cu^{I/II}$ to Cu^0 after the reduction leads to a decrease of the band at 1275 cm^{-1} attributed to antisymmetric sulfonate vibration and the appearance of a band at 1330 cm^{-1} attributed to this vibration of a species with a stronger S=O bond. This indicates an increase in the bond strength of two sulfonate oxygen atoms with the surface, which in turn increases the strength to the remaining bonds to the oxygen and the carbon atom. Indeed, the bands corresponding to CF_3 vibrations are shifted to lower wavenumbers indicating weaker C-F bonds as electrons from Cu^0 are pushed into the CF_3 antibonding σ^* orbital.[36] Thus, we conclude that the trifluoromethanesulfonate is adsorbed sideways and normal to the surface with two oxygen atoms bound to Cu. After admitting CO and water, however, the spectrum turned back to its state before reduction indicating that the interaction of CO with Cu is stronger (despite its reduced strength in the presence of the IL) than the interaction with $CF_3SO_3^-$.

5.4.3.   *Water-gas shift catalysis*

For the uncoated catalysts the highest activity in the low temperature water-gas shift reaction for the uncoated catalysts was observed for Cu supported on Al_2O_3-149 and Al_2O_3-151 both with a fraction of about 20 % of the Cu atoms being oxidized. Figure 5-26 shows that the catalytic activity decreases with higher and with lower degrees of reduction. The copper particle size for these catalysts determined from EXAFS was 1.1 nm and in average 0.6 oxygen neighbors for the Cu atoms were observed (compared to maximally 3.3 oxygen neighbors if the entire surface of the cluster is occupied with oxygen).

The degree of reduction and also the particle size increased during the treatment of the materials with CO and during the water gas-shift reaction. XANES indicates that the degree of reduction increases after flowing CO over the catalyst for 30 minutes. Under

these conditions the formation of bidentate CO species can be observed by IR spectroscopy indicating a change of the shape of the nanoparticles induced by the reaction of CO with surface oxygen. It is also remarkable that Cu is further reduced by admission of water to the stream of CO. This is attributed to the oxygen aided dissociation of water forming two hydroxyl groups that react quickly with adsorbed CO to carboxylic surface species. The fact, that the size of the copper particles as well as the number of oxygen neighbors was similar for all uncoated samples after reaction, (note that the catalytic activity was different) implies that not only the size of the clusters is of importance for the reactivity. It suggests that the structure of the nanoparticles, for example the concentration of highly uncoordinated sites is important. Note in that respect that copper nanoparticles containing defect sites are claimed to lead to a higher CO conversion activity.[37] Thus, it appears that the structure of the copper particles before the reaction determines the reactivity of the catalysts. In this context we speculate that for the catalysts having a high fraction of metallic Cu (Cu/Al_2O_3-99 and Cu/Al_2O_3-54) less defect sites can be formed by removing oxygen leading to less active catalysts.
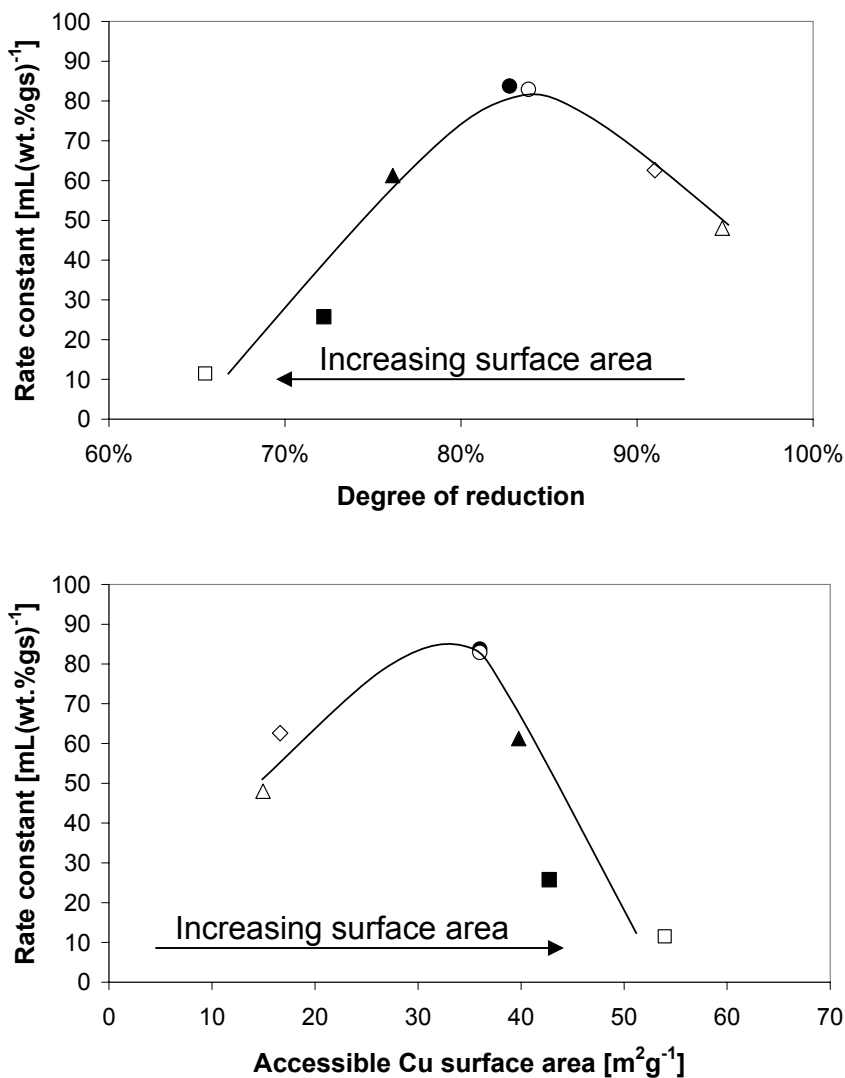
Figure 5-26 Activity of uncoated copper catalysts in dependence of the degree of reduction (upper part) and in dependence of accessible Cu surface area (lower part) ($\square$ Cu/Al_2O_3-360, $\blacksquare$ Cu/Al_2O_3-257, $\blacktriangle$ Cu/Al_2O_3-214, $\bullet$ Cu/Al_2O_3-149, $\bigcirc$ Cu/Al_2O_3-151, $\diamond$ Cu/Al_2O_3-99 and $\triangle$ Cu/Al_2O_3-54).

A kinetic isotope effect (k_H/k_D) of 1.2 was observed for the uncoated catalyst. This confirms that the steps of the reaction mechanism involving an abstraction of hydrogen (abstraction of hydrogen from water and the decomposition of COOH) are involved in the rate determining step.

To compare the activities of coated and uncoated catalysts three catalysts were chosen, i.e., Cu/Al_2O_3-54, Cu/Al_2O_3-149 and Cu/Al_2O_3-257, being examples for the optimum catalyst state as well as for a too high and too low degree of reduction for the uncoated

materials. In case of the coated catalysts, however, XAFS confirmed that the oxidation state and the copper particle size of all catalysts were similar. The catalytic activity increased with increasing specific surface area of the support leading to a lower averaged thickness of the IL film.

At temperatures below 180 °C the coated catalysts were more active than the uncoated materials. Due to the higher activity, the formation of carboxyl species was observed at lower temperatures compared to the uncoated systems, also indicating that these species are stabilized by the ionic liquid.

With increasing temperatures the catalytic activity for the coated catalysts decreased leading to an apparent negative energy of activation. We tentatively attributed this to the decreasing solubility of the reactants in the ionic liquid with increasing temperatures.

The question arises at this point as to why the coated catalysts are more active than the uncoated ones and why the activity drops with increasing reaction temperature. The activity of catalysts in the water-gas shift reaction is determined by the concentration of the reactants at the active sites and by the intrinsic activity of the catalyzing metal. Because the coated catalysts have an environment different from the gas phase at the surface, also the concentrations/activities of the educts in the ionic liquid have to be considered. This is especially important for CO is of interest, as the solubility of CO in ionic liquids is known to be low.[30]

At equilibrium conditions Henry's law can be applied to determine the activity of CO in the ionic liquid:

$$k_{H,CO}(T,\,p) \cdot a_{CO}(T,m_{CO}) = f_{CO}(T,p) \tag{21}$$

with Henry's constant of CO in the ionic liquid $k_{H,CO}(T, p)$, the activity of CO in the ionic liquid $a_{CO}(T,m_{CO})$ and the fugacity of CO in the vapor phase $f_{CO}(T,p)$. $k_{H,CO}$ in the supported ionic liquid is 54 MPa (determined from CO adsorption experiments on coated catalysts with and without copper). This is in excellent agreement with the published value of $k_{H,CO}$ (55 MPa).[30] Note that the presence of copper increases the CO uptake by a factor of 30, due to interaction of CO with copper.

The dependence of the chemical potential of CO on the fugacity of CO is given by:

$$\mu_{COgas} = \mu^{og} + RT \cdot \ln(f_{CO}/p^o) \tag{22}$$

with the fugacity dependent chemical potential μ_{COgas}, the standard chemical potential of CO in the gas phase μ^{og} (-137 kJ/mol[38]), the general gas constant R, the temperature T and the standard pressure p^o.

When dissolved in the ionic liquid the chemical potential of CO changes to:

$$\mu_{COsol} = \mu^{os} + RT \cdot \ln(a_{CO}(T,m_{CO})) \tag{23}$$

with the standard chemical potential of CO in the fluid phase μ^{os}.

At equilibrium conditions ($\Delta G = \Sigma_i v_i \cdot \mu_i = 0$) μ_{COgas} is equal to μ_{COsol}. Thus, by combining equation (21) to (23), μ^{os} can be calculated to be -122 kJ/mol for the supported ionic liquid. By comparison μ_{COsol} with μ^{og} (see Figure 5-27), the activity of CO at equilibrium conditions is $a_{CO}(T,m_{CO}) = 0.002$ for the supported ionic liquid.
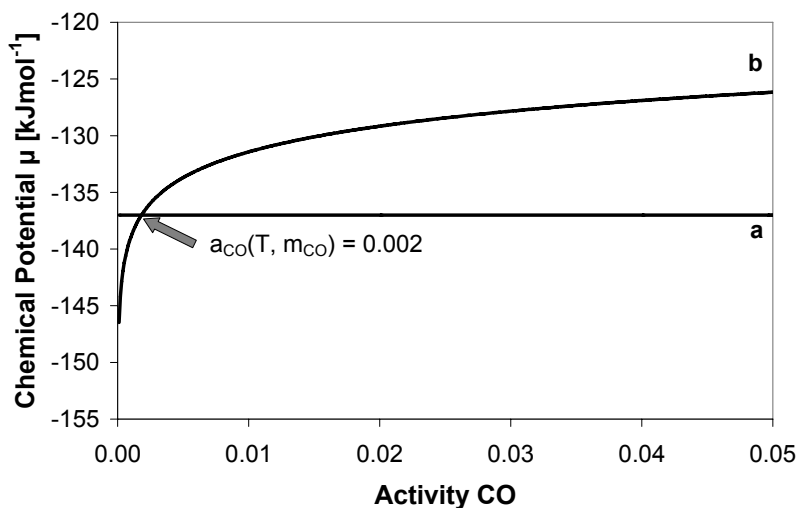

Figure 5-27   Chemical potential of CO in the vapor phase (a) and of CO dissolved in a supported ionic liquid (b).

This shows that as expected the activity of CO in the supported ionic liquid is low, in perfect agreement with the results obtained by IR spectroscopy. The concentration of adsorbed CO is, thus, reduced to approximately 4 % when the catalyst is coated with ionic liquid.

The same considerations can be made for H_2O. Using $k_{H,H2O}(T, p) = 0.05$[39] and $\mu^{og} = -228$ kJ/mol[40], μ^{os} can be calculated to -230 kJ/mol, indicating that 2.75 times more water than copper is present at equilibrium conditions. This is also in good agreement with the IR results, as the amount of observed adsorbed water two times higher for the coated catalyst, due to interactions of the water molecules with the ionic liquid.[35] As pointed out above, the energetic barrier to abstract an H from H_2O is about 7 times higher than the barrier to desorb water from the catalyst surface,[5] therefore, the increased concentration of water adjacent to the active sites will lead to a higher rate since the probability to cleave the O-H bond is higher.

Not only the interaction of H_2O, but also the interaction of the intermediate carboxyl species with the ionic liquid benefits the reaction, because the decomposition of COOH (abstraction of H from *COOH) is the second high energy barrier of the water-gas shift reaction. As the ionic liquid interacts with CO_2,[32-34] it is conceivable that also these carboxyl species interact with the ionic liquid and facilitate so the abstraction of hydrogen. Formate species, formed from CO_2 and H, are assumed to be blocking active sites and can reach considerable surface coverages.[5] Because of the presence of the ionic liquid their adsorption strength is weakened leading to less blocked active sites.

So overall the presence of the IL leads to a higher concentration of the reacting species by weakening of all interactions with the surface and by adjusting at the same time the activities in the liquid phase above the catalyst. A higher concentration of oxygen facilitates the dissociation of water, but as the oxygen concentration increases the concentration of adsorbed CO must decrease creating so a maximum in activity for catalysts with alumina supports of intermediate specific surface area.

5.5. Conclusions

The detailed characterization by *in situ* spectroscopy methods of the interactions of ionic liquids with supported metal nanoparticles leads to detailed insight to the reactivity of the catalysts in the low temperature water-gas shift reaction.

The copper particle size and, thus, the reduction degree vary sympathetically with the specific surface area of the support. The copper particle size and (together with it) the fractions of unreduced Cu and of adsorbed oxygen decide the catalytic activity in the water-gas shift reaction. The presence of adsorbed oxygen on the one hand increases the rate as it reduces the barrier for water dissociation. At the same time the surface coverage with CO increases. If CO is bound too weak (Cu/Al_2O_3-54) or too strong (Cu/Al_2O_3-257) to the active site, the reactivity in the water-gas shift reaction is decreased. In the former case the water adsorption is more difficult on the nearly oxygen free catalysts while on the oxygen rich materials the strong interaction with CO leads to a lower concentration of water. In the presence of the IL CO is adsorbed weaker improving the competitiveness for the adsorption of water.

Catalysts coated with the ionic liquid showed higher water-gas shift activities at low temperatures compared to uncoated and commercial systems. This is attributed due to a higher concentration of water in the proximity of the active sites and due to the interaction of the ionic liquid with reaction carboxyl intermediates facilitating the decomposition of these species. The observed concentrations of the reactants on the ionic liquid coated catalysts are in good agreement with this interpretation.

The present results indicate potential to develop easily manageable and highly active catalysts with a lower metal loading for low temperature water-gas shift superior to the present commercial systems.

5.6. References

[1]   D. L. Trimm, *Appl. Catal., A* **2005**, *296*, 1.

[2]   Y. Amenomiya, G. Pleizier, *J. Catal.* **1982**, *76*, 345.

[3]   T. M. Yureva, *Kinet. Catal.* **1969**, *10*, 862.

[4]   J. A. Rodriguez, P. Liu, J. Hrbek, J. Evans, M. Perez, *Angew. Chem., Int. Ed.* **2007**, *46*, 1329.

[5]   A. A. Gokhale, J. A. Dumesic, M. Mavrikakis, *J. Am. Chem. Soc.* **2008**, *130*, 1402.

[6]   T. Shido, Y. Iwasawa, *J. Catal.* **1993**, *140*, 575.

[7]   C. V. Ovesen, P. Stoltze, J. K. Norskov, C. T. Campbell, *J. Catal.* **1992**, *134*, 445.

[8]   C. V. Ovesen, B. S. Clausen, B. S. Hammershoi, G. Steffensen, T. Askgaard, I. Chorkendorff, J. K. Norskov, P. B. Rasmussen, P. Stoltze, P. Taylor, *J. Catal.* **1996**, *158*, 170.

[9]   P. B. Rasmussen, P. M. Holmblad, T. Askgaard, C. V. Ovesen, P. Stoltze, J. K. Norskov, I. Chorkendorff, *Catal. Lett.* **1994**, *26*, 373.

[10]   G. C. Wang, L. Jiang, Z. S. Cai, Y. M. Pan, X. Z. Zhao, W. Huang, K. C. Xie, Y. W. Li, Y. H. Sun, B. Zhong, *J. Phys. Chem. B* **2003**, *107*, 557.

[11]   Q. L. Tang, Z. X. Chen, X. He, *Surf. Sci.* **2009**, *603*, 2138.

[12]   A. Riisager, R. Fehrmann, S. Flicker, R. van Hal, M. Haumann, P. Wasserscheid, *Angew. Chem., Int. Ed.* **2005**, *44*, 815.

[13]   O. Jimenez, T. E. Muller, C. Sievers, A. Spirkl, J. A. Lercher, *Chem. Commun.* **2006**, 2974.

[14]   C. Sievers, O. Jimenez, R. Knapp, X. Lin, T. E. Muller, A. Turler, B. Wierczinski, J. A. Lercher, *J. Mol. Catal. A: Chem.* **2008**, *279*, 187.

[15]   R. Knapp, A. Jentys, J. A. Lercher, *Green Chemistry* **2009**, *11*, 656.

[16]   C. P. Mehnert, E. J. Mozeleski, R. A. Cook, *Chem. Commun.* **2002**, 3010.

[17]   T. Welton, *Coord. Chem. Rev.* **2004**, *248*, 2459.

[18]   R. Atkin, G. G. Warr, *J. Am. Chem. Soc.* **2005**, *127*, 11940.

[19]   C. Sievers, O. Jimenez, T. E. Muller, S. Steuernagel, J. A. Lercher, *J. Am. Chem. Soc.* **2006**, *128*, 13990.

[20]   A. Wolfson, I. F. J. Vankelecom, P. A. Jacobs, *Tetrahedron Lett.* **2003**, *44*, 1195.

[21]   H. Hagiwara, Y. Sugawara, K. Isobe, T. Hoshi, T. Suzuki, *Org. Lett.* **2004**, *6*, 2325.

[22]   S. M. Webb, *Phys. Scr.* **2005**, *T115*, 1011.

[23]   A. L. Ankudinov, B. Ravel, J. J. Rehr, S. D. Conradson, *Phys. Rev. B* **1998**, *58*, 7565.

[24]   A. L. Ankudinov, J. J. Rehr, *Phys. Rev. B* **2000**, *62*, 2437.

[25]   K. V. Klementiev, XANES dactyloscope, freeware: http://www.desy.de/~klmn/xanda.html.

[26]   R. E. Benfield, *J. Chem. Soc., Faraday Trans.* **1992**, *88*, 1107.

[27]   B. Redlich, PhD thesis, Universität Hannover (Hannover), **1998**.

[28]   G. C. Wang, S. X. Tao, X. H. Bu, *J. Catal.* **2006**, *244*, 10.

[29]   J. Jacquemin, P. Husson, V. Majer, M. F. C. Gomes, *Fluid Phase Equilib.* **2006**, *240*, 87.

[30]   J. Kumelan, A. P. S. Kamps, D. Tuma, G. Maurer, *Fluid Phase Equilib.* **2005**, *228*, 207.

[31]   I. Urukova, J. Vorholz, G. Maurer, *J. Phys. Chem. B* **2005**, *109*, 12154.

[32]   C. Cadena, J. L. Anthony, J. K. Shah, T. I. Morrow, J. F. Brennecke, E. J. Maginn, *J. Am. Chem. Soc.* **2004**, *126*, 5300.

[33]   X. C. Zhang, F. Huo, Z. P. Liu, W. C. Wang, W. Shi, E. J. Maginn, *J. Phys. Chem. B* **2009**, *113*, 7591.

[34]   T. Seki, J. D. Grunwaldt, A. Baiker, *J. Phys. Chem. B* **2009**, *113*, 114.

[35]   L. Cammarata, S. G. Kazarian, P. A. Salter, T. Welton, *Phys. Chem. Chem. Phys.* **2001**, *3*, 5192.

[36]   M. G. Miles, G. Doyle, R. P. Cooney, R. S. Tobias, *Spectrochim. Acta A* **1969**, *A 25*, 1515.

[37]   C. S. Chen, J. H. Lin, T. W. Lai, B. H. Li, *J. Catal.* **2009**, *263*, 155.

[38]   E. Wieberg, *Die chemische Affinität*, 2 ed., de Gruyter, Berlin, New York, **1972**.

[39]   J. K. Shah, E. J. Maginn, *J. Phys. Chem. B* **2005**, *109*, 10395.

[40]   D. R. Stull, H. Prophet, *JANAF Thermochemical Tables*, Natur. Bur. Stand. (U.S.), **1971**.

Chapter 6.

Summary and conclusions

This work was focused on understanding the interactions of immobilized ionic liquids with active components (e.g. metal nanoparticles) as well as with the support. The knowledge of nature of these interactions is of essential value when using these materials as catalysts, since the properties of the ionic liquid are significantly influenced by the support and the active components.

Physicochemical methods are used to study the surface chemistry and the behavior of the highly polar ionic liquid in the presence of nanoparticles. To get further insight, a detailed analysis of reactions was done where materials with supported ionic liquids are used as catalysts (e.g. ethylene hydrogenation and mainly for the low temperature water-gas shift).

Chapter 1 of this thesis gives an overview of the water-gas shift reaction (as this reaction was studied extensively in Chapter 5 of this work) as well as of ionic liquids and supported ionic liquid. Furthermore different preparation methods of supported ionic liquid catalysts with immobilized metal nanoparticles (also used for the preparation of catalysts in this thesis) are presented.

The analysis of the supported platinum catalysts coated with a thin film of BDiMIm in Chapter 2 elucidated the interactions of the ionic liquid with the oxide support and the metal clusters. The spectroscopy confirmed that the vibrations of the imidazolium ring of the SiO_2 supported ionic liquid were less restricted, whereas the viscosity of the ionic liquid increased. This will have a strong impact on the diffusivity of reactants to the active sites, allowing tailoring the selectivity towards certain products. The presence of platinum clusters further modified the electron density of the ionic liquid, which changes the polarity of the ionic liquid within certain limits and can also be used to improve the selectivity. In addition, the complete coverage of the catalyst surface including the metal particles with the ionic liquid protects the catalyst from oxidation, which can be further utilized to protect air sensitive catalysts. The similar catalytic activity of the coated catalyst for ethene hydrogenation at low temperatures shows that the ionic liquid does not block the access of hydrogen or ethane to the active sites. This is important aspect which indicates that the interaction of the ionic liquid and the Pt surface is weaker compared to the reactant molecules and therefore, potential transport limitations resulting from a low solubility of reactants did not occur. This opens new possibilities for the selective

hydrogenation of unsaturated compounds as the properties of the metal and of the reaction environment can be subtly tuned *via* the ionic liquid.

Chapter 3 shows that the local surface chemistry of polymer protected Pt particles is complex, but can be well understood. The PVP shell (up to 5 nm in thickness) around the Pt nanoparticles remains intact under all circumstances. The ionic liquid partly penetrates the protective layer and interacts with the metal. This leads to a significant reduction of the mobility of the ionic liquid molecules as also observed with metal complexes. The protected particles form small islands of aggregated moieties that are connected by interacting polymer strands. Dilution of the sample in methanol leads to partial detachment or dissolution of polymer chains and enhances the island formation. These ensembles segregate at the surface protruding significantly out from the bulk ionic liquid. The ionic liquid covers these ensembles, the organic cation being on top and the SO_3 group of the anion underneath being oriented towards the bulk. This indicates that density differences between the protected Pt particles and the ionic liquid must be a stronger driving force for the corrugation of the surface than classical chemical hydrophobic/hydrophilic interactions. If the latter forces were dominating an even dispersion of the protected particles in the ionic liquid would be the thermodynamically more favored situation.

A good interaction between the polymer and the metal salt prior to the reduction step is essential to assure that all Pt is within the nanoclusters and that Pt is not arbitrarily dispersed in the polymer layer. It is noteworthy to mention that the free mobility of the Pt particles markedly enhances the interaction with the ionic liquid in comparison to Pt particles supported on silica. The Pt nanoparticles dispersed in supported ionic liquids are furthermore accessible for reactants and able to catalyze hydrogenation reactions.

To get further insight to the interactions of supported ionic liquids with different alumina supports and supported copper nanoparticles INS and MAS NMR spectroscopy were used in Chapter 4. INS can be used to determine the influences of the support structure on the ionic liquid whereas solid state NMR spectroscopy gives information about the electrostatic interactions of the support and metal nanoparticles with the ionic liquid. The ionic liquid was aligned with the anion coordinated to the surface of the support. In the INS investigations the acidity of the support and metal nanoparticles had

only a minor influence on the supported ionic liquid. At room temperature, however, supported metal nanoparticles have a dramatic influence on the structure of the ionic liquid, as the viscosity is drastically reduced. At higher temperatures also the acidity of the support is influencing the alignment of BDiMIm (higher acidity leads to a lower mobility of the IL, so the diffusion of reactants through the ionic liquid to the active site will be slowed down).

The detailed characterization by *in situ* spectroscopy methods of the interactions of ionic liquids with supported metal nanoparticles in Chapter 5 gave an insight to the reactivity of the catalysts in the low temperature water-gas shift reaction.

A balanced concentration of oxygen neighboring atoms is necessary to achieve high conversions of CO. These oxygen atoms are removed during the reaction leading to differently structured copper nanoparticles, which in turn lead to different conversions of CO. If CO is bound too weak (Cu/Al_2O_3-54) or to strong (Cu/Al_2O_3-257) to the active site, the reactivity in the water-gas shift reaction is decreased. The particle size and thus the reduction degree can be changed by varying the surface area. The highest activities in the low temperature water-gas shift reaction were observed at a degree of reduction of 83 %. Furthermore the degree of reduction can be increased by using a higher loading of ionic liquid. CO is adsorbed weaker on coated catalysts, whereas the concentration of CO_2 and H_2O was higher in the presence of the ionic liquid. Catalysts coated with ionic liquid showed higher water-gas shift activities at low temperatures compared to uncoated and commercial systems mainly due to a higher concentration of water in the proximity of the active sites and due to the interaction of the ionic liquid with reaction carboxyl intermediates, facilitating the decomposition of these species. The observed concentrations of the reactants on the ionic liquid coated catalysts are in good agreement with thermodynamical considerations. This is a first lead towards the development of catalysts with a lower metal loading for the low temperature water-gas shift reaction.

In summary, the studies presented in this thesis show how different supported ionic liquid catalysts are synthesized and how the different materials act in different catalytic reactions. The first chapters are mainly focused on the interactions of the ionic liquid with the support and the active component, whereas in Chapter 5 mainly *in-situ* spectroscopy methods are used to investigate the way how supported ionic liquid

catalysts work and why they are more efficient than "normal" non-coated catalysts. This work contributes to the field of supported ionic liquids by elucidating the influences on supported ionic liquid by the support and the active component.

Chapter 7.

Zusammenfassung und Schlussfolgerungen

Die vorliegende Arbeit beschäftigt sich mit den Wechselwirkungen von immobilisierten ionischen Flüssigkeiten mit aktiven Komponenten (wie zum Beispiel Metallnanopartikel) sowie den Wechselwirkungen zum Trägermaterial. Die Kenntnis über die Art dieser Wechselwirkungen ist von großer Bedeutung, wenn diese Materialien als Katalysatoren eingesetzt werden, da die Eigenschaften der ionischen Flüssigkeit sich stark unter dem Einfluss des Trägers und der aktiven Komponente verändern.

Physicochemische Methoden wurden angewendet, um die Oberflächenchemie und das Verhalten der hoch polaren ionischen Flüssigkeit in der Anwesenheit von Metallnanopartikeln zu untersuchen. Um tiefere Einsichten zu gewinnen, wurden Reaktionen (wie beispielsweise die Ethenhydrierung oder die Tieftemperatur Wassergas Shift Reaktion) untersucht, bei denen Materialien mit geträgerten ionischen Flüssigkeiten als Katalysatoren eingesetzt wurden.

Kapitel 1 dieser Arbeit gibt sowohl einen Überblick über die Wassergas Shift Reaktion (diese Reaktion wird wieder in Kapitel 5 aufgegriffen), als auch über ionische Flüssigkeiten und geträgerte ionische Flüssigkeiten. Ferner werden verschiedene Methoden zur Herstellung von in ionischen Flüssigkeiten dispergierten Metallnanopatikeln vorgestellt.

Die Untersuchungen an mit BDiMIm beschichteten Pt Katalysatoren in Kapitel 2 klärten die Wechselwirkungen der ionischen Flüssigkeit zum oxidischen Träger und zu den Pt Nanopartikeln auf. Spektroskopische Analysen bestätigten, dass die Schwingungen des Imidazoliumrings der SiO_2 geträgerten ionischen Flüssigkeit weniger beschränkt waren und dass gleichzeitig die Viskosität der ionischen Flüssigkeit zunahm. Dies hat einen starken Einfluss auf die Diffusivität von Reaktanden, was eine Steuerung der Selektivität erlaubt. Die Anwesenheit der Pt Cluster veränderte auch die Elektronendichte der ionischen Flüssigkeit. Diese hat einen Einfluss auf die Polarität der ionischen Flüssigkeit und kann dadurch in gewissem Rahmen zur Steuerung der Selektivität von Reaktionen verwendet werden. Darüber hinaus schützt die vollständige Bedeckung des Trägers und der Pt Cluster mit ionischer Flüssigkeit die Materialien vor Oxidation und führt trägt somit zur einfacheren Handhabbarkeit von luftempfindlichen Katalysatoren bei. Die ähnliche Aktivität der beschichteten und unbeschichteten Katalysatoren in der Ethylenhydrierungsreaktion zeigt, dass die ionische Flüssigkeit nicht

die Zugänglichkeit der aktiven Zentren für Reaktanden behindert. Dies ist ein wichtiger Punkt, da hier gezeigt wird, dass die Wechselwirkungen der ionischen Flüssigkeit mit den Pt Nanopartikeln schwächer ist als die der Reaktanden, sodass potentielle Transportlimitierungen aufgrund einer geringeren Löslichkeit in der ionischen Flüssigkeit ausgeschlossen werden können. Dadurch eröffnen sich neue Möglichkeiten für die katalytische Hydrierung von ungesättigten Verbindungen.

Kapitel 3 zeigt, dass die Oberflächenchemie von polymergeschützten Pt Partikeln komplex ist, aber durch die Anwendung physikochemischer Methoden aufgeklärt werden können. Die PVP Schicht um die Pt Partikel war unter allen Umständen intakt. Die ionische Flüssigkeit drang partiell in die PVP Schicht ein, was zu einer Wechselwirkung mit den Pt Clustern führte. Dies führte wiederum zu einer signifikanten Reduktion der Mobilität der ionischen Flüssigkeit. Die einzelnen PVP geschützten Partikel formten in der ionischen Flüssigkeit kleine Aggregate durch die Wechselwirkung der einzelnen Polymerstränge. Die Verdünnung der Probe führte zu einer Ablösung von Polymerketten, was die Aggregat-Bildung förderte. Die so geformten Aggregate segregierten zum Teil an der Oberfläche der ionischen Flüssigkeit und ragten aus dem Bulk heraus. Die ionische Flüssigkeit bedeckt diese Ensembles, wobei das Kation an der Oberfläche ist und die SO_3 Gruppe des Anions in Richtung des Polymers zeigt. Dies ist ein Hinweis darauf, dass die Dichteunterschiede eine stärkere treibende Kraft für die Korrugation der Oberfläche sind als die klassischen chemischen hydrophoben/hydrophilen Wechselwirkungen. Darüber hinaus wurde gezeigt, dass ein gründliches Durchmischen des Pt Salzes und des Polymers vor dem Reduktionsschritt in der Synthese wichtig ist, damit keine atomar dispersen Pt Partikel in der Polymerschicht gebildet werden. Ferner wurde beobachtet, dass die PVP geschützten Pt Partikel wesentlich stärkere Wechselwirkungen mit der ionischen Flüssigkeit eingehen, als auf Silica geträgerte Pt Partikel. Die so in der ionischen Flüssigkeit immobilisierten Pt Partikel sind zugänglich für Reaktanden und damit in der Lage Hydrierungsreaktionen zu katalysieren.

Um tiefere Einblicke in die Wechselwirkungen von ionischen Flüssigkeiten und geträgerten Kupfer Katalysatoren zu erhalten, wurden in Kapitel 4 INS und MAS NMR Untersuchungen durchgeführt. INS kann dazu verwendet werden, die Einflüsse des Trägers auf die Struktur der ionischen Flüssigkeit zu untersuchen, während durch MAS

NMR Informationen über die elektrostatischen Wechselwirkungen der ionischen Flüssigkeit mit den Cu Nanopartikeln und dem Träger erhalten werden. Es wurde gezeigt, dass die ionische Flüssigkeit mit dem Anion an die Oberfläche koordiniert. Die INS Untersuchungen (bei Temperaturen von ca. 20 K) zeigten, dass die Acidität der Oberfläche sowie die Metallnanopartikel nur einen geringen Einfluss auf die ionische Flüssigkeit haben. Allerdings zeigten die NMR Messungen bei Raumtemperatur einen deutlichen Einfluss der Cu Partikel auf die ionischen Flüssigkeit (drastischer Anstieg der Viskosität). Bei Raumtemperatur zeigte sich auch ein Einfluss der Acidität des Trägers auf die ionische Flüssigkeit.

Die detaillierte Charakterisierung mit *in situ* Spektroskopie Methoden in Kapitel 5 dieser Arbeit gab Einsichten über die Wirkungsweise von beschichteten Katalysatoren in der Tieftemperatur Wassergas Shift Reaktion. Es zeigte sich, dass ein ausgewogenes Verhältnis an Sauerstoffatomen am Cu vorhanden sein muss, um hohe CO Umsätze zu realisieren. Diese Sauerstoffatome werden im Laufe der Reaktion entfernt, was zu unterschiedlich strukturierten Partikeln und somit zu unterschiedlichen Reaktivitäten führt. Es wurde auch gezeigt, dass die Größe der Cu Partikel durch die spezifische Oberfläche des Trägermaterials beeinflusst werden kann. Die höchsten Wassergas Shift Aktivitäten wurden bei einem Reduktionsgrad von 83 % beobachtet. Darüber hinaus kann der Reduktionsgrad des Kupfers durch die Beladung an ionischer Flüssigkeit beeinflusst werden. An den beschichteten Katalysatoren wird CO schwächer adsorbiert, während die CO_2 und H_2O Konzentrationen steigen. Diese beschichteten Katalysatoren zeigten bei tiefen Temperaturen höhere Aktivitäten als die unbeschichteten Katalysatoren. Der Grund hierfür liegt in der höheren Wasserkonzentration in der Nähe der aktiven Zentren, da die Spaltung des Wassers einer der Geschwindigkeits-bestimmenden Schritte der Reaktion ist. Aber auch die Wechselwirkung der ionischen Flüssigkeit mit den Carboxyl-Intermediaten der Reaktion führte zu einer schnelleren Spaltung dieser Spezies. Thermodynamische Betrachtungen bestätigten die während der Reaktion beobachteten Konzentrationsverläufe. Dies ist ein erster Schritt zur Entwicklung von Wassergas Shift Katalysatoren mit einer niedrigen Kupfer Beladung.

Zusammenfassend beschreibt diese Arbeit, wie verschiedene mit ionischer Flüssigkeit beschichtete Katalysatoren synthetisiert werden und wie diese Katalysatoren in

verschiedenen Reaktionen funktionieren. Die ersten Kapitel sind auf die Wechselwirkungen der ionischen Flüssigkeit mit dem Trägermaterial und der aktiven Komponente fokussiert, während in Kapitel 5 *in situ* Spektroskopiemethoden verwendet werden, um aufzuklären, wie diese Katalysatoren unter Reaktionsbedingungen arbeiten und warum diese effizienter als klassische Katalysatoren sind. Die vorliegende Arbeit ist ein Beitrag zum Verständnis von geträgerten ionischen Flüssigkeiten, wobei die Wechselwirkungen zum Träger und zur aktiven Komponente aufgeklärt werden.

Curriculum Vitae

Richard Knapp was born in Temeschburg on September 25th, 1980. He visited the Ernst Mach Gymnasium Haar untill June 2000, when he graduated and received his Abitur (general qualification for university entrance). After military service from July 2000 until April 2001, he took up chemistry studies at the Technische Universität München, majoring in catalysis and reaction engineering. In 2006, Richard Knapp joined the group of Johannes Lercher (Chair for technical chemistry II) for his Diploma thesis entitled "Catalyzed hydrolysis of lignin and lignin probe molecules in supercritical water". After graduation as "Diplom-Chemiker" (master degree) in August 2006, he stayed in the group of Johannes Lercher as a PhD student at the Tecnische Universität München. His work was focused on the catalysis with ionic liquid mediated metal nanoparticles.

List of Publications

Palladium catalysts immobilized in thin films of ionic liquid for the direct addition of aniline to styrene, C. Sievers, O. Jimenez, R. Knapp, X. Lin, T. E. Müller, A. Turler, B. Wierczinski, J. A. Lercher, J. Mol. Catal. A: Chem., **2008**, 279, 187

Impact of supported ionic liquids on supported Pt catalysts, R. Knapp, A. Jentys, J.A. Lercher, Green Chem., **2009**, 11, 656

Corrugated ionic liquid surfaces with embedded polymer stabilized platinum nanoparticles, R. Knapp, S. A. Wyrzgol, M. Reichelt, T. Hammer, H. Morgner, T. E. Müller, J. A. Lercher, accepted for publication in J. Phys. Chem. C

Water-gas shift catalysts with ionic liquid mediated metal nanoparticles, R. Knapp, S. A. Wyrzgol, A. Jentys, J. A. Lercher, submitted to J. Catal

List of Presentations

Immobilization of metal nanoparticles in supported ionic liquids for fine-tuning of catalysts, (Poster) R. Knapp, T.E. Müller, J.A. Lercher, 19. Deutsche Zeolith Tagung, **2007**, Leipzig, Germany

Solvent cages of ionic liquid: structure and effect on catalysis, (Poster) R. Knapp, T.E. Müller, J.A. Lercher, 40. Jahrestreffen Deutscher Katalytiker, **2007**, Weimar, Germany

ZrO_2 supported K_2CO_3 for the conversion of diphenyl ether in supercritical water, (Poster) V.M. Roberts, R. Knapp, J.A. Lercher, 40. Jahrestreffen Deutscher Katalytiker, **2007**, Weimar, Germany

Catalysis with ionic liquid mediated nanoparticles, (Oral presentation), R. Knapp, T.E. Müller, J.A. Lercher, Europacat VIII, **2007**, Turku, Finland

Catalytic conversion of diphenyl ether in supercritical water as a model compound for lignin hydrolysis, (Poster) V. M. Roberts, R. T. Knapp and J. A. Lercher, Europacat VIII, **2007**, Turku, Finland

Multi-functional catalysts for process intensification - Solvent cages of ionic liquid: structure and effect on catalysis, (Poster) R. Knapp, T. E. Müller and J. A. Lercher, European Congress of Chemical Engineering – VI, **2007**, Copenhagen, Denmark

Nanopartikel in ionischen Flüssigkeiten, (Oral presentation), R. Knapp, A. Jentys, T.E. Müller, J.A. Lercher, 41. Jahrestreffen Deutscher Katalytiker, **2008**, Weimar, Germany

Catalysis with ionic liquid mediated nanoparticles, (Oral presentation), R. Knapp, A. Jentys, J.A. Lercher, EUCHEM 2008 Conference on Molten Salts and Ionic Liquids, **2008**, Copenhagen, Denmark and Green Solvents - Progress in Science and Application, **2008**, Friedrichshafen, Germany

Water-gas shift catalysts with ionic liquid mediated nanoparticles, (Poster) R. Knapp, A. Jentys, J.A. Lercher, 42. Jahrestreffen Deutscher Katalytiker, **2009**, Weimar, Germany and European Conference on Combinatorial Catalysis Research and High-Throughput Technologies, **2009**, Gandia, Spain